

THE UNIVERSITY OF HULL

**Development of fluorine-18 radiolabelled peptides for
targeted imaging of the CXCR4 chemokine receptor**

Being a thesis submitted for the degree of

Masters by Research in the University of Hull

By

Jarrad Plater, BSc

November 2021

Abstract

The chemokine receptor CXCR4 has been shown to be over-expressed in multiple cancer types and is often linked to a poor prognosis, making it a significant target of interest for both imaging and therapeutics. Early diagnosis, imaging and identification of this receptor, along with others shown to be over-expressed, can inform treatment selection and lead to improved outcomes for patients.

The development of a fluorine-18 based CXCR4 targeting tracer is intended to facilitate an increase in clinical availability due to the longer half-life than the more commonly used gallium-68 tracers such as Pentixafor. A range of novel tracers were synthesised with different length PEG chain spacers, building on previous work by the Archibald group. Competition binding assays and calcium mobilisation assays showed the length of these spacers did not appear to impact on the binding properties of the tracer, with CPC4-PEG₂-PEG₃-F and CPC4-PEG₄-PEG₄-F having very similar IC₅₀ values (198.95 ± 4.75 nM and 199 ± 48.6 nM respectively, by competition binding assay).

Multiple synthetic routes were developed to increase yields and ease of purification before CPC4-PEG₄-PEG₄-¹⁸F was progressed to *in vivo* testing, with final formulated yields of 37 % ± 15 % (decay corrected) delivering 103 ± 53 MBq (n = 5).

Imaging and *in vivo* studies show significant tumour uptake, with a tumour: muscle ratio of 2.9 at 50 minutes after tracer's administration. Analysis by HPLC also showed a reasonable average tracer stability in the tumour, urine and liver (59, 69 and 78% respectively), with metabolites almost undetectable in the plasma.

In vivo studies showed that, while the lipophilicity of this novel tracer is lower than the previous derivatives produced by the Archibald group (-1.13 ± 0.01 compared to the previous value of -0.14 ± 0.02), the excretion route is primarily *via* the biliary system and gut, rather than the renal system. It is still a significant improvement on the previous attempt and shows promise for future development of this tracer class for fluorine-18.

Contents

| | |
|---|-------|
| Abstract..... | ii |
| Contents..... | iii |
| Acknowledgment | viii |
| Abbreviations | ix |
| List of Figures | xiv |
| List of Schemes..... | xvii |
| List of Tables | xviii |
| Chapter One: Introduction..... | 1 |
| 1.1 Medical imaging..... | 1 |
| 1.1.1 History of medical imaging | 1 |
| 1.1.2.1 PET imaging..... | 4 |
| 1.1.2.2 Combining PET and CT | 5 |
| 1.1.3 SPECT imaging..... | 5 |
| 1.1.4 Radionuclides used in molecular imaging..... | 7 |
| 1.1.5 Radionuclide production..... | 7 |
| 1.1.6 [¹⁸ F]fluoro-2-deoxy-2-d-glucose..... | 8 |
| 1.1.7 Classes of imaging agent..... | 10 |
| 1.1.7.1 Peptide-based | 10 |
| 1.1.7.2 Antibodies | 12 |
| 1.1.7.3 Small molecules | 13 |
| 1.1.7.4 Nanoparticles..... | 15 |
| 1.2 CXCR4 | 17 |
| 1.2.1 Chemokines and chemokine receptors | 17 |
| 1.2.2 CXCR4..... | 19 |
| 1.3 CXCR4 in Cancer | 20 |

| | |
|---|----|
| 1.4 CXCR4 targeting tracers | 21 |
| 1.4.1 CXCR4 targeting small molecules..... | 21 |
| 1.4.2 Peptides as imaging agents..... | 25 |
| 1.4.2.1 T140 and its derivatives | 25 |
| 1.4.2.2 Cyclopentapeptides | 27 |
| 1.5 Click reactions | 32 |
| 1.5.1 Click chemistry | 32 |
| 1.5.2 Pre-targeted imaging | 32 |
| 1.5.3 Copper-Catalysed Azide-Alkyne Cycloaddition | 33 |
| 1.6 Research aims | 34 |
| Chapter Two: Results/Discussion..... | 35 |
| 2.1 “Click” radiolabelling strategy..... | 36 |
| 2.2 PEG _x linker synthesis | 37 |
| 2.2.1.1 CC-PEG _n -COOH synthesis | 37 |
| 2.2.1.2 Alternative synthesis method | 38 |
| 2.2.2 N ₃ -PEG _m -Tosyl synthesis..... | 39 |
| 2.3 CPC4-PEG _n -CC synthesis..... | 41 |
| 2.3.1 General Peptide Synthesis | 41 |
| 2.3.2 Side chain protection and protection removal | 45 |
| 2.3.3 Order of reaction steps – when to couple the PEG chain..... | 46 |
| 2.3.4 Purity and by-product analysis..... | 47 |
| 2.4 Stable fluorine isotope standards | 50 |
| 2.4.1 Synthesis method..... | 50 |
| 2.4.2 Reagent solution quantities for PEG coupling | 50 |
| 2.5 Biological studies: <i>in vitro</i> | 54 |
| 2.5.1 Cell receptor binding assays..... | 54 |
| 2.5.2 CXCL12 competition binding assay – Jurkat cells..... | 55 |

| | |
|--|----|
| 2.5.3 Calcium mobilisation assay – U87.CD4.CXCR4 cells [190] | 57 |
| 2.6 Peptide radiolabelling with fluorine-18 for PET imaging | 60 |
| 2.6.1 “Click” reaction for radiolabelling | 60 |
| 2.6.2 LogD comparison | 63 |
| 2.7 <i>In vivo</i> imaging studies | 66 |
| 2.7.1 PET-CT scanning experiments | 66 |
| 2.7.2 Metabolite analysis | 72 |
| Chapter Three: Conclusions and Further Work | 75 |
| 3.1 Summary | 76 |
| 3.2 Conclusions | 76 |
| 3.3 Potential further work | 77 |
| Chapter Four: Experimental | 79 |
| 4.1 General methods | 80 |
| 4.1.1 Solvents and reagents | 80 |
| 4.1.2 Mass Spectrometry | 80 |
| 4.1.3 NMR spectroscopy | 80 |
| 4.1.4 High Performance Liquid Chromatography (HPLC)..... | 80 |
| 4.2 Cell Culture and <i>in vitro</i> assays | 80 |
| 4.2.1 Cell Culture..... | 80 |
| 4.2.2 Cell Counting | 81 |
| 4.2.3 CXCR4 affinity measurement | 81 |
| 4.2.3.1 Competition binding assay..... | 81 |
| 4.2.3.2 Calcium signalling..... | 82 |
| 4.3 <i>In vivo</i> experiments | 82 |
| 4.3.1 General..... | 82 |
| 4.3.2 Tumour implants | 82 |
| 4.3.3 PET/CT imaging | 82 |

| | |
|--|----|
| 4.3.4 Metabolism | 83 |
| 4.4 Peptide synthesis - general methods..... | 84 |
| 4.4.1 General reaction treatments | 84 |
| 4.4.2 Coupling reactions | 84 |
| 4.4.3 Fmoc-deprotection | 84 |
| 4.4.4 N-methylation | 85 |
| 4.4.4.1 o-NBS Protection..... | 85 |
| 4.4.4.2 N-methylation | 85 |
| 4.4.4.3 o-NBS Deprotection | 85 |
| 4.4.5 Alloc cleavage..... | 85 |
| 4.4.6 Dde cleavage | 85 |
| Method A - Cleavage from linear peptide in solid phase | 86 |
| Method B - Cleavage from cyclic peptide in liquid phase..... | 86 |
| 4.4.7 Cleavage from trityl chloride resin..... | 86 |
| 4.4.8 Cyclisation | 86 |
| 4.4.9 Removal of side chain protection groups | 86 |
| 4.4.10 Resin Drying | 86 |
| 4.5 PEG linker synthesis | 87 |
| 4.5.1 Propargyl-PEG _n -acid linker | 87 |
| 4.5.1.1 Synthesis of OH-PEG _n -propargyl | 87 |
| 4.5.1.2 Synthesis of COOH-PEG _n -propargyl | 87 |
| 4.5.2 N ₃ -PEG _m -Tosyl linker | 89 |
| 4.5.2.1 Mono-Tosylation | 89 |
| 4.5.2.2 Substitution of N ₃ | 89 |
| 4.5.2.3 Tosylation 2 | 89 |
| 4.6 Radiochemistry | 90 |
| 4.6.1 PEG radiolabelling | 90 |

| | |
|---|-----|
| 4.6.1.1 Preparation of fluorine-18 | 90 |
| 4.6.1.2 Labelling of PEG precursor | 90 |
| 4.6.2 Copper (I)-catalysed azide-alkyne 1,3-dipolar cycloaddition (CuAAC) | 90 |
| 4.6.3 LogD _{7.4} determination | 91 |
| 4.6.4 Radio HPLC | 91 |
| 4.6.5 Radio-TLC | 92 |
| 4.7 Compound Synthesis..... | 93 |
| 4.7.1 Synthesis of COOH-PEG ₁ -CC..... | 93 |
| 4.7.2 Synthesis of COOH-PEG ₂ -CC..... | 94 |
| 4.7.3 Synthesis of COOH-PEG ₃ -CC..... | 95 |
| 4.7.4 Synthesis of COOH-PEG ₄ -CC..... | 96 |
| 4.7.5 Synthesis of N ₃ -PEG ₂ -Tosyl..... | 97 |
| 4.7.6 Synthesis of N ₃ -PEG ₃ -Tosyl..... | 99 |
| 4.7.7 Synthesis of N ₃ -PEG ₄ -Tosyl..... | 101 |
| 4.7.8 Attempted synthesis of CPCR4-PEG ₂ -CC..... | 102 |
| 4.7.9 Synthesis of CPCR4-PEG ₂ -CC, using Alloc protected ornithine | 103 |
| 4.7.10 Attempted synthesis of CPCR4-PEG ₁ -CC and CPCR4-PEG ₄ -CC | 105 |
| 4.7.11 Attempted synthesis of CPCR4-PEG ₂ -CC and CPCR4-PEG ₃ -CC | 107 |
| 4.7.12 Synthesis of linear, protected CPCR4 peptide backbone, using Dde protected ornithine, using Method A of Dde cleavage. | 109 |
| 4.7.13 Synthesis of CPCR4-PEG ₍₂₋₄₎ -CC, using Dde protected ornithine, with Method B of Dde cleavage | 110 |
| 4.7.14 Synthesis of CPCR4-PEG ₄ -PEG ₄ - ¹⁸ F | 111 |
| References | 112 |

Acknowledgment

I would like to thank Prof Steve Archibald for his ongoing guidance and support during my Masters as my supervisor. I would also like to thank Dr Juozas Domarkas for his patience, always being willing to answer even the most basic of questions, as well as helping share his knowledge and practical skills whenever needed.

I would like to thank Prof Schols and his group in KU Leuven, Belgium, for their work in carrying out the required CXCR4 *in vitro* assays of the peptides synthesised in this study.

I also thank John Wright for providing his expertise and skills in PET imaging and processing the imaging data for analysis reported in this work.

A thanks goes to all members of the Archibald group, past, present and visitors during my time, especially those in C222 for making it a fun lab to work in and assisting with their chemistry knowledge when needed. A special mention goes to George, Noemi and Max for putting up with me and always providing laughter, whatever the situation.

Finally, I would like to thank my family for their support during my Masters, especially during my time writing up, providing me with lifts to and from the university in the middle of the night.

Abbreviations

α Alpha

γ Gamma

β Beta

β^- Electron (Beta minus)

ACN Acetonitrile

Arg Arginine

Alloc Allyloxycarbonyl

AMBA Amino methylbenzyl acid

BFC Bifunctional chelator

BGO Bismuth germanate

Br Broad signal

BRCA Breast cancer gene

cFLFLF N-Cinnamoyl-F-(D)L-F-(D)L-F

Cit Citrulline

CT Computerised tomography

CuAAC Copper (I)-catalysed azide-alkyne 1,3-dipolar cycloaddition

d Doublet

DARC Duffy antigen receptor of chemokine

DBU 1,8-Diazabicyclo(5.4.0)undec-7-ene

DCM Dichloromethane

DIPEA N,N-Diisopropylethylamine

DMEM Dulbecco's Modified Eagle Medium

DMF Dimethylformamide

DOTA 1,4,7,10-Tetraazacyclodecane-1,4,7,10-tetraacetic acid

DPPA Diphenylphosphoryl azide

dt Double triplet

EEG Electroencephalogram

EMA European Medicines Agency

FBS Foetal bovine serum

FDA Food and Drug Administration

FDG Fluoro-2-deoxy-2-d-glucose

FDP-6-P Fluoro-2-deoxy-2-d-glucose-6-phosphate

FLT 3-Deoxy-3-¹⁸F-fluorothymidine

Fmoc Fluorenylmethyloxycarbonyl Chloride

G-6-P Glucose-6-phosphate

GLUT Glucose transporters

GPCR G-protein coupled receptor

HATU 1-[Bis(dimethylamino)methylene]-1*H*-1,2,3-triazolo[4,5-*b*]pyridinium
hexafluorophosphate 3-oxid

HBTU *N,N,N',N'*-Tetramethyl-*O*-(1*H*-benzotriazol-1-yl)uronium hexafluorophosphate

HER-2 Human epidermal growth factor receptor-2

HIV Human immunodeficiency virus

HPLC High performance liquid chromatography

IC₅₀ Concentration required to inhibit 50% of binding

kDa Kilodaltons

keV Kiloelectronvolts

Lys Lysine

LSO Lutetium oxyorthosilicate

m Multiple

MRI Magnetic resonance imaging

MS Mass spectrometry

NaI 3-(2-Naphythyl)-alanine

NMP N-Methyl-2-pyrrolidone

NMR Nuclear magnetic resonance

o-NBS 2-Nitrobenzenesulfonyl chloride

OI Optical imaging

Orn Ornithine

Pbf 2,2,4,6,7-Pentamethyldihydrobenzofuran-5-sulfonyl

| | |
|--------------|---|
| PBS | Phosphate buffered saline |
| PEG | Polyethylene glycol |
| PET | Positron emission tomography |
| PIB | Pittsburgh compound B |
| Pro | Proline |
| PTFE | Polytetrafluoroethylene |
| q | Quartet |
| RBC | Red blood cells |
| ROI | Region of interest |
| Rt | Retention time |
| RT | Room temperature |
| s | Singlet |
| SD | Standard deviation |
| SDF-1 | Stromal cell-derived factor-1, also called CXCL12 |
| SPECT | Single-photon emission tomography |
| SSTR | Somatostatin receptor |
| t | Triplet |
| <i>t</i> -Bu | <i>tert</i> -Butyl |
| td | Triple doublet |

| | |
|-----------------|---------------------------|
| TEA | Triethylamine |
| TFA | Trifluoroacetic acid |
| THF | Tetrahydrofuran |
| TK ₁ | Thymidine kinase |
| TLC | Thin layer chromatography |
| TOF | Time of Flight |
| Tyr | Tyrosine |
| US | Ultrasound |

List of Figures

| | |
|--|----|
| Figure 1: Structure of ¹¹ C-Pittsburgh Compound B..... | 13 |
| Figure 2: Structures of Tauvid (left) and [¹⁸ F]FLT (right) | 14 |
| Figure 3: Structure of [⁶⁸ Ga]Ga-NRT-c-FLFLF [69] | 16 |
| Figure 4: Schematic representation of CXCL12/CXCR4 pathway [77] | 17 |
| Figure 5: The Chemokine Wheel: From Balkwill [78]..... | 18 |
| Figure 6: Diagram showing the sub-classes of chemokine receptors, their ligands and association to disease. The receptors for the CXC subclass are shown in blue, receptors for the CC subclass are in red and receptors for the C and CX3C class are in green. (Inspired by figures by Wells <i>et al.</i> and Proudfoot <i>et al.</i>) [80-82]. | 19 |
| Figure 7: Representation of the chemokine receptor CXCR4, showing the seven transmembrane helices, using single letter amino acid codes with key aspartate residues highlighted. Reproduced from De Clercq, E. Nat. Rev. Drug Discov. 2003, 2 (7), 581–587. [86]..... | 20 |
| Figure 8: Structures of AMD3100 (left) and AMD3465 (right)..... | 22 |
| Figure 9: The six configurations of metal-cyclam complexes [123]..... | 23 |
| Figure 10: Structures of the configurationally restricted CB-Bicyclam and its corresponding copper complexes | 24 |
| Figure 11: Structures of RAD1-24 (left) and RAD1-52 (right)..... | 25 |
| Figure 12: Structure of T ₁₄₀ | 25 |
| Figure 13: Molecular structure of CXCR4 binding peptide FC131 | 28 |
| Figure 14: Molecular structure of CXCR4 targeted imaging agent [⁶⁸ Ga]Pentixafor | 29 |
| Figure 15: Example of [⁶⁸ Ga]Pentixafor scan in multiple-myeloma patient. Shown are maximum-intensity projections and transaxial slices at 40 (left) and 236 (right) minutes after injection..... | 30 |
| Figure 16: Molecular structure of [¹⁷⁷ Lu]Pentixather | 31 |
| Figure 17: Structure of the target CXCR4 binding peptide in this work, CPCR4-PEG ₁₋₄ -CC..... | 41 |
| Figure 18: Amino acid activation by HBTU..... | 42 |
| Figure 19: HPLC chromatogram of linear, protected version of CPCR4, pre-PEG chain coupling. | 47 |

| | |
|---|----|
| Figure 20: Pre-PEG chain coupling, linear peptide structures identified by HPLC and MS, with and without Fmoc terminal protection | 47 |
| Figure 21: Potential outcomes following the coupling of CC-PEG ₁ -COOH and cyclisation of peptide without Fmoc protection, with correct cyclic product on the left, incorrect tetrapeptide on the right and incorrect bi-PEG linear peptide above..... | 49 |
| Figure 22: HPLC chromatograms of stable fluorine isotope analogues of the tracer. HPLC gradient: MeOH 0.1% TFA in water 0.1% TFA, 5 to 95%, 20 min, 1.0 mL/min. A: COOH-PEG ₂ -PEG ₃ -F, B: COOH-PEG ₂ -PEG ₄ -F, C: COOH-PEG ₃ -PEG ₃ -F, D: COOH-PEG ₃ -PEG ₄ -F, E: COOH-PEG ₄ -PEG ₃ -F, F: COOH-PEG ₄ -PEG ₄ -F..... | 53 |
| Figure 23: Competition binding assays, carried out by Prof. Schols and his research team at KU Leuven, Belgium. Graphs from repeat assay measurement (each performed in triplicate) to allow determination of a standard deviation..... | 56 |
| Figure 24: Calcium mobilisation assays, percentage inhibition, carried out by Prof. Schols and his research team in Belgium. | 57 |
| Figure 25: Example radio HPLC chromatograms of a purified [¹⁸ F]N ₃ -PEG ₄ -F prosthetic, crude tracer post-“click” reaction and the purified radiotracer..... | 62 |
| Figure 26: Structures of core peptide and respective chelators / ¹⁸ F-labelled moieties..... | 63 |
| Figure 27: Dynamic PET of [⁶⁸ Ga]Pentixafor compared to the previous generation of ¹⁸ F-labelled CXCR4 targeted peptides from the Archibald laboratory. Coronal maximum intensity projections, 40-66 min post administration, U87-CXCR4 xenograft (human CXCR4) mouse model (arrow colour code: red – tumour, white – liver, green – gut, yellow – bladder). | 65 |
| Figure 28: Graphs showing the SUV _{Max} in blocked and unblocked scans, to demonstrate how the tracer can be blocked | 67 |
| Figure 29: Dynamic PET. Coronal maximum intensity projections, 40-50 min post administration, U87-CXCR4 xenograft (human CXCR4) mouse model. Arrow colour code: red – tumour, white – gut, green – liver, blue – gallbladder, purple – bladder, orange – muscle. | 67 |
| Figure 30: Dynamic PET. Coronal maximum intensity projections, 40-50 min post administration, U87-CXCR4 xenograft (human CXCR4) mouse model. Arrow colour code: red – tumour, white – gut, green – liver, yellow – kidney, blue – gallbladder. Left: Unblocked scan. Right: Scan after blocking dose of SJA05 (5 mg/kg) | 68 |
| Figure 31: Graph of SUV _{Mean} ± SD of each organ during dynamic PET scan..... | 69 |

Figure 32: Graph of $SUV_{Mean} \pm SD$ of some organs during dynamic PET scan, to separate out the lines more clearly 69

Figure 33: Graph of $SUV_{Mean} \pm SD$ for Tumour and Muscle during dynamic PET scan..... 70

Figure 34: Graph of Tumour to Muscle ratio during dynamic PET scan 70

Figure 35: Graph showing the $SUV_{Mean} \pm SD$ of organs at 50 mins post injection, the highest tumour to muscle ratio 71

Figure 36: Graph showing the $SUV_{Mean} \pm SD$ of each organ at 50 mins post injection, the highest tumour to muscle ratio, to separate the bars more clearly 71

Figure 37: Radio-HPLC chromatograms of the $[^{18}F]CPCR4-PEG_4-PEG_4-F$ tracer, urine metabolites, plasma metabolites, tumour metabolites and liver metabolites 74

List of Schemes

| | |
|---|----|
| Scheme 1: The Copper-Catalysed Azide-Alkyne Cycloaddition “click” reaction..... | 33 |
| Scheme 2: Synthesis of CC-PEG _n -COOH linkers, n = 1-4 | 37 |
| Scheme 3: Synthesis of CC-PEG _n -COOH linker, avoiding acetic acid impurities, n = 1-4 | 38 |
| Scheme 4: Synthesis of N ₃ -PEG _m -Tosyl linker, m = 2-4 [183, 184]..... | 39 |
| Scheme 5: Synthetic route for CPCR4-PEG _n -CC, using alloc protected ornithine..... | 43 |
| Scheme 6: Synthetic route for CPCR4-PEG _n -CC, using Dde protected ornithine (up to the formation of the linear peptide there is no difference between the methods, other than the protection groups shown)..... | 44 |
| Scheme 7: Fmoc protection group removal by piperidine treatment..... | 45 |
| Scheme 8: Terminal amine N-methylation | 45 |
| Scheme 9: Radiotracer synthesis <i>via</i> “click” reaction..... | 60 |
| Scheme 10: Aqueous radio fluorination of NOTA-pentixather. Reproduced from Poschenrieder <i>et al.</i> [162]..... | 64 |

List of Tables

| | |
|---|----|
| Table 1: Comparison of <i>in vivo</i> imaging techniques [7, 8] | 3 |
| Table 2: Half-life, decay modes and production methods of radioisotopes commonly used for clinical medical imaging | 7 |
| Table 3: Generator pairs and half-lives..... | 8 |
| Table 4: Corrected quantities for PEG chain coupling reactions | 51 |
| Table 5: HPLC retention times and purities of stable fluorine isotope analogues of the tracer. HPLC gradient: MeOH 0.1% TFA in water 0.1% TFA, 5 to 95%, 20 min, 1.0 mL/min..... | 52 |
| Table 6: Compounds and CXCR4 affinity, from competition binding assay measurements, (n = 2) ^a Compounds containing PEG ₃ were from the same batch of linker and results may be inaccurate due to undetected impurities or samples diminished before testing. ^b n = 1 | 56 |
| Table 7: Compounds and CXCR4 affinity, from calcium mobilisation assay measurements. ^a As with the previous binding assay, PEG ₃ was from the same batch and results indicate there may have been an undetected impurity or samples diminished before testing. | 58 |
| Table 8: Lipophilicity comparison, from LogD _{7.4} or LogP, as required | 63 |
| Table 9: Tracer stability summary for selected organs (extraction and analysis by radio-HPLC, 2 hours post injection). | 73 |

Chapter One: Introduction

1.1 Medical imaging

1.1.1 History of medical imaging

Medical imaging began with the use of X-rays in 1895, discovered by physicist Wilhelm Roentgen [1]. For several decades, X-rays were the only method available to image internal anatomy, until the development of ultrasound (US) in the 1960s, followed by computerised tomography (CT), magnetic resonance imaging (MRI) and optical imaging (OI) shortly after [1]. Mathematical models for reconstruction from projections had been published from 1917, but were only developed for medical use in the 1970s, for use in CT and, subsequently, nuclear medicine imaging [2]. MRI, ultrasound and optical imaging have the advantages of not delivering any ionising radiation to the patient, but can have significant disadvantages for some types of imaging. A comparison summary of properties is included in Table 1.

The field of nuclear medicine was first recognised in 1946 with the treatment of thyroid cancer, using iodine-131, though it had been investigated in various forms since the 1920s [2, 3]. Although nuclear imaging techniques were developed in the 1970s, the full application of tomographic methods was only available in the 1980s, due to the computing power needed. Although single-photon emission tomography (SPECT) and positron emission tomography (PET) have been used in research since the 1980s, they have only been used clinically more recently, and first combined with CT since 2001, leading to more accurate images, with fewer artefacts [4].

The use of PET imaging has increased rapidly in recent years, with a 12.6% increase in PET-CT scans carried out in England in 2019/20 on the previous year, to give a total of nearly 200,000. SPECT scans had a 0.6% reduction in the same time frame but a 13.4% increase the year before, with over 45,000 being carried out, both following similar increases for the previous ten years [5]. This is partly due to advances in imaging technologies, leading to lower costs and higher sensitivity and an improvement in infrastructure. The reason for the lack of increase in SPECT scans is unclear but may be linked to the replacement of some SPECT imaging with PET-CT imaging.

With any medical investigation, the more data provided, with the highest sensitivity, the better. This is an area that PET has an advantage, being able to track biochemical, physiological and pharmacological processes with very high sensitivity (10^{-11} - 10^{-12} mol.L⁻¹) [6].

The combination of PET and CT in the same scanner allows for patients to be scanned with both during the same non-invasive procedure, providing metabolic or biochemical information *via* PET and anatomical information *via* CT. When imaging cancerous tumours, this combination provides crucial

information on the progression on the disease, either during treatment with chemotherapy or radiotherapy, or during the planning of surgical intervention.

The development of more tracers also means a wider range of conditions can be investigated, including cancer, cardiology and neurology. As with many forms of technology, an increase in applications and demand has driven more rapid development.

Table 1: Comparison of *in vivo* imaging techniques [7, 8]

| Technique | Resolution | Application | Advantages | Disadvantages |
|-------------------|-----------------------|--------------------------------------|--|---|
| PET | 4 mm | Metabolic, functional and molecular | <ul style="list-style-type: none"> • Requires only small dose of tracer • Can image physiological processes • Tracers can have specific targets | <ul style="list-style-type: none"> • Low spatial resolution • Radiation exposure • Production of tracer can limit access |
| SPECT | 6-8 mm | Functional | <ul style="list-style-type: none"> • Multiple specific targeted tracers available | <ul style="list-style-type: none"> • Radiation exposure • Low spatial resolution |
| MRI | 1 mm | Anatomical, functional and molecular | <ul style="list-style-type: none"> • No radiation • Excellent for soft tissue • Functional imaging • Multiplanar imaging | <ul style="list-style-type: none"> • Long imaging times • Expensive • Can be difficult to interpret • Contraindicated in patients with metal implants |
| CT | 0.5 mm | Anatomical | <ul style="list-style-type: none"> • Good contrast range, especially for hard tissue/bone • Fast scan times, useful for emergencies • 3-D | <ul style="list-style-type: none"> • Soft tissue definition not as good as MRI • High radiation dose • Expensive |
| Ultrasound | 300-500 μm | Anatomical, functional | <ul style="list-style-type: none"> • Inexpensive • Real time • Can be portable • Good characterisation of vascular flow | <ul style="list-style-type: none"> • Operator dependent quality • Limited use in some organ systems, such as bone, lungs or bowels • Difficult interpretation of static images |
| X-Ray | | Anatomical | <ul style="list-style-type: none"> • Inexpensive • Fast • Simple • Readily available | <ul style="list-style-type: none"> • Imaging 3-D structures in 2-D • Radiation exposure • Low soft tissue contrast • Overlapping anatomy |
| Optical | 0.3 μm | Physiological and molecular | <ul style="list-style-type: none"> • No radiation • Low cost • More use analysing biopsies etc. | <ul style="list-style-type: none"> • Limited use in a clinical setting |

1.1.2.1 PET imaging

As a non-invasive technique that allows for quantitative measurements of biological processes *in vivo*, PET imaging has been investigated for its uses in multiple disease states. Although the primary focus has been on oncology, it is also used in neurology [7], cardiology [8] and autoimmune diseases [9-11], amongst others.

In 1928, Paul Dirac suggested the existence of a positively charged, sub-atomic particle, carrying the same mass as an electron [12]. These particles were later named as positrons by Carl Anderson, whose work with cosmic ray experiments in 1937 allowed for the movements of such particles to be observed.

When a positron collides with an electron, annihilation occurs, emitting two 511 keV gamma rays at approximately 180° from each other [12]. PET imaging takes advantage of this process. The gamma rays are detected by a series of scintillators, amplified by photomultiplier tubes, arranged in a ring formation around the patient. The gamma rays detected in coincidence allow for the calculation of their origin within the patient's body, with increased detection numbers providing more accurate images. The detection of both γ ray photons provides a line along which the annihilation must have occurred [13]. Further localisation is provided by multiple annihilations, with photons being detected in different directions allowing for triangulation.

Pairs of photons detected within a certain required timescale, usually around 5 ns, are considered to be coming from the same annihilation event. The idea was put forward to use the difference between the two times to provide a more precise location for the photons' origin, which would improve image quality and accuracy. Known as Time of Flight PET (TOF-PET), this became commercially available in 2006 using ultrafast detectors, such as barium fluoride (BaF_2), with a light decay time of less than 1 ns. The standard scintillator at the time, bismuth germanate ($\text{Bi}_4\text{Ge}_3\text{O}_{12}$ or BGO) had a response time of 300 ns [14, 15]. More scintillator materials have been developed since then, such as lutetium oxyorthosilicate or LSO (Lu_2SiO_5), which, along with improvements in electronics, allow for a location to be calculated to within approximately 9 cm along the known line of response. The newest PET scanners can have TOF performances close to 200 ps [15, 16].

The limitation of PET imaging resolution comes from the fact that positrons can travel a short distance, up to a few millimetres, before annihilation occurs and so it does not provide a 100% accurate indication as to their origin.

1.1.2.2 Combining PET and CT

Combining imaging modalities has been of major interest as far back as the 1960s, in order to gain as complete a picture of a disease as possible. This was achieved through the use of increasingly complex computer algorithms, to account for the images being acquired on different machines, often in different departments. While this was largely successful when imaging the brain, due to it being fixed in place within the skull with very little freedom to move, fusing images of the rest of the body proved complex, with organs able to move much more freely [17]. Limiting patient movement or positioning the patient in the same way was challenging.

One of the earliest attempts of combining PET with CT was in 1984 by Prof. Nagai *et al.* at Gunma University in Japan with a design consisting of the two scanners side by side and a single bed able to transport the patient between them. It was therefore possible to acquire both images without the patient leaving the bed and with minimal movement [17].

Townsend, Nutt and co-workers made the suggestion to combine PET with CT in a single scanner in the early 1990s, unaware of the previous design by Nagai *et al.* The Swiss oncology surgeon, Dr Rudi Egeli, suggested the gaps between the banks of BGO detectors on one of the machines earlier developed by Townsend and co-workers could be used to include another modality, such as CT, to provide anatomical information surgeons were more familiar with at the time [18]. Due to the components required for the CT scan and their density, this initially proved to be unfeasible.

Townsend and Nutt's work gained funding in the next few years, following on from work by Bruce Hasegawa and colleagues, who developed the first combined SPECT/CT prototype scanner [19]. The problem of space was overcome by positioning the PET components on the rear of the CT assembly. This meant they formed a single rotational assembly, gathering data sequentially [18]. The first prototype was operational in 1998, with the first commercial PET/CT scanners being offered in 2001 and rapidly becoming more common. The advantages seen in acquiring both PET and CT at the same time, providing attenuation factors for PET much faster, combining metabolic and anatomical data into a single image, simplifying image interpretation and allowing higher patient throughput, resulted in the major suppliers no longer building PET only scanners by just 2004 [17].

1.1.3 SPECT imaging

Unlike in PET, SPECT tracers decay emitting gamma rays directly, in a single direction, which are then detected by gamma cameras. Common SPECT radionuclides include technetium-99m or indium-111. Modern scanners usually have multiple detectors arranged around the patient, often with a variable

radius, which rotate to get a full 360° image. The variable radius can be useful for head scans, allowing for the detectors to be as close to the head as possible. The original scanners in the late 1960s achieved the image by moving the patient in front of a stationary camera [20].

SPECT imaging is often more widely available than PET, with more hospitals being equipped with SPECT scanners than PET scanners due to their lower cost. It is therefore a more practical routine procedure, but has a lower sensitivity than PET, due to the requirement of collimator inclusion [21].

With SPECT tracers emitting gamma radiation directly, rather than travelling a short distance before the annihilation event causing the emission, theoretically, SPECT should have higher resolution. However, the technology required for the detection of the gamma rays, and its limitations, results in PET imaging often having the better resolution in today's scanners.

One common clinical use for SPECT is in seizure disorders, such as epilepsy, allowing for comparisons to be made in blood flow within the brain during ictal and interictal states. The most commonly used tracer in this instance is [^{99m}Tc]Tc-HMPOA (Hexamethylpropyleneamine oxime), followed by [^{99m}Tc]Tc-ECD (ethyl cysteinate dimer). Both of these tracers cross the blood brain barrier and are lipophilic, achieving maximum uptake in brain tissue within 2 minutes, and being retained for up to 2 hours. They are therefore ideal to detect perfusion changes during the ictal phase.

Whilst interictal imaging is relatively easy, ictal-SPECT imaging requires the coordination of clinical and nuclear imaging teams, and often patient transport facilities, dependent on the location of the wards and scanners. The tracer, which clearly has a very limited shelf life due to its half-life, should ideally be injected within 15 seconds of the onset of a seizure and then scanned shortly after [22]. This limited timescale, and the often-unpredictable nature of seizures can mean it takes multiple attempts to obtain a good quality image, increasing the cost for the hospitals involved. It can also be an unpleasant investigation for the patient, requiring a short stopping of their medication to try to cause a seizure at the right time [22]. These investigations are used alongside further electroencephalogram (EEG) and PET/CT scans to locate the epileptogenic focus as specifically as possible, if MRI was unable to find a clear lesion.

1.1.4 Radionuclides used in molecular imaging

Radioactive isotopes are present in all groups of the periodic table, but not all are useful for clinical purposes, or, in some cases, are more useful for treatment rather than imaging. Basic properties of commonly used radionuclides are listed in Table 2. The most important properties regarding clinical uses are decay modes, chemical reactivity, availability and half-life.

Table 2: Half-life, decay modes and production methods of radioisotopes commonly used for clinical medical imaging

| Isotope | Half life | Decay mode | Production Method |
|--------------------------|-----------|---------------------------|--|
| ^{11}C | 20.3 min | β^+ (100%), 961 keV | Cyclotron $^{14}\text{N}(p,\alpha)^{11}\text{C}$ |
| ^{18}F | 110 min | β^+ (97%), 873 keV | Cyclotron $\text{H}_2^{18}\text{O}(p,n)^{18}\text{F}$ |
| ^{64}Cu | 12.7 h | β^+ (19%), 656 keV | Cyclotron $^{64}\text{Ni}(p,n)^{64}\text{Cu}$ |
| ^{68}Ga | 67.8 min | β^+ (89%), 1880 keV | $^{68}\text{Ge}/^{68}\text{Ga}$ generator |
| ^{44}Sc | 3.9 h | γ , 1157 keV | Cyclotron $^{44}\text{Ca}(p, n)^{44}\text{Sc}$, $^{44}\text{Ti}/^{44}\text{Sc}$ generator |
| ^{111}In | 67.2 h | γ , 245 keV | Cyclotron $^{111}\text{Cd}(p,n)^{111}\text{In}$ |
| $^{99\text{m}}\text{Tc}$ | 6.0 h | γ , 140 keV | Cyclotron $^{100}\text{Mo}(p,2n)^{99\text{m}}\text{Tc}$, $^{99}\text{Mo}/^{99\text{m}}\text{Tc}$ generator |
| ^{86}Y | 14.7 h | β^+ (33%), 1221 keV | Cyclotron $^{86}\text{Sr}(p,n)^{86}\text{Y}$ |
| ^{89}Zr | 78.5 h | β^+ (23%), 897 keV | Cyclotron $^{89}\text{Y}(p,n)^{89}\text{Zr}$ |

1.1.5 Radionuclide production

Production of a radionuclide can be done in four basic ways; charged-particle bombardment by a cyclotron (particle accelerator), radionuclide generator, neutron capture or nuclear fission. The latter two are not viable for on-site production for clinical radiopharmaceuticals, though can be used to produce the precursor (“parent”) isotope for a radionuclide generator [13].

In the case of cyclotrons, radionuclides are produced through the bombardment of stable nuclei with high energy ions. The ions (protons, deuterons or alpha particles) are accelerated to high kinetic

energy to overcome the coulomb barrier of the atom's nuclei. The name cyclotron comes from the spiral path the ions take as they are accelerated before being steered towards the target.

By their nature, and need for large amounts of shielding, cyclotrons are large and heavy machines requiring significant investment in infrastructure. This makes them impractical for most hospitals and so there are very few around, approximately 25 in the UK.

This is one of the reasons generators are more common, requiring much less investment in infrastructure and providing PET scanning facilities in more locations. Generators work by the continuous production of the required radionuclide through the decay of a chemical precursor with a significantly longer half-life, which can therefore be supplied more easily. The daughter radionuclide can then be eluted by an ion exchange process periodically. Commonly used radionuclides produced in this way are the PET isotope gallium-68, from germanium-68, and the SPECT isotope technetium-99m, from molybdenum-99. Other examples are given in Table 3 [23].

Table 3: Generator pairs and half-lives

| Generator System | Parent Radionuclide | | Daughter Radionuclide | |
|--------------------------------------|---------------------|------------------|-----------------------|----------------|
| | T _{1/2} | Decay Mode | T _{1/2} | Decay Mode |
| ⁵² Fe/ ^{52m} Mn | 8.28 h | β ⁺ | 21.1 min | β ⁺ |
| ⁶⁸ Ge/ ⁶⁸ Ga | 270.8 d | Electron capture | 67.8 min | β ⁺ |
| ⁷² Se/ ⁷² As | 8.4 d | Electron capture | 1.08 d | β ⁺ |
| ¹³⁴ Ce/ ¹³⁴ La | 3.16 d | Electron capture | 6.4 d | β ⁺ |
| ⁹⁹ Mo/ ^{99m} Tc | 2.75 d | β ⁺ | 6.01 h | γ |
| ¹¹⁸ Te/ ¹¹⁸ Sb | 6.0 d | Electron capture | 3.6 min | β ⁺ |

1.1.6 [¹⁸F]fluoro-2-deoxy-2-d-glucose

The clinical standard for PET imaging is the use of [¹⁸F]fluoro-2-deoxy-2-d-glucose ([¹⁸F]FDG), which is used to investigate several diseases, in particular being used for the staging, monitoring and planning for cancer [24]. The major advantage between the use of [¹⁸F]FDG PET imaging and other imaging techniques is the reporting of metabolic activity within the body, rather than structural. However, without being used alongside structural information, such as a CT scan, the clinical use of the

information provided is limited as the location of any tumour identified is hard to determine accurately.

Due to [¹⁸F]FDG showing all areas of high glucose uptake, such as in hyperglycaemic conditions or infections, this can affect scan accuracy and specificity [24]. For these reasons, targeted tracers such as Pentixafor, can be beneficial in disease diagnosis and monitoring of specific diseases. This does not mean that non-specific metabolic tracers, like [¹⁸F]FDG, do not have their uses, especially when screening for an unknown disease or primary cancers [25].

PET imaging through the use of [¹⁸F]FDG takes advantage of tumour cells having abnormally high levels of glycolysis to account for high metabolism, known as the Warburg effect [26]. Cancer cells also show abnormally high levels of glucose transporters (GLUTs), allowing the movement of glucose across the cell membrane along a concentration gradient. Once inside the cell, [¹⁸F]FDG undergoes the same phosphorylation process as glucose by the action of hexokinase to form [¹⁸F]FDG-6-phosphate ([¹⁸F]FDG-6-P), the normal process forming glucose-6-phosphate (G-6-P). Both [¹⁸F]FDG-6-P and G-6-P are unable to cross the cell membrane due to the presence of the charged phosphate group. G-6-P is metabolised further, transformed by phosphoglucose isomerase to form fructose-6-phosphate. However, as there is no hydroxyl group on the 2-position carbon, [¹⁸F]FDG-6-P cannot undergo this process and so remains “trapped” in the cell cytosol [14, 27, 28].

[¹⁸F]FDG has two main clinical uses; in locating sources of unknown disease, usually but not always of cancer, and of monitoring treatment efficacy [29-31]. When treating cancer patients, it is possible for treatment to be focussed on one specific form of cancer, when a secondary form may develop and be missed. Though these cases are not common, [¹⁸F]FDG scans lower the chance of these secondary cancers being missed. It also helps to find the primary source of a cancer in the first place, to then allow a more specific tracer to be used if deemed appropriate [25, 32].

Following up treatment responses and restaging cancers forms a major part of a treatment regime, especially with treatments with side effects such as those of chemotherapy. [¹⁸F]FDG is able to show responses to treatments with a high degree of accuracy, as well as detecting the occurrence of metastases [31, 32]. This allows it to be used to guide clinical decisions with confidence [33, 34].

As well as cancer, [¹⁸F]FDG is used to monitor other chronic diseases, such as ischemic heart disease and has been demonstrated to be powerful as a diagnostic tool to detect infections in patients supported with internal devices, such as continuous-flow left ventricular assist devices (CF-LVADs) [29, 35].

However, despite all these positives, [¹⁸F]FDG does have its downfalls. As already mentioned, it can detect multiple diseases. If the disease is unknown, it can be difficult to identify or differentiate between different positively identified sites, if multiple diseases are present. Further investigations are therefore required, often including biopsies. [¹⁸F]FDG has also been proven to have a low detection rate for certain cancers. This is particularly a problem for carcinomas with unknown primary location, with detection rates as low as 11% for small cell carcinomas [32]. For these reasons, it should be used selectively and not fully relied upon in all cases. False positives have been found in many cases, proven by biopsies or other methods to be benign or unidentifiable.

1.1.7 Classes of imaging agent

Multiple classes of imaging agents are in use, with different advantages and disadvantages. Sometimes, these properties are linked to the types of radioisotopes they are labelled with but some isotopes, such as gallium-68, can be used to label multiple classes of agents. Gallium-68 has a convenient half-life and, along with its ease of production, has led to it becoming one of the most widely studied and radioisotopes, allowing time for scanning but not giving high dose levels to patients [36, 37].

The choice of tracer design is often based on its desired use. For example, diagnosis or monitoring of a chronic inflammatory disease, a neurological disorder or a specific form of cancer, requiring tracers with different levels of specificity, biological half-lives and behaviours.

1.1.7.1 Peptide-based

Peptide receptors are often over-expressed in specific cancers, making them ideal for targeted tracers to be used for diagnosis, monitoring and treatment, depending on the isotopes used [38]. They can often be adapted without much difficulty to be labelled in different ways, either with a chelator for radiometals or using “click chemistry” with fluorine-18.

Targeting peptides can be identified in multiple ways; 1. From natural proteins known to bind with the wanted target, which can then be modified to be optimised further; 2. Structure based rational engineering and chemical synthesis; 3. Screening of peptide libraries [38].

A disadvantage to peptide-based tracers, particularly earlier ones, has often been their stability, with many having too short a biological half-life, sometimes in the region of minutes, to provide a satisfactory image. This half-life can cause them to lose their bioactivity before reaching their target, and clearly this is no use for a targeted imaging agent. This is often due to enzymatic degradation and

rapid renal clearance [38]. Major advances have been made in this area, the CXCR4 targeted T140 and the tracers developed as a result of its study being a good example of this, as discussed in more detail in section 1.4.2.1.

The success of gallium-68 has been largely due to work first reported by Henze *et al.*, whose report described the success of PET imaging of somatostatin receptor (SSTR) positive meningiomas with [⁶⁸Ga]Ga-DOTATOC [36, 39]. This led to a large increase in the development of somatostatin analogue-based tracers, labelled with gallium-68. So far, five SSTR subtypes have been discovered [40].

Early developments into SSTR imaging proved helpful in differentiating between neurinomas and meningiomas, as well as helping with the follow up to monitor metastatic disease. DOTATOC tracers were developed as an improvement on the previously used [¹¹¹In]In-diethylenetriaminepentaacetic acid octreotide ([¹¹¹In]In-DTPAOC) labelled SPECT tracers, which had the main drawback of lower spatial resolution and the limited sensitivity of SPECT compared to PET in detecting small meningiomas [39]. DOTATOC showed promising early results, allowing for tracers to be labelled with the positron-emitting generator gallium-68, as well as being rapidly cleared from the blood, with 80% being cleared within 10 minutes. Providing a high tumour-to-background ratio allowing tumours under 7 mm in diameter to be identified. It had been previously reported that [¹¹¹In]In-DTPAOC SPECT was not effective in detection of meningiomas with diameters under 2.7 cm [39].

Being able to differentiate between these different cancer types, as well as detecting which receptors particular tumours are expressing, allows oncologists to orient treatments to those that are most likely to be effective, and exclude treatments that are near certain to have no beneficial effect on the patient [41, 42].

Many SSTR tracers have now been investigated, including using technetium-99m as the label, with varying results. Of the technetium labelled tracers, such as [^{99m}Tc]Tc-vapreotide, [^{99m}Tc]Tc-depreotide (6-hydrazinonicotinic), [^{99m}Tc]Tc-EDDA-HYNIC-TOC and [^{99m}Tc]Tc-P829, only [^{99m}Tc]Tc-EDDA-HYNIC-TOC (or -TATE) proved to be superior to the earlier [¹¹¹In]In-pentetreotide at detecting SSTR+ tumours or metastases [37].

The generator production of gallium-68, rather than cyclotron, was another reason for the development of a tracer labelled with this isotope, though it has other advantages. One of these is that the detection of a tumour with a tracer labelled with [⁶⁸Ga]Ga-DOTATOC or [⁶⁸Ga]Ga-DOTATATE could lead on to its treatment with the analogous yttrium-90 or lutetium-177 labelled derivative [37].

1.1.7.2 Antibodies

Antibodies have been used for the imaging and treatment of chronic inflammatory diseases such as rheumatoid arthritis, multiple sclerosis and inflammatory bowel disease, amongst others. They have become increasingly utilised in recent years as they show a high specificity for their desired targets and can have a range of biological half-lives, depending on how they have been engineered [43]. They can also be aimed at different classes of targets, with each probe having a high level of specificity. These targets include cell adhesion molecules, surface markers on immune cells and cytokines, all of which can make them useful for monitoring the progression and therapeutic response of the previously mentioned diseases [43].

Full antibodies can be retained in blood plasma for a sustained amount of time and have slow elimination pathways (ranging from days to weeks) with relatively slow target binding and accumulation, in comparison to other types of imaging probes, which can be a drawback for targeted nuclear imaging agents [43, 44]. Using antibody fragments, nanobodies, or single chain variable fragments with lower molecular weights can achieve faster clearance speeds, with potentially enhanced biodistribution [43].

A major difficulty in the development of antibody-based probes targeted at specific diseases is many auto-immune, inflammatory diseases share mechanisms in their pathophysiology [45]. The difficulty is therefore finding a specific biomarker to target in the first place.

One of many success stories showing the potential of these biomarkers when found is in the treatment of breast cancer with Trastuzumab. Trastuzumab is a humanised monoclonal antibody that binds with the extracellular domain of human epidermal growth factor receptor-2 (HER-2), a receptor tyrosine kinase that is over expressed in 20-30% of human breast cancers [46]. Trials in the mid-90s showed women treated with chemotherapy alone experienced a 26.2% response rate. A combined treatment of Trastuzumab and chemotherapy provided a significant improvement, with the patients having a 62.0% response rate [47]. Concerns were seen regarding an increased risk of cardiac toxicity, which have remained in place, and so patients undergo cardiac assessment before treatment with Trastuzumab to assess the risk [48, 49].

By inhibiting the HER-2 receptor, Trastuzumab inhibits the growth of the cancer cells significantly, allowing other treatments, or the body's own immune system, to react more effectively against the abnormal cells that would normally grow out of control. This effect makes it most useful in early-stage cancers or in preventing recurrences. It is now standard treatment with Pertuzumab, alongside

chemotherapy in HER-2 positive breast cancer, being administered by intravenous infusion. Pertuzumab is an additional humanised anti-HER-2 monoclonal antibody, inhibiting HER-2 signalling. However, as they bind to different sites of the receptor, they have an additional anti-tumour effect [50, 51].

In 2016, Azad *et al.* reported a CXCR4 targeting, ^{89}Zr -labelled antibody showing preferential uptake in high CXCR4 expressing tumours [52]. Specificity and the diagnostic potential of the antibody was confirmed through blocking experiments. Their study showed the potential use of such an antibody for CXCR4 targeted immunotherapy as well as its radiolabelled counterpart for monitoring of the response to treatment [52]. Similar studies have resulted in multiple antibodies currently being in clinical trials for the treatment of multiple cancer types, including Ulocuplumab (BMS-936564/MDX1338), a fully human anti-CXCR4 antibody, for the treatment of chronic lymphocytic leukaemia [53, 54].

1.1.7.3 Small molecules

Small molecule tracers replicating the binding properties of peptides or antibodies are commonly preferred as they usually more stable and have improved clearance properties [44].

A well-researched carbon-11 tracer is the amyloid targeting compound N-methyl- ^{11}C 2-(4-methylaminophenyl)-6-hydroxybenzothiazole, given the name Pittsburgh Compound B (^{11}C PIB) in 2004 [55]. Its main use is to assess amyloid beta plaque disposition in Alzheimer's disease, with patients showing characteristic uptake in the frontal, temporal and parietal lobes and within the posterior cingulate and precuneus regions [14]. The predictive power of ^{11}C PIB has been shown to have prognostic value when detecting those patients who will progress from mild cognitive impairment, usually one of the earlier symptoms, through to Alzheimer's disease, although some of the data in this area is still to be followed up with further studies required [56].

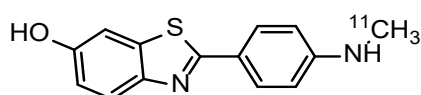


Figure 1: Structure of ^{11}C -Pittsburgh Compound B

Research into whether ^{11}C PIB would be useful for the prognostication of cardiac amyloidosis has also been ongoing, with initial results for a proof of concept appearing promising. Although, so far, it does appear to act as a significant, independent predictor of clinical outcome [57, 58].

[¹¹C]PIB's main drawback is the short half-life of carbon-11, just over 20 minutes, requiring the use of an on-site cyclotron and rapid synthesis of any tracers. Other tracers, such as Flortetapir, Flutemetamol or Flortetaben, get around this issue through the use of fluorine-18 instead [59-61]. However, this can also result in a higher radiation dose.

Though limited in its use clinically due to off-target binding, the tracer Tauvid received US Food and Drug Administration (FDA) approval last year for the imaging of tau pathology in potential Alzheimer's patients. As a first-generation tau tracer, it has proved a promising step forward in Alzheimer's prediction. Other tracers being developed at the same time had major problems, which limited their use [62].

A useful tracer to evaluate tumour response to treatment is the tracer 3-deoxy-3-[¹⁸F]fluorothymidine ([¹⁸F]FLT). [¹⁸F]FLT works in a similar way to [¹⁸F]FDG, in that it becomes trapped in the cell after being phosphorylated by an enzyme, in this case thymidine kinase 1 (TK₁). However, it is a measure of cell proliferation rather than metabolism. TK₁ activity reaches its maximum in the late G₁ and S phases of the cell cycle and is close to non-existent in non-proliferating cells. It is also reported to be four-five times higher in cancer cells than normal cells [63]. The greatly increased cell proliferation of many cancer tumours is a characteristic which can be targeted by [¹⁸F]FLT. An advantage [¹⁸F]FLT has over [¹⁸F]FDG is that it does not accumulate in inflammation [64].

Studies have shown that [¹⁸F]FLT has an important part to play when it comes to the assessment of therapy response, especially in cancers such as lung, brain and breast cancers. It is unlikely to replace [¹⁸F]FDG as a standard measure of cell metabolism but can be utilised alongside it, adding additional information in many cases [64, 65].

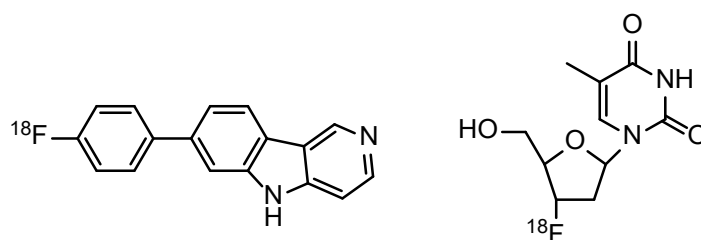


Figure 2: Structures of Tauvid (left) and [¹⁸F]FLT (right)

1.1.7.4 Nanoparticles

Nanoparticles form a framework on which tracers can be built, usually requiring surface functionalisation before such particles can be used in targeting and nuclear imaging.

Nanoparticles have the advantage of being able to fulfil multiple purposes. In the clinical field of molecular imaging, this can be as a simultaneous targeted PET and MRI probe [66]. As technology improves, this dual function may become more popular. Currently, integrated clinical PET/MRI machines are relatively rare in comparison to PET/CT, with only 30 in the US in 2017 compared to over 1600 PET/CT. This is partly due to cost, MRI machines being significantly more expensive, along with a lack of expertise in both the medical field to interpret the scan results and the technicians to operate scanners that cross nuclear and MR imaging technologies [67].

In the past few years, multiple new tracers have been synthesised and tested, most commonly using gallium-68 or copper-64, and iron oxide to provide the two functions. In 2016, Pellico *et al.* synthesised a chelator-free [⁶⁸Ga]Ga-iron oxide nanotracer, functionalised with RGD peptide, returning clear images for both PET and MRI. A small amount of accumulation was seen in the liver, which was reduced when tested without the attached RGD peptide [68].

The next year, the same group reported a neutrophil specific nanotracer, with the aim of quantifying lung inflammation. Again, they used gallium-68 and iron oxide with effective imaging results [69]. They had also demonstrated that the nanotracer could be modified to be aimed at different targets by changing the targeting vector on the particle surface. In this case, the peptide used was N-cinnamoyl-F-(D)L-F-(D)L-F (cFLFLF), which is hydrophobic and so has been limited in its use in nuclear imaging. However, it was thought the hydrophilic nature of the nanoplatform may be enough to overcome this problem and this was confirmed in the imaging results [69].

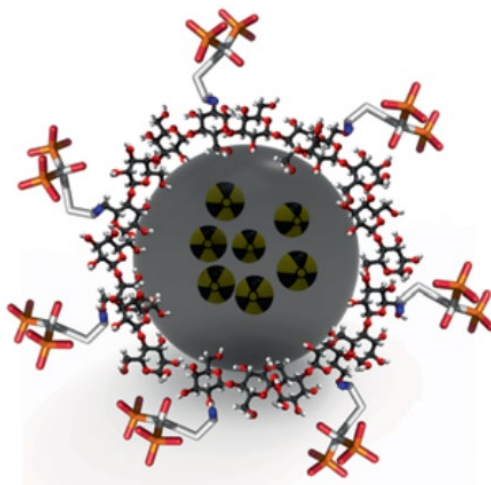


Figure 3: Structure of [⁶⁸Ga]Ga-NRT-c-FLFLF [69]

The developed [⁶⁸Ga]Ga-NRT-c-FLFLF tracer showed high specificity for neutrophils, as desired. There was a small amount of interaction with macrophages seen, but this was at low levels and significantly different to the neutrophil activity. The findings from the *in vivo* studies showed not only promising results for this specific tracer, but also demonstrated how the technology involved for nuclear imaging with nanoparticles could be used to overcome some of the limitations of more traditional techniques [69].

Nanoparticle based radiotracers have been synthesised to carry more than one targeting vector when targeting NSCLC [70], breast cancer [71] as well as recent work in the early detection of cardiac ischemia [72]. The dual targeting capability can allow for more efficient imaging. However, it can also result in a reduction in efficacy for binding to each target when compared to the single target tracer and this needs to be considered when developing these agents [70].

1.2 CXCR4

1.2.1 Chemokines and chemokine receptors

Chemokine refers to a family of chemotactic cytokine proteins, which are found in cells within the body's immune system, central nervous system and endothelial cells [73]. Initially discovered for their role in attracting immune cells to sites of inflammation, the role of the chemokine and chemokine receptors in to regulate the mobilisation of cells, leading to an easy link to the metastatic spread of disease [73, 74]. Currently, there are more than 20 different chemokine receptors known about, and a total of more than 50 chemokines with a known influence on a variety of biological functions [75].

Chemokines are made up of small proteins around 8-14 kDa in size and are divided into four categories according to the location of the first two cysteine residues, adjacent to the N-terminus, C, CC, CXC and CX3C [75, 76]. The larger number of chemokines compared to receptors implies several chemokines are able to bind to multiple receptors. Indeed, many of these pairings have been identified.

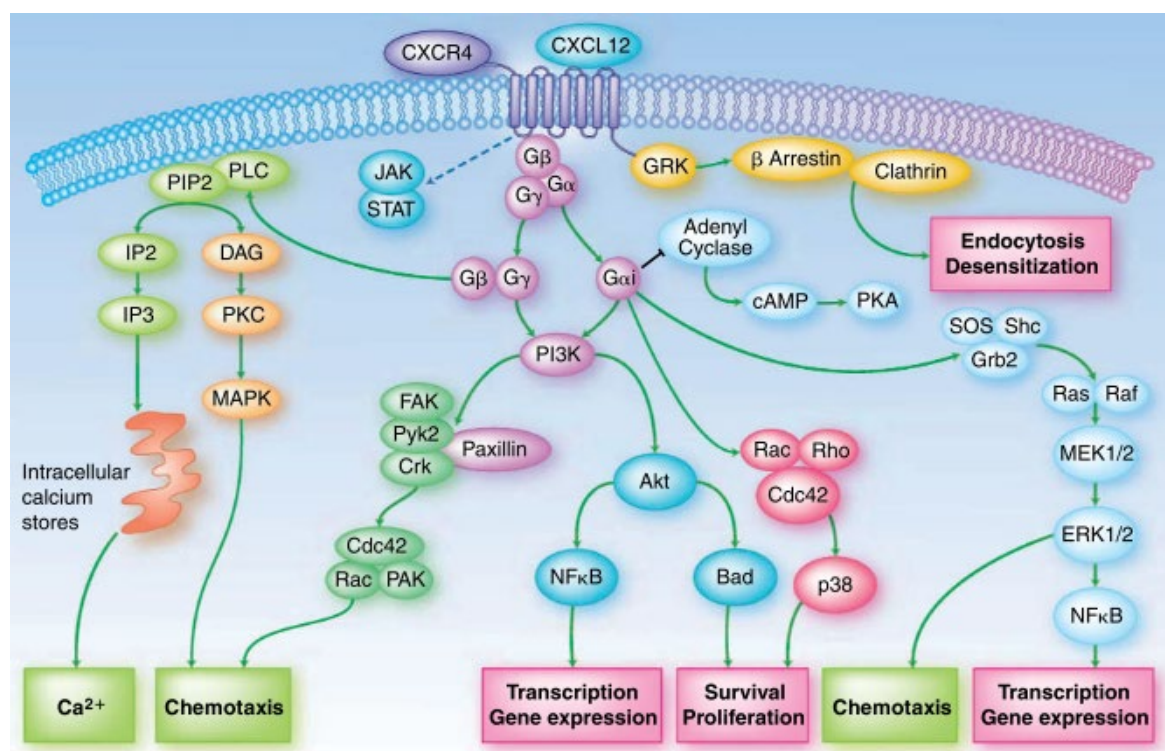


Figure 4: Schematic representation of CXCL12/CXCR4 pathway [77]

The biochemical signalling pathway of G-protein coupled receptors (GPCRs) is a complicated process with many components and may be tissue dependent, varying slightly between different cell types [77]. When a ligand binds with its cognate receptor, the intracellular domain on the receptor binds to a heterotrimeric G-protein on the inner surface of the cell membrane. The heterotrimer is made up of three subunits and formed from the interaction of Gβ with Gγ before binding to Gα. Activation of the

receptor by ligand binding leads to subunits' dissociation into a $\beta\gamma$ dimer and α monomer. There are four forms of $G\alpha$, each of which transmit the signal from the GPCR through slightly different routes. A schematic version of the CXCL12/CXCR4 pathway is shown in Figure 4 [77].

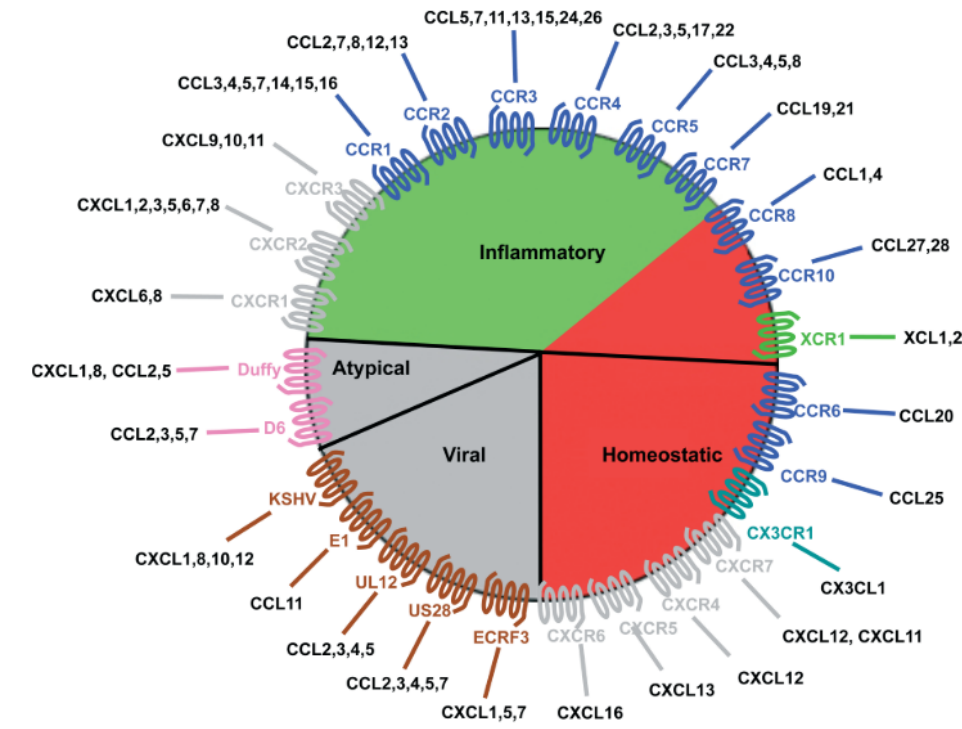


Figure 5: The Chemokine Wheel: From Balkwill [78]

Homeostatic chemokines are involved in the regulation, trafficking and homing of different cell types to ensure normal bodily function. Inflammatory chemokines, as the name suggests, regulate inflammatory processes, such as recruiting leukocytes to sites of inflammation. These two types, homeostatic and inflammatory, form the two main sub-groups of chemokines, see Figure 5 [76, 78]. Not all chemokines, however, carry out a single function with several showing both homeostatic and inflammatory functions [76].

The overexpression of many chemokines and chemokine receptors has been demonstrated to be associated with a large array of pathological conditions, including specific cancers, autoimmune diseases and infectious diseases [79]. Figure 6 shows some of the links between the diseases and chemokines that have been determined.

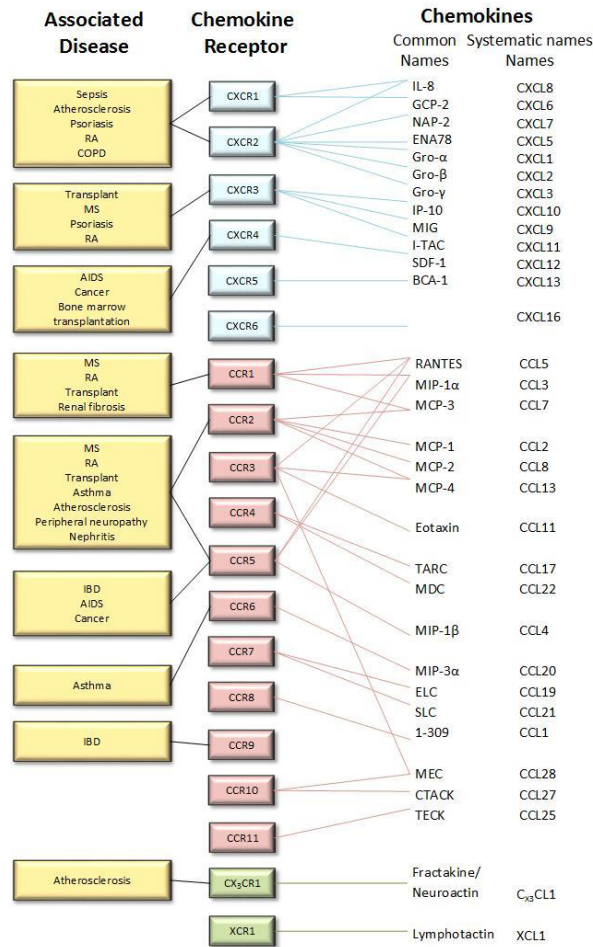


Figure 6: Diagram showing the sub-classes of chemokine receptors, their ligands and association to disease. The receptors for the CXC subclass are shown in blue, receptors for the CC subclass are in red and receptors for the C and CX3C class are in green. (Inspired by figures by Wells *et al.* and Proudfoot *et al.*) [80-82].

1.2.2 CXCR4

CXCR4 is a highly researched chemokine receptor, as a target for both imaging and drug therapy. It is a seven transmembrane helix GPCR consisting of 352 amino acids, roughly 40 kDa in size, and only binds with one ligand, stromal cell-derived factor-1 (SDF-1), also known as CXCL12, a small protein containing ca. 70-90 amino acid residues with four conserved cysteines forming two disulphide bonds. CXCL12 also binds to the receptor CXCR7, linking the function of these two receptors [83].

As well as being overexpressed in various diseases, CXCR4 plays an important role in the normal processes of haematopoiesis, neoangiogenesis, embryogenesis and inflammation. Mutations or abnormalities in the interactions between CXCR4 and CXCL12 during the embryonic stages of development lead to severe birth defects, including cardiac dysfunction and bone marrow defects [84].

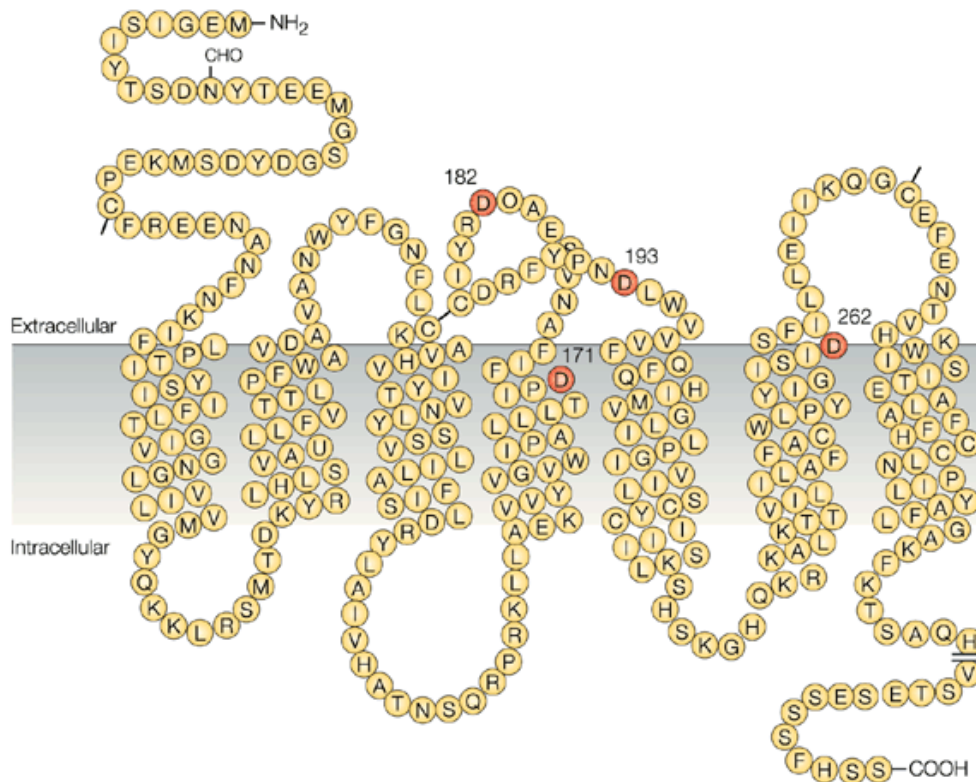


Figure 7: Representation of the chemokine receptor CXCR4, showing the seven transmembrane helices, using single letter amino acid codes with key aspartate residues highlighted. Reproduced from De Clercq, E. *Nat. Rev. Drug Discov.* 2003, 2 (7), 581–587. [86]

1.3 CXCR4 in Cancer

The involvement of CXCR4/CXCL12 in a range of both physiological and pathological processes has led to a substantial amount of biological, chemical and pharmaceutical research to further understand the mechanisms involved at a molecular level. The number of papers published on the topic of CXCR4 has increased rapidly over the past twenty years.

It is thought that cancer cells take over the CXCR4/CXCL12 axis during metastasizing and the formation of secondary tumours. Part of this is due to the high levels of CXCR4 expression in common sites of metastasis, including brain, lungs, lymph nodes, liver and bone marrow. CXCR4 over-expression has also been observed to be associated with poor prognosis [94]. It has been found to be overexpressed in 23 different cancers, including mammary, ovarian, prostate, oesophageal, pancreatic, melanoma, and renal cell carcinoma. It is also showed to be involved in the progression of several autoimmune disorders, including HIV [95-97].

Given the role of CXCR4 in normal biology, it is not surprising that it has been shown to be heavily involved in cancer physiology, especially tumour growth, angiogenesis and cell survival, with an important aspect in cell migration and metastasis [98].

The links between CXCR4 and the immune system, particularly the motility of neutrophils, have recently been under investigation. Interactions between host immune system neutrophils and cancer cells may play a part in the development of early metastatic events. At the same time, CXCR4 signalling has a major role in the innate immune response to these events, meaning the development of therapies targeted at this system is much needed [99]. It is however also clear that there is much more to be known about how each component interacts.

The link to a poor prognosis, often due to aggressive cancers or diagnosis after a cancer has metastasised, is the main reason CXCR4 has become of major interest for imaging and treatment, mainly in the field of oncology but also for the detection and treatment of the other previously mentioned diseases. Earlier detection and treatment of any disease, cancer or otherwise, is almost always linked to a better outcome for the patient.

More personalised, targeted treatment is also becoming more common, as more treatments can be aimed at specific cancer types and sub-types. For example, whilst it is still undergoing trials for various cancers, the diagnostic PET agent [⁶⁸Ga]Ga-Pentixafor may be able to predict a patient's response to its therapeutic counterpart, [¹⁷⁷Lu]Lu-Pentixather. Pentixafor is a CXCR4-targeting, cyclopentapeptide based tracer that is currently in clinical trials for PET imaging of several types of cancer. A patient who is shown to have high CXCR4 expression when imaged with [⁶⁸Ga]Ga-Pentixafor is likely to respond well to radionuclide treatment with [¹⁷⁷Lu]Lu-Pentixather in the future [100].

1.4 CXCR4 targeting tracers

1.4.1 CXCR4 targeting small molecules

Two common small molecules to target CXCR4 are AMD3100 and AMD3465, known for their anti-HIV activity due to binding to CXCR4 [101, 102]. During trials in healthy volunteers, AMD3100 was also found to unexpectedly be an efficient stem cell mobilising agent [103]. By blocking CXCR4 and preventing CXCL12 from binding, AMD3100 prevents CD34⁺ haematopoietic stem cell retention, causing a rapid increase in the peripheral blood and allowing for the harvest of these cells. Harvested cells can be returned to patients with haematological malignancies, such as multiple myeloma, following ablation treatment [104]. After further studies had validated this property, AMD3100 was approved by the US FDA in 2008 under the commercial name of Plerixafor, for use in patients with

multiple myeloma or non-Hodgkin's lymphoma who would undergo autologous haematopoietic stem cell transplantation [105-108].

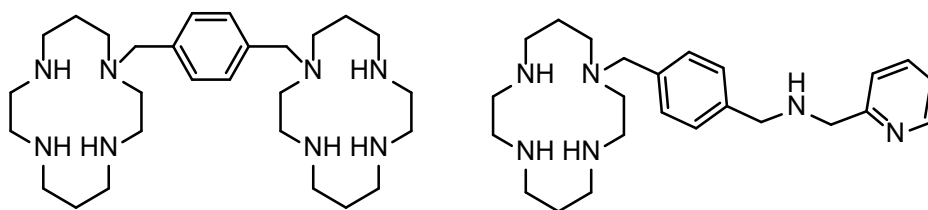


Figure 8: Structures of AMD3100 (left) and AMD3465 (right)

As azamacrocycles, such as the cyclams forming AMD3100 and AMD3465, are known to be effective chelators, a series of metal complexes was prepared and investigated. Multiple metal complexes of AMD3100 have been shown to display an increase in affinity for CXCR4, with zinc(II) and nickel(II), showing 36, and 50-fold increases, respectively [109].

Following these observations, the natural progression to radiolabelling the compounds was made initially with copper-64 by Jacobson *et al.* with [⁶⁴Cu]CuAMD3100, with multiple studies assessing the tracer *in vivo* shortly after [110-112]. Results showed good preferential uptake for CXCR4 expressing tumours but blocking studies revealed a potential issue with the tracer's *in vivo* stability, with the copper(II) ion not being retained. The issue was confirmed by the Archibald group more recently with stability assays and demonstrating the majority of activity from [⁶⁴Cu]CuAMD3100 injected *in vivo* was in the form of free copper(II) on excretion or extraction from the liver [113].

[⁶⁴Cu]CuAMD3465 was developed by de Silva *et al.*, and showed interesting results but is likely to suffer from the same stability issues. At 90 minutes after injection, the tumour-to-muscle and tumour-to-blood ratios were 7- to 8- higher than those of [⁶⁴Cu]CuAMD3100 [114]. However, as with [⁶⁴Cu]CuAMD3100, non-blockable uptake in the liver was seen, indicating loss of the metal ion and low complex stability. Derivatives of AMD3465 have also been reported to be radiolabelled with carbon-11 [115] and fluorine-18 [116, 117] *in vivo*. Both show high levels of liver uptake. A technetium-99m derivative for SPECT imaging has also been recently reported, and though results are promising, they are still at an early stage and *in vivo* stability remains unclear [118].

One factor that affects the binding of these cyclam based tracers and their ability to retain the copper ion is the configuration of the ring when in solution. When forming the metal complex, it is possible for the cyclam to form six different configurations, see Figure 9. While preferred configurations appear to be affected by the presence of other ligands, multiple configurations have been shown to be

present in the same solution as well as the ability to change configuration, showing that they are in equilibrium [119, 120]. Sadler *et al.* reported that whilst trans-III was the most common configuration of cyclam, others can be favoured by N-substitution, ternary complexation or interaction with other solvents in solution [119]. For example, acetate can induce the formation of cis-V configuration, while it has been shown that trans-III complexes of zinc–cyclam complexes (with acetate, phthalate, perchlorate or chloride as counterions) equilibrates to form mixtures of cis-V, trans-I and trans-III isomers, usually over the course of hours [121, 122].

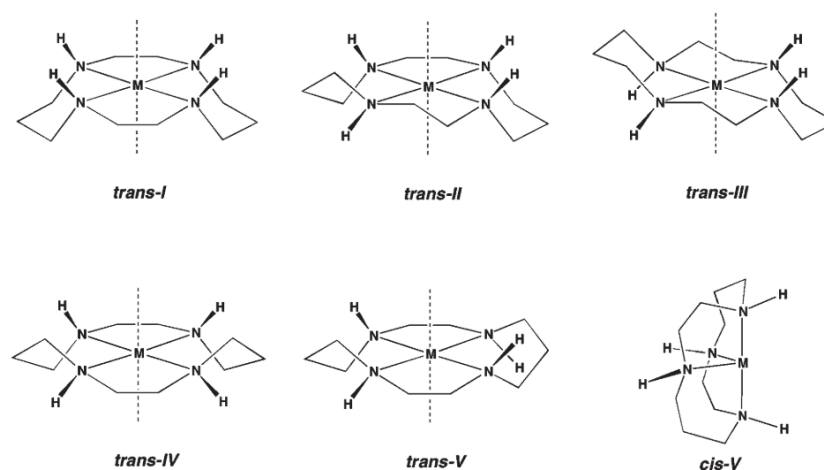


Figure 9: The six configurations of metal-cyclam complexes [123]

With the binding ability of cyclam being affected by its configuration, the ability to constrain the compound into a single configuration has the potential to be of major importance, particularly when it comes to designing a targeted tracer. The flexible cyclam molecule with a transition metal ion coordinated will adopt the most stable configuration that matches the binding cavity on the target receptor. In the case of AMD3100 (or related molecules) binding to CXCR4, *in vitro* receptor binding assays show cis-V has the highest affinity for the receptor [120, 122]. The configuration can be locked in place though the use of an ethylene chain introduced between two adjacent nitrogen atoms or two non-adjacent nitrogen atoms, a side-bridge (SB, *via* steric effects) or cross-bridge (CB, *via* mechanical restriction) respectively.

The introduction of a side bridge was first reported by Wainwright in 1980, while the preparation of the cross-bridge was reported in 1990 by Weisman [124, 125]. Studies into both of these structures showed they formed a single configuration of the cyclam, SB-cyclam forming trans-II due to the steric bulk and CB-cyclam forming cis-V, due to the mechanical restrictions [126-128]. For CB-cyclam, this results in an increase in kinetic inertness of the metal complexes, with four convergent nitrogen lone

pairs coordinating the metal centre in the cavity [123]. CB-Cyclam was developed by Hubin and Busch, in collaboration with Proctor and Gamble company, for application in catalysis. The Archibald and Hubin groups have developed advanced novel synthetic methodologies that are scalable and address prior bulk production challenges whilst also increasing efficiency with shorter production timescales, and widening the range of derivatives that it is possible to synthesise [129-132].

Following on from this work, Archibald and co-workers prepared a bis-macrocylic compound with the same para-xylyl cross-bridge as AMD3100, CB-Bicyclam, along with its Cu(II) metal complexes, which were then assessed for their CXCR4 affinity *in vitro*, see Figure 10 [133].

Before the metal is inserted, the ligand only has a low affinity for the CXCR4 receptor ($IC_{50} > 5 \mu M$). However, once the metal centres have been inserted into the cyclam cavities, the affinity for CXCR4 increases significantly. CuCB-Bicyclam has an IC_{50} of 7.9 nM whereas Cu_2CB -Bicyclam has an IC_{50} of 3.1 nM, the higher affinities being attributed to the Cu(II) complex being rigidly locked in a cis-V configuration, reported to be the configuration producing the best binding ability for CXCR4 [113, 120, 122, 134]. Site directed mutagenesis studies on the CXCR4 receptor show that the same aspartate residues that are relevant to AMD3100 binding (Asp171 and Asp262) have a role in the binding of the cross bridged bicyclam compounds.

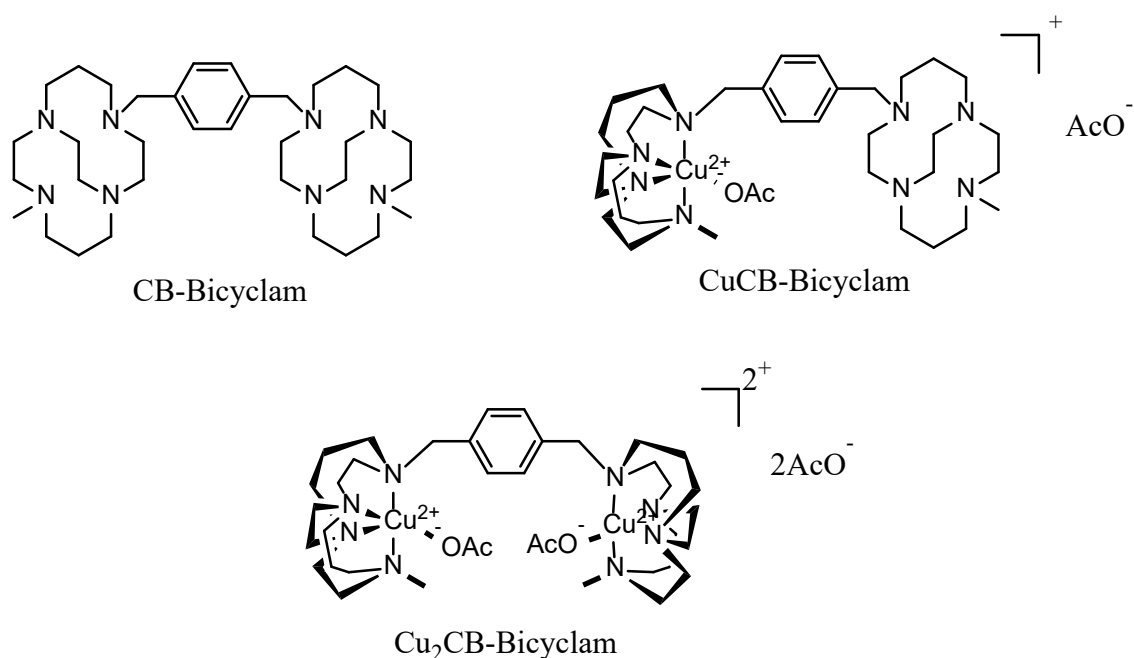


Figure 10: Structures of the configurationally restricted CB-Bicyclam and its corresponding copper complexes

Based on these published reports, Nimmagadda and co-workers produced derivatives of AMD3465, RAD1-24 and RAD1-52, with cross-bridges leading to similar increases in CXCR4 affinity in *in vitro* testing, although radiolabelling did not deliver stable copper-64 labelled compounds [135].

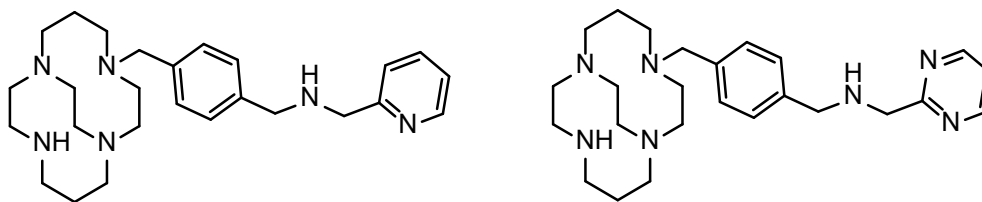


Figure 11: Structures of RAD1-24 (left) and RAD1-52 (right)

1.4.2 Peptides as imaging agents

1.4.2.1 T140 and its derivatives

Much of the work into peptides for binding to CXCR4 was started by Nakashima *et al.*, looking for anti-HIV activity [136]. T140 (Arg¹-Arg²-Nal³-*cyclo*(Cys⁴-Tyr⁵-Arg⁶-Lys⁷-D-Lys⁸-Pro⁹-Tyr¹⁰-Arg¹¹-Cit¹²-Cys¹³)-Arg¹⁴, see Figure 12) was found to be the most active of the compounds tested.

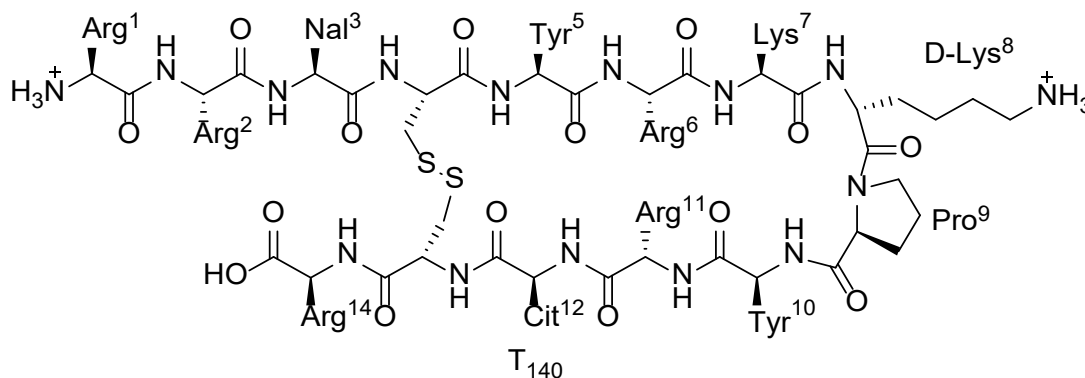


Figure 12: Structure of T₁₄₀

Further investigation in the late 90s and early 00s into T140 showed the peptide binds to the CXCR4 receptor at the C- and N- terminus *via* 4 key residues, Arg², Nal³, Tyr⁵ and Arg¹⁴ [137, 138]. Since then, derivatives of T140 have become one of the most studied classes of CXCR4 antagonist due to their high specificity for the CXCR4 receptor and their low nanomolar affinity. They did, however, have some problems, including cytotoxicity due to the high net charge on T140 and a poor metabolic stability in serum [139]. Several modifications have been attempted over the years to reduce these issues. The most successful of these was Ac-TZ14011, which benefitted from the addition of a carboxyl group on to Arg¹, through amidation [140].

The first radiotracer produced from a T140 derivative was reported by Hanaoka *et al.* in 2006, in the form of a ^{111}In -labelled SPECT tracer. They conjugated DTPA to Ac-TZ14011 and radiolabelled with indium-111. Despite a partial tumour uptake in nude mice bearing pancreatic tumours and significant difference in blocking studies (blocked with 10 mg/kg unlabelled TZ14011), [^{111}In]In-DTPA-Ac-TZ14011 was not suitable for further investigation as it also showed a high uptake in non-CXCR4 expressing organs [140].

The first PET imaging agent formed from T140 was an ^{18}F -labelled derivative, with a radiolabelled fluorobenzoyl group at the N-terminus. [^{18}F]-T140 had several advantages, including a tumour to muscle ratio of 20.6, but required a co-injection of a non-radioactive compound to prevent non-specific binding to red blood cells. It also had a long synthesis time, with a low yield, so further development was required for it to be fully viable [141].

Another derivative of T140, Ac-TC14012, was investigated for radiolabelling with fluorine-18 in 2013, by Zhang *et al.* [142]. They investigated two variants, attaching either a fluorobenzoyl or fluoropropionate at Lys⁷. Both showed significantly higher accumulation in CXCR4-positive tumours compared to CXCR4-negative tumour xenografts in mice and provided clear visualisations of CXCR4 expression by PET. Between the two, the fluoropropionate variant showed a better tumour-to-background contrast, as well as a higher tumour uptake. Tumour uptake was also increased when blocked with low dose cold peptide [142]. In comparison to the previous N-terminal fluorobenzoyl variant of the radiotracer, both of these showed reduced RBC binding, leading to minimal blood retention. From these results, it is clear the location of additional groups on the T140 peptide framework plays an important role in the prevention of non-specific interactions, however further studies are required to fully elucidate the importance of each residue to overall binding efficacy and selectivity .

Derivatives of T140 to allow for facile copper-64 radiolabelling were investigated by Jacobson *et al.*, by including the chelators NOTA or DOTA on the N-terminus of the peptide [143]. A similar variant, this time with the chelator on the D-lysine⁸ residue and a 4-fluorobenzoyl group on the N-terminus, was reported by Hennrich *et al.*, who radiolabelled with gallium-68 instead [144]. The approach of using chelators allows for the use of different PET or SPECT radiometals, also including the possibility of therapeutic isotopes.

The possibility of including two DOTA bifunctional chelators (BFC)s was also investigated by Jacobson *et al.*, with one on each lysine residue (T140-2D). Initial investigations showed it was easy to radiolabel

with copper-64 in high yields. The main issue with these compounds was unexpected binding with red blood cells (RBC), as functional groups were included that had previously been shown to reduce this interaction. A co-injection of unlabelled T140-2D increased the tumour-to-muscle and tumour-to-blood ratios, 4.86 ± 0.89 and 12.56 ± 3.66 , respectively [145]. Overall, the radiotracer biodistribution was less optimal than the fluorine-18 analogues as higher uptake and retention was observed in the liver and kidneys slowing the clearance of the tracer and creating background signal on the imaging timescale [145]. Similar results were observed when the construct was radiolabelled with gallium-68 instead of copper-64.

During their investigations of [^{64}Cu]T140-2D, Jacobson *et al.* carried out research into the binding with RBC seen in T140 derivatives [145]. Although CXCR4 is not expressed, RBC do express scavenger receptors, such as Duffy antigen receptor of chemokine (DARC), which is able to bind to various chemokines and so was suggested as a possible explanation for the unwanted non-specific binding [146]. However, no difference was seen in blood uptake when [^{64}Cu]T140-2D was tested between DARC knockout mice and wild-type mice, effectively eliminating DARC as the binding site.

1.4.2.2 Cyclopentapeptides

A goal in the development of CXCR4 targeted imaging agents has been to discover a low molecular mass agent, in comparison to the natural ligand for CXCR4, SDF-1, which consists of around 67-residues and has a molecular mass of nearly 8000, depending on its level of processing [138].

Alongside the further development of T140, efforts have been made to produce smaller, more metabolically stable peptides, based on the known structure and antagonistic actions of T140. This led to the design and synthesis of two cyclic pentapeptide isomers, *cyclo*[Nal-Gly-D-Tyr-Arg-Arg] (FC131, $\text{IC}_{50} = 8 \text{ nM}$) and *cyclo*[Nal-Gly-D-Tyr-D-Arg-Arg] (FC131(D-Arg), $\text{IC}_{50} = 4 \text{ nM}$) [147]. Studies on both peptides investigating the importance of each of the side chain functional groups, using alanine replacements, showed reduced CXCR4 affinity upon each replacement [148]. Further studies, using the N-methylation of the different amino acids, showed the Arg³ and Nal⁴ residues are essential to CXCR4 binding affinity. The N-methylation of D-Arg² led to a doubling of CXCR4 affinity, in comparison to the parent peptide, suggesting the amide bond orientation between the tyrosine and methylated arginine is important for receptor interaction [148]. The cyclic structure of the peptide produces a high level of *in vivo* metabolic stability and low susceptibility to degradation by peptidases.

FC131 has been of increasing interest in recent years, having the possibility to be radiolabelled with a range of different isotopes. Chelators such as DOTA can be attached (for labelling with gallium-68), it

can be reacted with p-fluorobenzaldehyde or “click chemistry” can also be used to link to a fluorine-18 precursor [149-152]. Labelling with iodine-124 has also been attempted, with promising CXCR4 interaction, but high liver and intestine uptake was observed, attributed to its high lipophilicity (tumour-to-liver and tumour-to-intestine ratios of 0.3 and 0.6 respectively) [152].

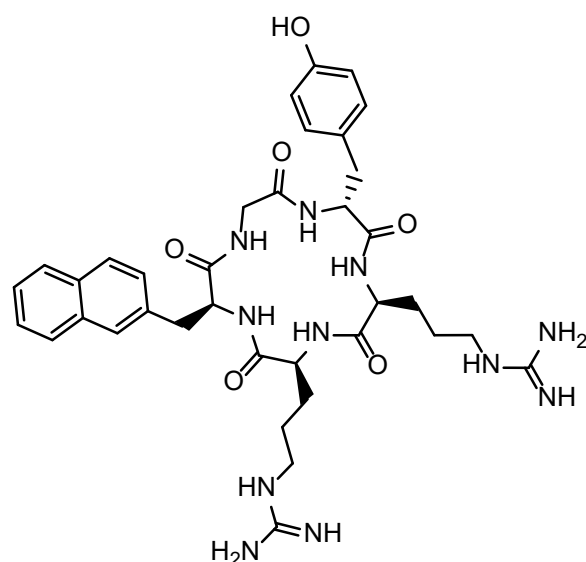


Figure 13: Molecular structure of CXCR4 binding peptide FC131

Demmer *et al.* further optimised the structure of FC131, allowing for the introduction of an aminomethylbenzoyl spacer (AMBA) before the DOTA chelator, substituting Arg⁵ for a D-Orn residue [153]. This new structure was renamed CPCR4-2. It is noted during testing of CPCR4 based tracers, [⁶⁸Ga]GaCPCR4-2 shows no binding to murine CXCR4. This means that preclinical studies in mice will show a high tumour to background contrast as there is no binding to naturally expressed CXCR4 in tumour tissues [154].

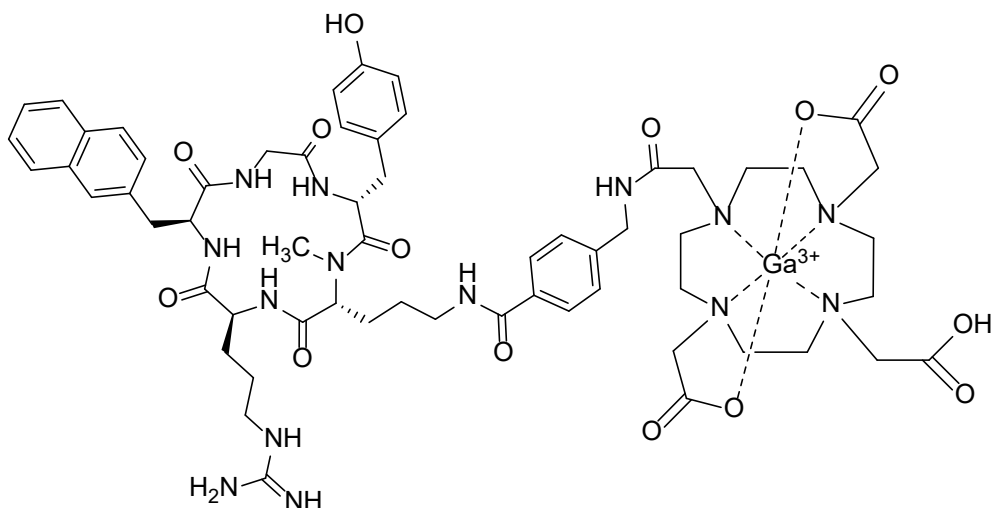


Figure 14: Molecular structure of CXCR4 targeted imaging agent [⁶⁸Ga]Pentixafor

The unlabelled CPC4-2 has a much higher IC₅₀, indicating a lower affinity, than FC131 (177 and 4.4 nM respectively) [152]. [⁶⁸Ga]Pentixafor was formed in 2011 by Gourni *et al.*, who reported the inclusion of DOTA and the radiolabelling with gallium-68. Interestingly, when complexed with gallium(III), [⁶⁸Ga]Pentixafor becomes more potent with the IC₅₀ decreasing to 5 nM[152]. The exact reason for this increase in affinity has yet to be identified but it is more likely to be due to charge neutralisation (reducing unfavourable electrostatic interactions) than direct binding interactions between the gallium(III) DOTA complex and the receptor target.

The rapid success of [⁶⁸Ga]Pentixafor in pre-clinical studies led to it quickly advancing to human trials. The dosimetry and biodistribution were studied by Hermann *et al.* by imaging and assessing five multiple-myeloma patients who were injected intravenously with 90 – 158 MBq of [⁶⁸Ga]Pentixafor (134 ± 25 MBq). This showed very promising results and low toxicity, delivering absorbed doses to organs lower than those delivered by [¹⁸F]FDG or ⁶⁸Ga-labeled somatostatin receptor ligands [155].

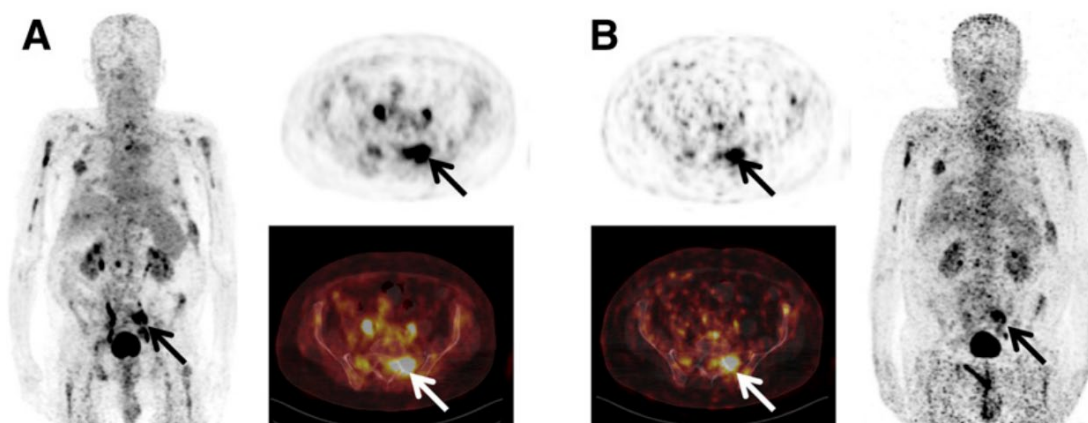


Figure 15: Example of $[^{68}\text{Ga}]$ Pentixafor scan in multiple-myeloma patient. Shown are maximum-intensity projections and transaxial slices at 40 (left) and 236 (right) minutes after injection.

Following this initial success, trials progressed quickly to test its diagnostic abilities in various malignancies including multiple myeloma [156], small cell lung cancer [157], breast carcinoma [158] and chronic bone infection [159]. A more recent paper reported the imaging of pulmonary cryptococcosis in a patient who had been treated for multiple myeloma [160].

The use of DOTA as a chelator allows for a choice of radioisotopes, including the option of therapeutic isotopes such as lutetium-177 or yttrium-90. $[^{177}\text{Lu}]$ Pentixather, a ^{177}Lu -radiolabelled analogue of Pentixafor, has been prepared, shows good pharmacokinetic properties and favourable overall dosimetry [161]. Related Pentixafor based analogues have been synthesised, including $[^{68}\text{Ga}]$ NOTA-Pentixafor [162] and an ^{18}F -analogue [163] in attempts to increase availability of the tracer by either simplifying radiolabelling or using isotopes with longer half-lives.

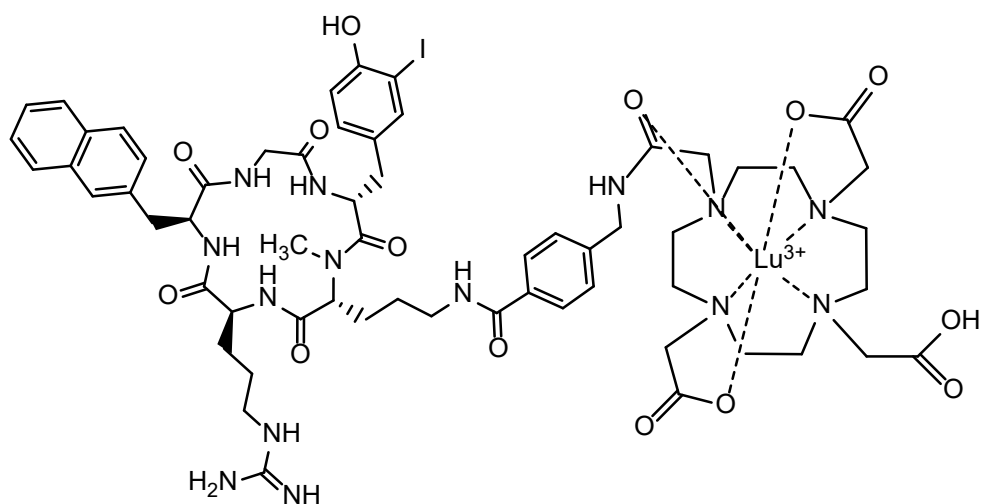


Figure 16: Molecular structure of [¹⁷⁷Lu]Pentixather

Yttrium-90 labelled Pentixather has also been trialled in patients with advance stage myeloma, with more studies ongoing [40, 164].

1.4.2.3 Novel peptide-based tracer design

The design of any new tracer depends on the required characteristics of the tracer and, in some cases, can be informed by data from validated tracers or those in development. In this case of CXCR4 targeting, there is an unmet need for a fluorine-18 tracer due to established infrastructure for production and supply.

The development of various cyclopeptides, such as FC131 and, more recently, pentixather, has shown the cyclic structure provides a higher metabolic stability in comparison to linear peptides. It has also established an *in vivo* profile and structure-activity relationships, informing potential sites for modifications. This can be seen in cases such as in the development of pentixather, which has a very similar peptide structure to pentixafor [163].

The method for tracer labelling with the fluorine-18 isotope must also be considered as part of the design. [¹⁸F]Pentixather uses an aluminium-¹⁸F fluoride complex ([¹⁸F]AlF), with a NOTA chelator, a method commonly used in recent years for ¹⁸F-labelling. However, this resulted in a significantly higher lipophilicity than desired and so further pharmacokinetic optimisation is needed [163]. [¹⁸F]AlF is a method that has made it into clinical trials in a variety of tracers and is being developed for clinical use in the near future [165]. An alternative method that is under widespread investigation is the use of “click” chemistry.

1.5 Click reactions

1.5.1 Click chemistry

“Click” chemistry is an approach that is defined by a set of stringent criteria, defined by K. B. Sharpless. To meet these criteria, a process must be “modular, wide in scope, give very high yields, generate only inoffensive by-products that can be removed by non-chromatographic methods, and be stereospecific (but not necessarily enantioselective)”. The reaction conditions must be simple, ideally insensitive to oxygen and water. Reaction materials and reagents must be readily available and ideally require no solvent, a solvent that is benign or easily removable and the product must be simple to isolate and be stable under physiological conditions [166].

Several processes have been identified or developed to meet these conditions;

- Inverse Electron Demand Diels-Alder reaction (IEDDA)
- Copper-Catalysed Azide-Alkyne Cycloaddition (CuAAC)
- Huisgen 1,3-dipolar cycloaddition
- The Staudinger-Bertozzi ligation
- Strain-promoted alkyne-azide cycloaddition (SPAAC)

1.5.2 Pre-targeted imaging

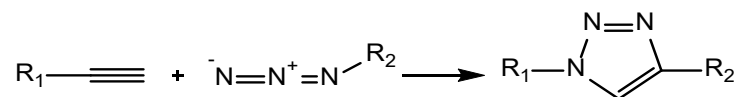
One significant example of the usefulness of “click” chemistry, is the use of pre-targeted PET imaging. A non-radiolabelled molecule with a reactive tag is injected into the patient and allowed time to bind to the biological target, as well as non-bound molecules to clear the system. The radiolabelled compound, with the complementary reactive tag, is then injected. This will rapidly and selectively react with the bound, pre-targeted molecules at the desired receptor. As before, time is allowed for this molecule to disperse, the reaction to occur and unreacted molecules to clear the system [167]. The image can then be taken as normal in the scanner.

The technique allows shorter half-life radioisotopes to be used, that would not normally be suitable for direct imaging with biological molecules such as antibodies. Larger peptides can also be used as the targeting molecule, allowing for increased clearance, and so achieving higher tumour-to-blood ratios [168].

To be applicable in pre-targeted imaging applications, where the conjugation reaction is performed *in vivo*, the reaction must be biorthogonal (i.e. not interacting with the biological system). Unfortunately, not all forms of “click” chemistry are either biocompatible or biorthogonal, utilising toxic catalysts or

reagents in the reaction. For example, the Copper-Catalysed Azide-Alkyne Cycloaddition (CuAAC) reaction requires a toxic copper catalyst. However, the Inverse Electron Demand Diels-Alder (IEDDA) reaction, is an example of a suitable biorthogonal process that can be used *in vivo* [169].

1.5.3 Copper-Catalysed Azide-Alkyne Cycloaddition



Scheme 1: The Copper-Catalysed Azide-Alkyne Cycloaddition “click” reaction

The most common “click” reaction is the Copper-catalysed Azide-Alkyne Cycloaddition (CuAAC) reaction. This reaction has been used in many fields of research due to its high stability and, with the assistance of the catalyst, high reactivity. The 1,2,3-triazole ring also shows various biological activities, including anti-bacterial and anti-allergenic effects. [170].

CuAAC reactions have been used for radiolabelling peptides for several years, as a reliable and efficient method for general ¹⁸F-labelling. Initially “click” reaction studies had varied results, with labelling efficiency ranging from 5% to near 100%, depending on factors such as peptide concentration, temperature, copper to alkyne ratio and reaction time [171]. The development of “click” chemistry in radiolabelling provides a quick method for testing a large range of potential tracers in a short amount of time, with small variances in structure between each derivative. There are now examples of the application of “click” chemistry being used in GMP radiotracer synthesis and taken through to clinical trials. In particular Aboagye and co-workers have developed a fluorinated octreotide for neuroendocrine tumour imaging that has a favourable safety and dosimetry profile along with high quality imaging results [172, 173].

As well as being used to attach radiolabels, as in this case, CuAAC has a wide range of applications. A review by Castra *et al.* details the suitability of this reaction for building peptides, nucleotides, polymers, supramolecular structures, and small molecules. In particular, the use of CuAAC in solid phase synthesis has been investigated [174]. For peptides, CuAAC can be used as an alternative to the standard amide bond formation for functionalisation, as well as creating amino acid triazole derivatives and new resins. It is also applicable as a method for cyclising peptides [174]. The mechanisms behind the reactions, and the intermediate the catalyst forms have been studied by multiple research groups, including recently by Fang *et al.*, who managed to capture the intermediate [175].

1.6 Research aims

Almost all cancer treatments have a harmful effect on the body, the more targeted the treatment can be is therefore significant, along with being able to detect cancer early to eliminate risk of metastases. The ultimate goal of this work is to develop a tracer to allow accessible targeted CXCR4 imaging in patients. An easily modifiable design should allow for the *in vivo* kinetics to be optimised to provide the high-quality imaging data. Ideal images have minimal background noise, including a high ratio of uptake between the tumour and other organs. In particular, the liver, gallbladder and gut are of relevance due to the excretion/ retention of previously developed fluorine-18 analogues having significant non-specific uptake in these organs.

The main aims of this research are to synthesise and purify a CXCR4 targeting, CPCR4 based peptide, with a variety of polyethylene glycol (PEG) chain linkers attached. A further variety of PEG chain linkers will then be “clicked” onto this, with ¹⁸F isotopes as labels. This research builds on work done by the Archibald group, that has managed to synthesise a fluorine-18 labelled- CXCR4 targeting tracer, using an AMBA linker. That derivative was excreted *via* the biliary system due to its lipophilicity, unlike Pentixafor, which is excreted *via* the bladder.

This research and the longer PEG chains could address this issue, making the tracer less lipophilic, while maintaining its binding properties. A fluorine-18 labelled tracer, instead of the current gallium-68 labelled Pentixafor, would increase accessibility of the tracer *via* current infrastructure for clinical supply.

Chapter Two: Results/Discussion

2.1 “Click” radiolabelling strategy

The pharmacokinetic properties of any substance to be used within the body are very important as they will dictate how the compound interacts with the body, how it is absorbed, distributed and metabolised, and excreted from the body. For radiotracers, this can have a dramatic effect on the quality of the images obtained by increasing target accumulation and reducing background signal. PEG linkers have been used to optimise drug delivery, increasing the concentration in target locations, therefore increasing the drug’s efficacy [176].

With any tracer, compound not bound to the specific target should be rapidly cleared to reduce background signal otherwise it will reduce image clarity. Usually, this is *via* the kidneys and bladder and the optimal imaging timepoint is often 20-30 minutes after the administration of the radiotracer. For cancer imaging, this reduces the potential to miss small tumours and metastases that might be masked by background signal.

[¹⁸F]AlF complexes were not pursued in this work, instead favouring the option of “click chemistry”. This allows for simple modifications to be made in the spacer chain between the peptide and the isotope, as well as providing rapid synthesis techniques with few to no impurities for facile purification.

Labelling the tracer *via* a covalent bond, can be achieved with the fluorine-18 being attached to a variety of atoms. Elements commonly used for this purpose, which fluorine-18 will form a stable bond to, include carbon, boron, silicon and sulphur. Some require the use of high temperatures to achieve good radiolabelling yields.

“Pegylation” has been used for a number of purposes for decades, primarily for the modification of the *in vivo* kinetic properties of a variety of pharmaceuticals and radiotracers [177]. However, the introduction of long PEG chains into radiotracers, some hundreds or thousands of carbons long, has also been shown to have a negative effect on the receptor binding ability and tissue uptake of several radiotracers [178]. Research into the use of shorter PEG chain chains, referred to by some as mini-PEGs, in the region of 10-carbons in length has shown to minimise this problem while still influencing pharmacokinetic properties [178-180].

A major effect of the addition of a PEG chain to a drug or tracer is an increase in hydrophilicity, potentially altering the excretion mechanism with a higher likelihood of the preferred renal excretion. PEG chains are also used to increase residence time in the blood pool which can increase target accumulation, although this has to be balanced against slow clearance that will generate background

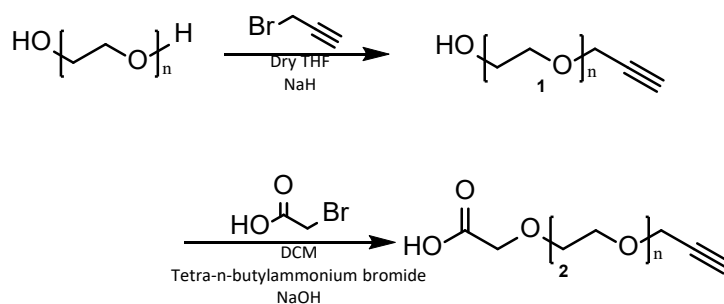
signal. Some tracers based on peptides such as FC131 are already highly lipophilic, due to inherent properties and addition of chelators for radiolabelling. The chelator DOTA is highly hydrophilic, and so when used to form Pentixafor, the final radiotracer is sufficiently hydrophilic to be excreted through the renal system. However, previously studied fluorine-18 derivatives of the same peptide do not have this advantage and so further modifications are required. The aim in this research is to develop a tracer that (i) can be labelled in high radiochemical yields, (ii) possesses favourable decay characteristics, (iii) has potent receptor affinity and (iv) has optimal *in vivo* kinetic properties.

The linkers selected for this tracer were synthesised in two parts. The first contained an acid group for coupling to the peptide, and an alkyne group to be “clicked” to the other linker. The second contained an azide group, forming the other component of the “click” reaction, and a tosyl group, for reaction with the fluorine-18 isotope for radiolabelling. The varying lengths of PEG chain in each component were used to investigate how PEG chains affect the binding potency and lipophilicity of the tracer. These modifications can alter how a radiotracer is excreted, with excretion *via* the kidneys preferred, rather than retention or metabolic processes in the liver.

2.2 PEG_x linker synthesis

2.2.1.1 CC-PEG_n-COOH synthesis

Short PEG linkers of defined length were used in these studies (i.e. $n = 3$ and $n = 4$), see Scheme 2. The first of the two linkers was synthesised in two stages, see Scheme 2. Firstly a reaction with propargyl bromide was carried out, adapted from a method reported by Goswami *et al.* [181], see Scheme 2. The sodium hydride must be added slowly as it rapidly releases hydrogen, which can cause an increase in pressure in the reaction vessel. The slow addition of propargyl bromide, rapid stirring, low temperature and dilute reaction mixture, promote mono substitution. However, despite these measures, some dialkylated PEGs were produced but these were removed along with other impurities by silica gel column chromatography.



Scheme 2: Synthesis of CC-PEG_n-COOH linkers, $n = 1-4$

The carbon-carbon triple bond is quickly and easily identified by TLC, using potassium permanganate staining. This allows monitoring of the reaction progress, following the consumption of the reagents. However, although all of the starting material was consumed, the highest isolated yield achieved was 40%. The characteristic triple bond C-H peak was present in the proton NMR spectrum at 2.4 ppm.

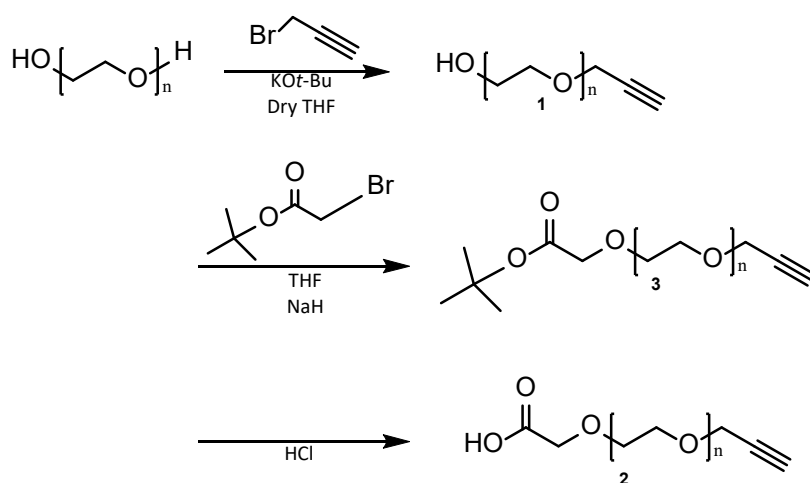
The method for the second stage of the reaction, with bromoacetic acid, was adapted from a method reported by Bogdan *et al.* [182], see Scheme 2. Analysis of the product by proton NMR showed the expected total number of protons on integration (two more than the starting material).

The main impurity observed was acetic acid, the majority of which was removed by drying *in vacuo* on a Schlenk line. However, some product loss was also observed, as the product appeared to be volatile, particularly for the shorter PEG chains. In some cases, this made it challenging to remove all of the DMF solvent without loss of product, and so a balance was sought to remove the acetic acid (as this would also couple to the CPC4 precursor) but it was not problematic if some DMF remained.

Some other impurities could be removed through washes and extractions, but silica column chromatography was required to achieve high purity.

2.2.1.2 Alternative synthesis method

Despite efforts to optimise drying and purification, it was clear from analysis by NMR that an alternative method of synthesis was needed, due to the quantity of acetic acid present in the final product. The method shown in Scheme 3 was used involving no direct acid addition, which proved to be easier to purify.



Scheme 3: Synthesis of CC-PEG_n-COOH linker, avoiding acetic acid impurities, n = 1-4

The polyethylene glycol was added to a suspension of KO t -Bu in dry THF at 0°C, under a nitrogen atmosphere, and allowed to stir for 20 minutes before leaving to warm to RT. Propargyl bromide was then added dropwise and the reaction mixture was stirred at 80°C for 18 hours.

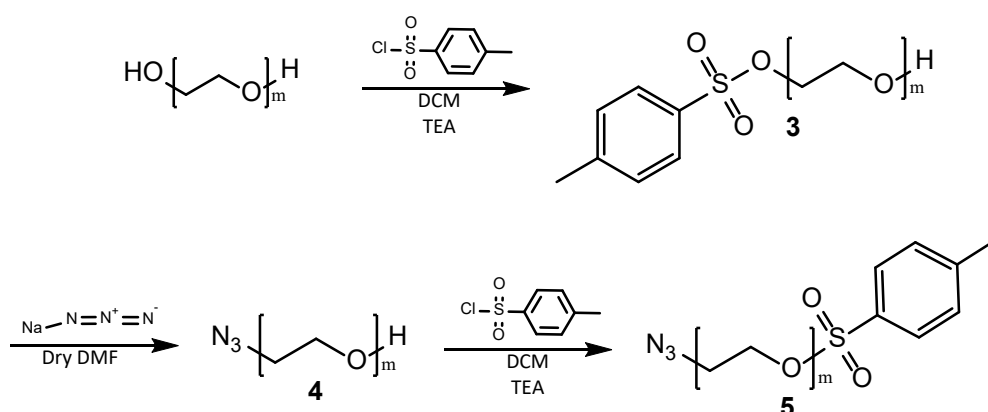
At the end of reaction, solvent was removed by evaporation and residue was recovered in DCM and water. The aqueous phase was extracted with 100 mL of DCM and the organic extracts washed with 150 mL of brine solution, dried over MgSO₄ and evaporated to dryness. Products were purified by silica gel column chromatography, with a gradient of 100% DCM to 2-3% MeOH in DCM.

NaH was added to the solution of CC-PEG_(n)-OH in THF at 0°C. The mixture was allowed to warm to room temperature for 30 min, allowing for the evolution of hydrogen, before being cooled back to 0°C prior to addition of tert-butyl 2-bromoacetate. After 30 min stirring at 0°C, the mixture was quenched with a saturated solution of NH₄Cl, phases separated, the aqueous phase was extracted with ethyl acetate and the combined organic layers washed with brine, dried over anhydrous Na₂SO₄, filtered and concentrated by rotary evaporation. The crude residue was purified by column chromatography to give CC-PEG_(n)-COOtBu as a colourless oil.

The t Bu ester was deprotected by treatment with an excess of HCl at room temperature overnight. Solvent was removed by rotary evaporation and the residue dried under Schlenk line to remove any trace solvent or HCl.

This synthesis method gave the desired product in higher levels of purity.

2.2.2 N₃-PEG_m-Tosyl synthesis



Scheme 4: Synthesis of N₃-PEG_m-Tosyl linker, m = 2-4 [183, 184]

Toluene sulfonyl (tosyl or tos) forms a good leaving group and is appropriate for the reaction to introduce the azide. Synthesis of this linker should be carried out in a dry, oxygen free environment. In step 1, TEA was added dropwise, at a low temperature. As with the TEA, the tosyl chloride should be added slowly to avoid bis-substitution. The method used was to suspend the powder in further DCM and to add slowly by syringe.

After washes with water, re-extractions if necessary, and a wash with 5% citric acid, very few impurities were seen and they were mainly made up of bi-substituted PEG chains and a small amount of other tosylate material, both of which could be easily removed with silica gel column chromatography.

Step 2 is a simple substitution reaction to replace the tosyl with an azide group. The reaction was carried out using sodium azide with heating overnight in DMF. Excess azide was used to drive the reaction, giving yields in excess of 90%. DMF was removed by rotary evaporation and could be azeotroped with water to encourage evaporation. The resulting solid was dissolved in diethyl ether with sonication followed by filtration through celite and the diethyl ether evaporated to give the product as an oil.

Step 3 follows the same reaction as the first step, although with altered ratios as there is only one end of the chain available for reaction. Excess TEA and tosyl chloride were used to maximise the yield. Purification procedures were identical to step 1 and, again, gave yields above 90%.

To follow the tosylation reactions, TLC with UV to visualise is the easiest method. Bis-tosyl-PEG chains separate easily from mono-tosyl-PEG chains, allowing for a short silica gel column to be used for purification separating the product and impurities. Proton NMR showed doublet peaks at 7.36 and 7.79 (ArH, 2H), which disappeared when replaced by N_3 , being the most obvious identifying feature of the tosyl group.

Yields in step 1 were 70-75% across all length chains, with ca. 90% for subsequent steps. Further optimisation or more care taken, particularly when removing solvents, may increase these even further.

In the first step, some bis-substitution of the tosyl group was observed. This was reduced by sufficient dilution and ensuring that the tosyl chloride was added slowly to promote mono-substitution. The Tos-PEG-Tos impurities were collected alongside the desired compounds during column chromatography purification for potential use in later experiments.

2.3 CPCR4-PEG_n-CC synthesis

2.3.1 General Peptide Synthesis

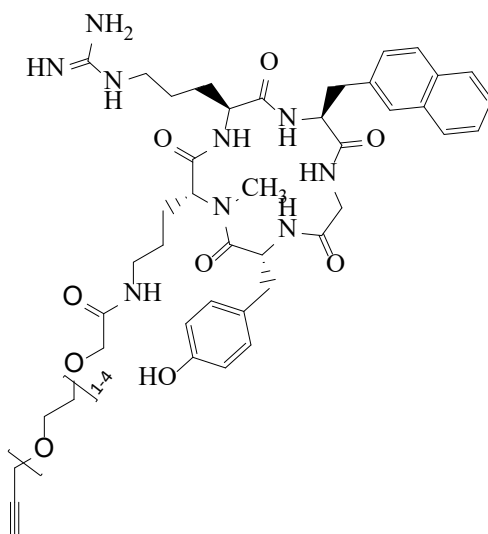


Figure 17: Structure of the target CXCR4 binding peptide in this work, CPCR4-PEG₁₋₄-CC

All peptides were synthesised on a 2-chlorotrityl resin, which was supplied preloaded with the first amino acid, glycine, already in place and protected by Fmoc. The addition of each amino acid required the removal of Fmoc from the previously added amino acid, as does the cyclisation stage. These steps are not shown in the schemes to prevent unnecessary repetition.

Amino acid coupling reactions were carried out in DMF (1 mL/250 mg of resin) using 4 equivalents of the amino acid, activated by 2-(1*H*-benzotriazol-1-yl)-1,1,3,3-tetramethyluronium hexafluorophosphate, (Hexafluorophosphate Benzotriazole Tetramethyl Uronium, HBTU) and diisopropylethylamine (DIPEA), see Figure 18. Secondary amino acids require the use of 1-[Bis(dimethylamino)methylene]-1*H*-1,2,3-triazolo[4,5-*b*]pyridinium 3-oxide hexafluorophosphate, (Hexafluorophosphate Azabenzotriazole Tetramethyl Uronium, HATU) in the place of HBTU and 6 equivalents of DIPEA. HATU can be used for all amino acids if necessary. Higher yields were sometimes found with HATU use, though this may have been due to other factors in the synthesis.

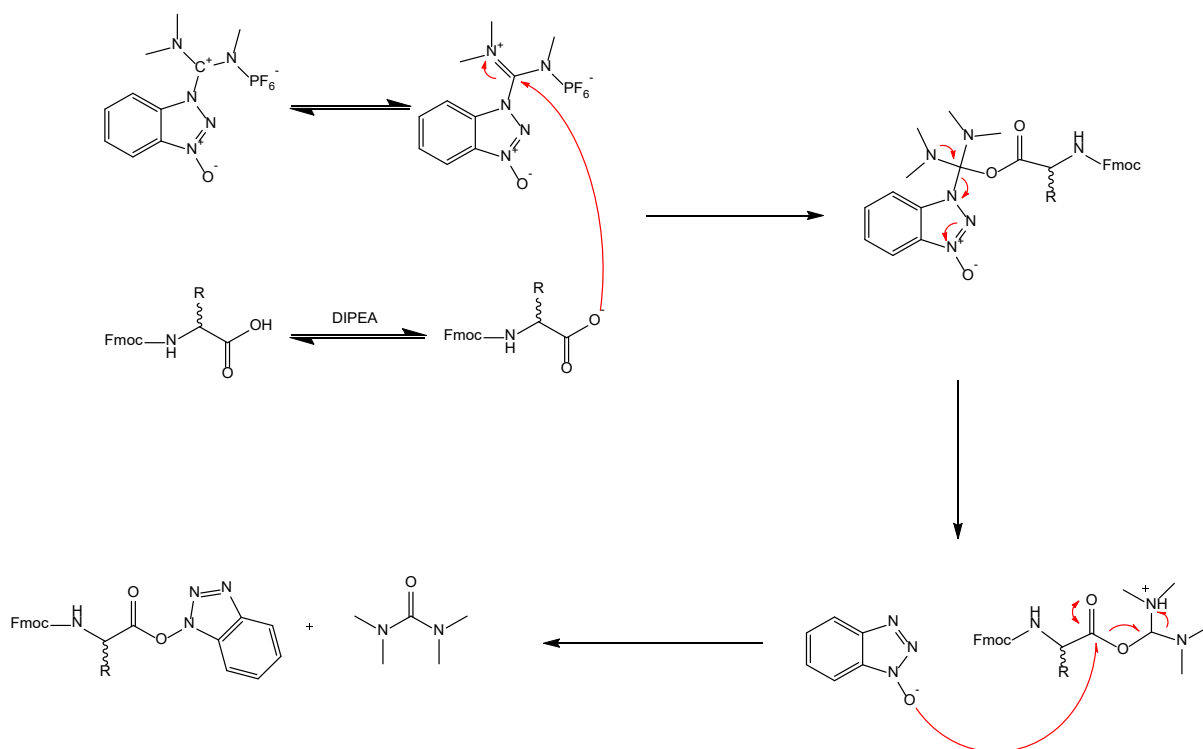


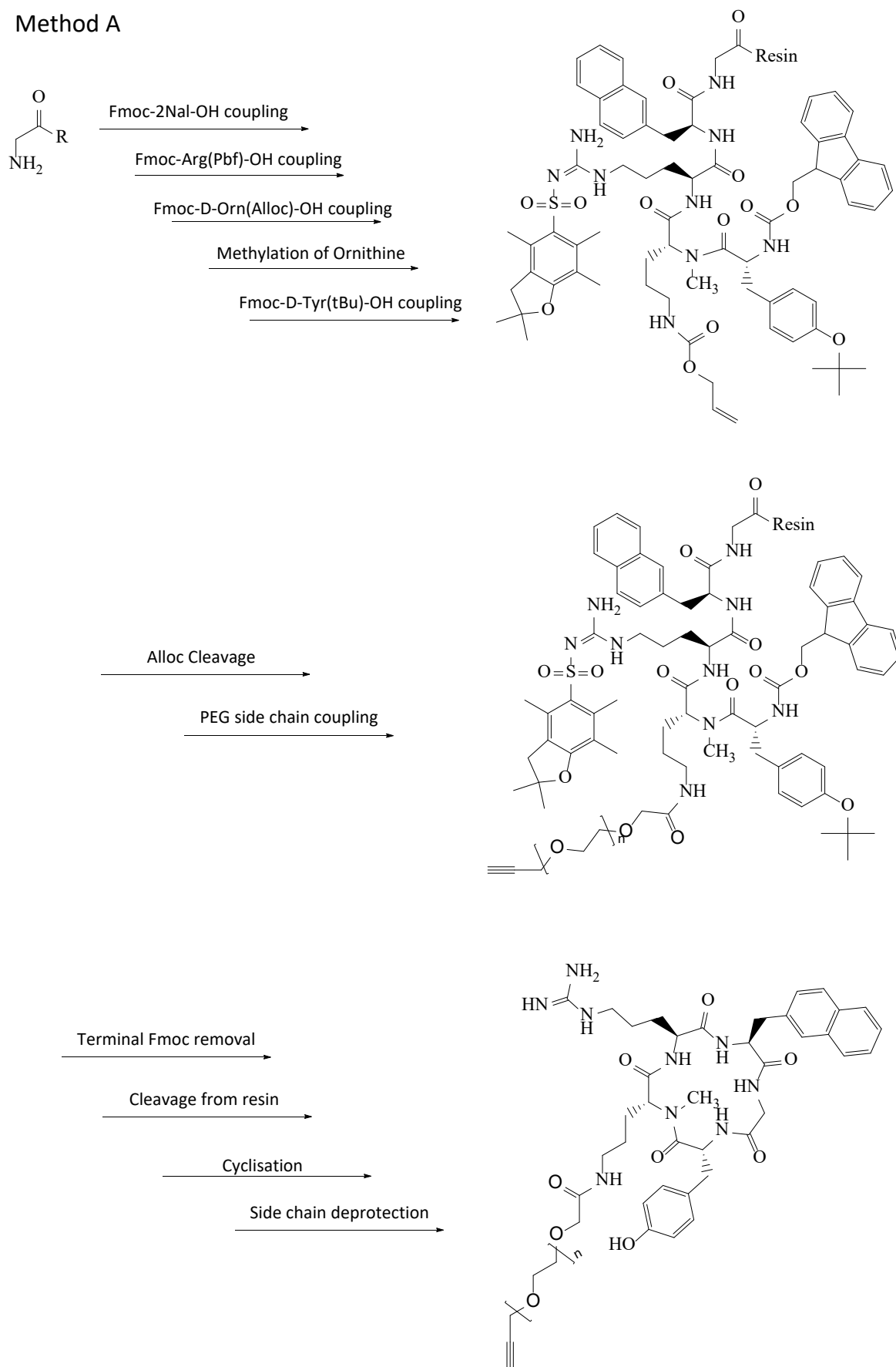
Figure 18: Amino acid activation by HBTU

Method A, see Scheme 5, shows ornithine side chains with Alloc protection while Method B, see Scheme 6, shows the side chain protected by Dde. Differences between these protection groups are discussed in section 2.3.2.

In order to monitor the addition of each amino acid, the Kaiser/Ninhydrin test was used, as it is a sensitive test for primary amines, requiring only a few beads of resin to produce clear results. The ninhydrin reacts with the amine to produce a clear dark blue colour, with a partially complete coupling producing a lighter blue colour. A complete coupling will produce little to no colour change [185]. False positives are possible if the test is not carried out correctly, due to Fmoc not being fully stable under some of the Kaiser test conditions.

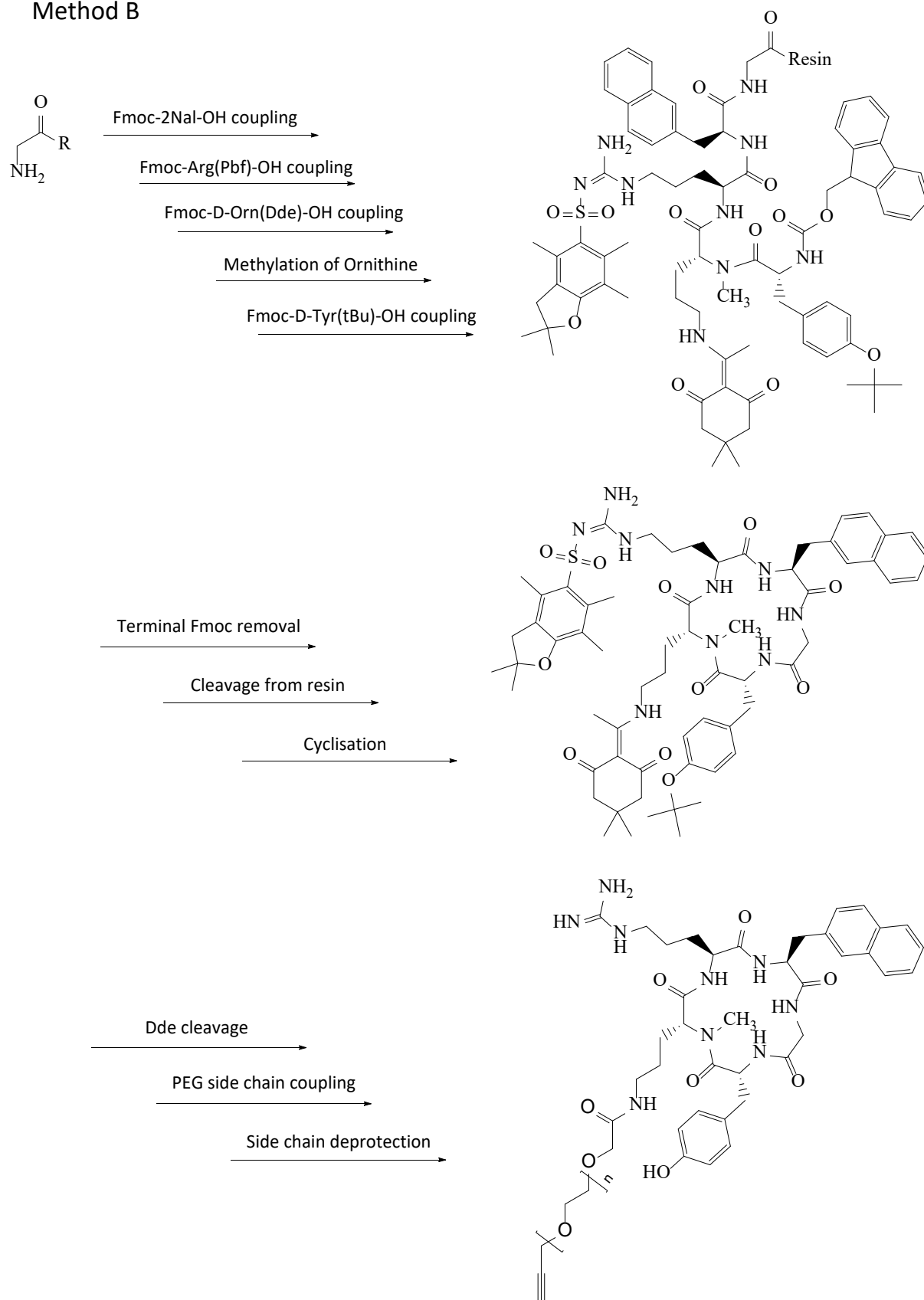
Other tests are possible, such as the bromophenol blue test and the 2,4,6-trinitrobenzenesulfonic acid test, which will also detect secondary amines, such as *n*-methyl amino acids, but the Kaiser test is the most commonly used.

Method A



Scheme 5: Synthetic route for CPCr4-PEG_n-CC, using alloc protected ornithine

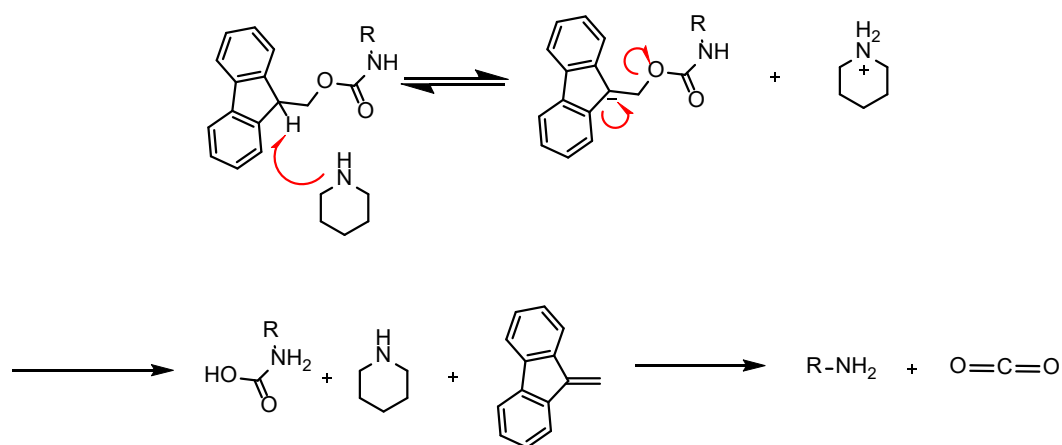
Method B



Scheme 6: Synthetic route for CPCr4-PEG_n-CC, using Dde protected ornithine (up to the formation of the linear peptide there is no difference between the methods, other than the protection groups shown).

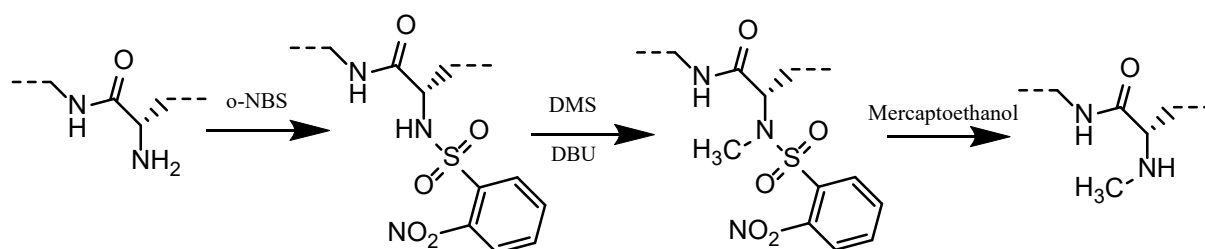
2.3.2 Side chain protection and protection removal

Fmoc is removed by two treatments with 50% piperidine in DMF solution.



Scheme 7: Fmoc protection group removal by piperidine treatment

N-Methylation was carried out in three stages, in N-methyl-2-pyrrolidone (NMP) as solvent. o-NBS protection is added to the resin as a solution of o-NBS and collidine. Three treatments of 1,8-diazabicyclo[5,4,0]undec-7-ene and dimethyl sulphate result in the methylation and the o-NBS is then removed by three treatments with mercaptoethanol.



Scheme 8: Terminal amine N-methylation

Three side chains within the peptide require protection during synthesis. Arginine is protected by Pbf (2,2,4,6,7-pentamethyldihydrobenzofuran-5-sulfonyl) and tyrosine by *t*Bu (*tert*-butyl). Both can be removed once the peptide construction is complete and are stable under all of the reaction conditions encountered.

However, ornithine's side chain requires removal selectively to allow the addition of the PEG chain linker. Initially, this was done with an allyloxycarbonyl (Alloc) protection group, selectively cleaved by PhSiH_3 and $\text{Pd}(\text{Ph}_3\text{P})_4$ catalyst. Some papers report Fmoc to be stable in these conditions, but this was

found to not always be the case, with some other researchers reporting similar issues [186, 187]. It is for this reason that Dde was used as a protecting group instead, which eliminated the issue.

Dde can be cleaved in a range of different ways, either with hydrazine, or with a mixture of hydroxylamine hydrochloride and imidazole [188]. Hydrazine removes the Dde in minutes but also cleaves Fmoc and so is not a suitable reagent. Unfortunately, whilst Fmoc is stable in the hydroxylamine hydrochloride, imidazole mixture, the removal of Dde is also an overnight reaction, extending the synthesis time of the peptide. Hydrazine can be used to remove Dde in the peptide liquid phase after cyclisation, as Fmoc is no longer present.

In this synthetic protocol, the Dde group was used to protect ornithine. Following synthesis of the protected, linear peptide on resin, the Fmoc group of the N-terminus was removed, followed by peptide cleavage from the resin. The peptide was then “cyclised” in solution. The Dde group could then be simply removed. Following this, the PEG linker was attached in a “click” reaction, prior to removal of other peptide protecting groups.

2.3.3 Order of reaction steps – when to couple the PEG chain

When to couple the PEG to the peptide is an important part of the order of the reaction steps. As mentioned, it can be done at different times, with the peptide in linear form prior to cleavage, or cyclic form in the liquid phase. Coupling in solid phase is simpler and allows for easier purification. However, cleavage of Dde in liquid phase with the cyclic peptide can be done in a few minutes using 2% hydrazine, instead of overnight as required for the solid phase. Hydrazine cleaves Fmoc as well as Dde, so is not suitable for use with the peptide linear form.

Another factor for consideration is the cost of the reagents being used, Dde protected ornithine being more expensive than alloc protected, hence the original plan to use alloc protected ornithine to synthesise CPC4.

2.3.4 Purity and by-product analysis

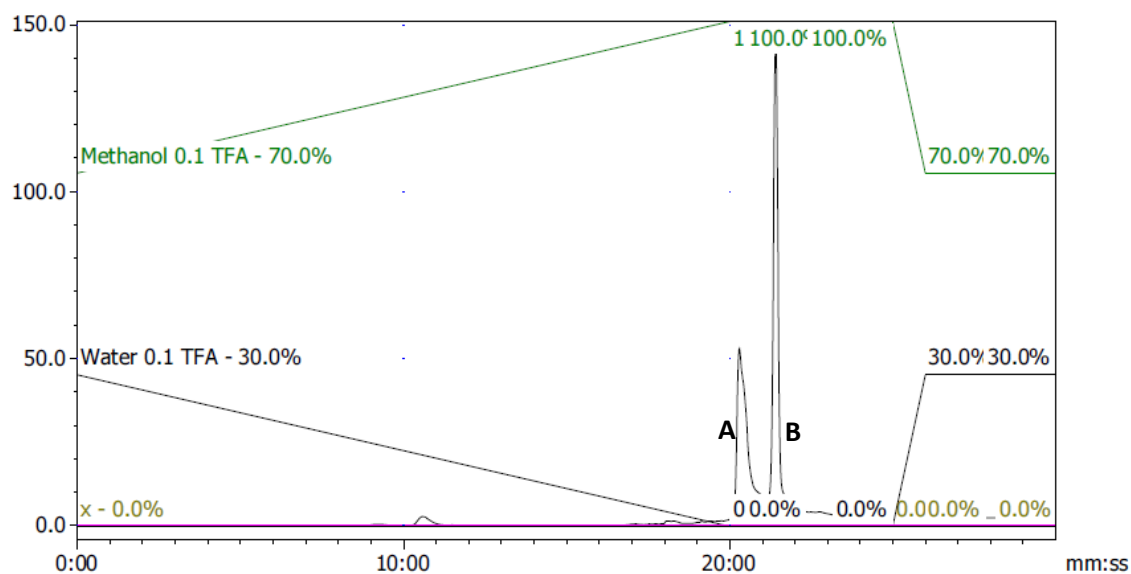


Figure 19: HPLC chromatogram of linear, protected version of CPCr4, pre-PEG chain coupling.

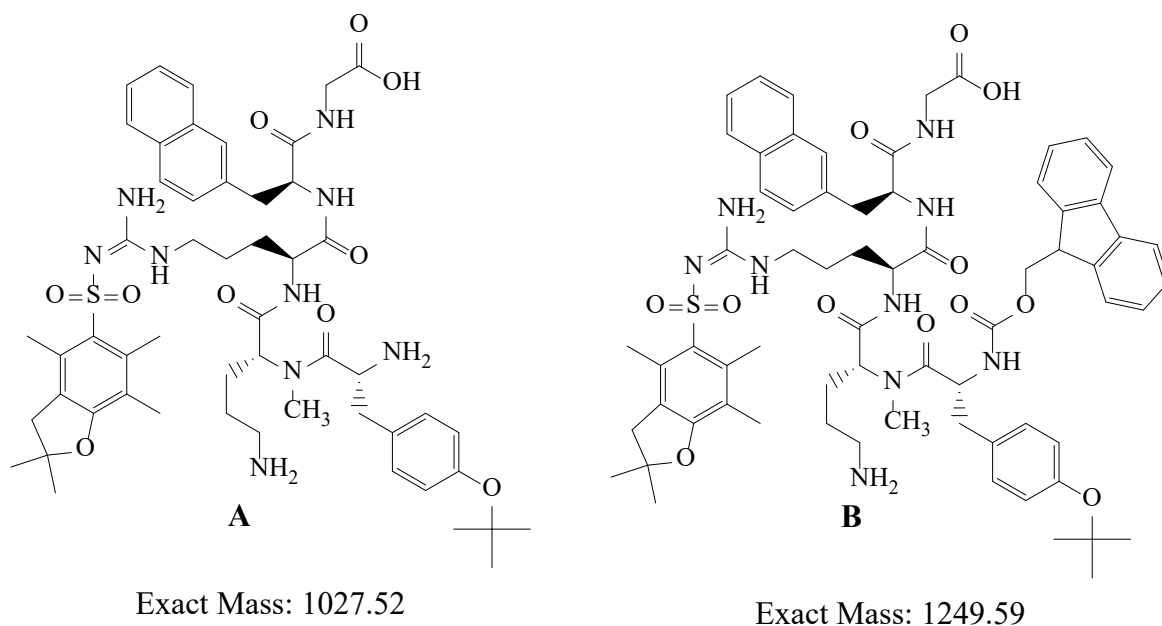


Figure 20: Pre-PEG chain coupling, linear peptide structures identified by HPLC and MS, with and without Fmoc terminal protection

Analysis by HPLC before the coupling of the PEG chain, see Figure 19, revealed two peaks with different masses, 1028 (Peak A) and the desired 1250 (Peak B), which is the linear peptide, before the PEG chain is coupled and after alloc side chain protection has been cleaved, see Figure 20.

Having both potential attachment points available for the PEG to react with would lead to the 3 possible outcomes, as shown in Figure 21. Two of these have the same mass but would cyclise in different ways, and so it would be challenging to separate them using semi-preparative HPLC and MS identification. The third potential product has a higher mass, with two PEG chains attached, and so would not cyclise. Both masses were observed from the reaction.

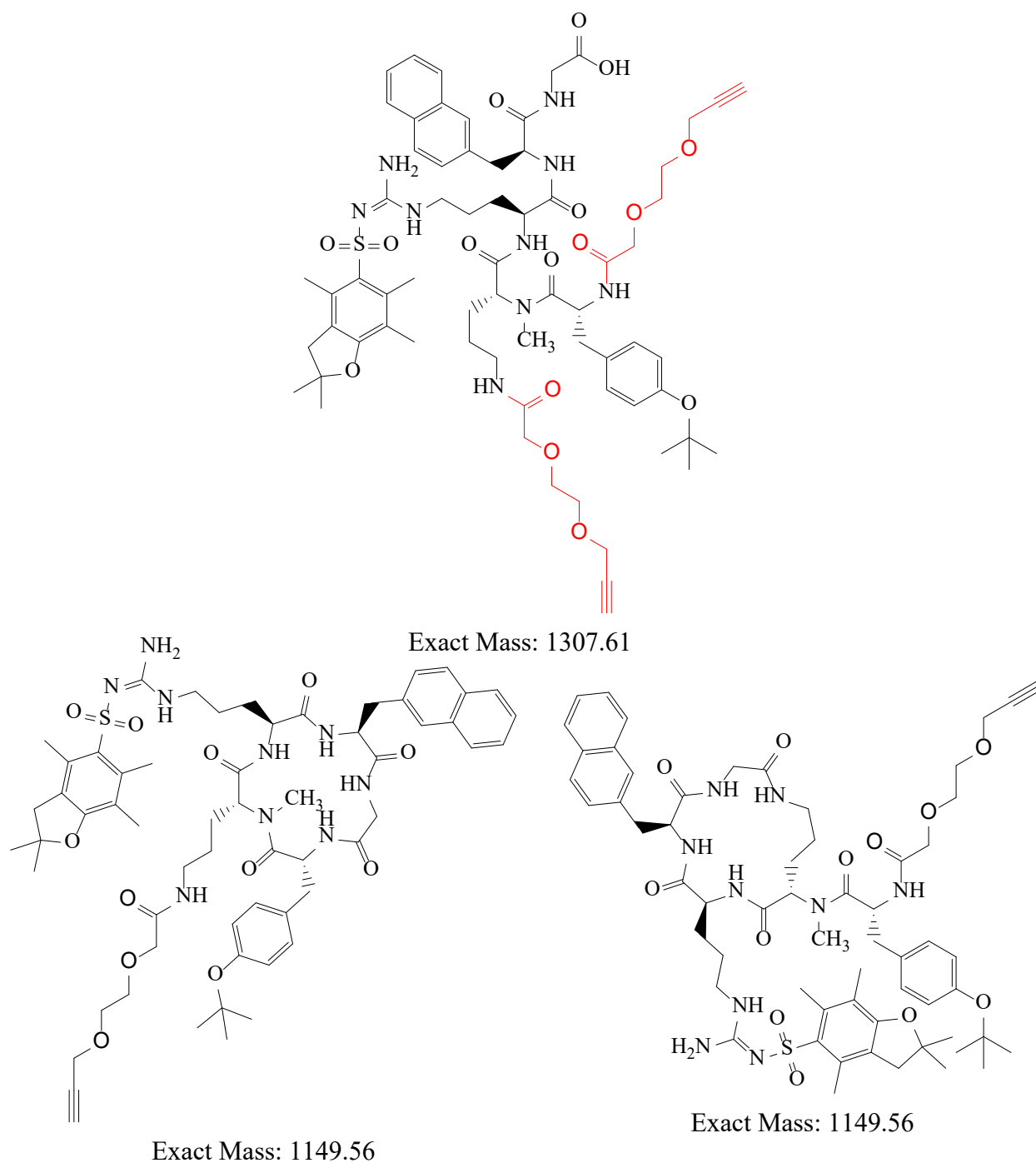


Figure 21: Potential outcomes following the coupling of CC-PEG₁-COOH and cyclisation of peptide without Fmoc protection, with correct cyclic product on the left, incorrect tetrapeptide on the right and incorrect bi-PEG linear peptide above.

The unwanted by-products were due to the alloc cleavage technique prematurely removing the Fmoc protection of the terminal amino acid. Literature reports indicate that this has been seen before, although it is normally assumed that Fmoc is stable under these conditions, so an alternate side chain

protection was used, with Dde being chosen. Shorter reaction times may have partially addressed this issue; however, the decision was made to switch to an alternate protecting group instead.

The other main issue during peptide synthesis appeared to be instability with early incorporation of the alkynyl group, either reducing yields or causing problems with the subsequent “click” reaction.

There was potential for reaction between the alkynyl group on the peptide and the N_3 of the cyclisation reagent, diphenylphosphoryl azide (DPPA), causing side reactions and consuming the reagent. Without the presence of a catalyst, this reaction should be disfavoured but was considered as a possibility. Further investigation would be required to determine if this was occurring.

The synthesis of the stable fluorine isotope standards did not have these issues as a different method was used which is not compatible with radiolabelling.

2.4 Stable fluorine isotope standards

2.4.1 Synthesis method

The stable fluorine isotope analogue of the tracer, to be used for *in vitro* biological testing, was made using a different method to the radioactive isotope analogue. The full linker, including the fluorine, was “click” reacted before being attached to the ornithine residue of the linear peptide using the standard coupling method. The remaining steps were then completed as previously, with cleavage from the resin and cyclisation.

By “click” reacting the two linker components together before attaching them to the peptide, there was no longer an issue with the presence of a propargyl group (see Section 2.3.4). However, this method requires overnight reaction times to go to completion, hence is not possible for the radiotracer.

2.4.2 Reagent solution quantities for PEG coupling

Following the synthesis of the linear CPC4 structure, prior to the coupling of the PEG chain, the resin was weighed and divided into six, roughly equal aliquots, with the masses given below. HATU quantities were corrected for resin mass.

Table 4: Corrected quantities for PEG chain coupling reactions

| PEG chain to be coupled | Resin mass aliquoted, mg | HATU, corrected for resin mass, mg |
|--|---------------------------------|---|
| COOH-PEG ₂ -PEG ₃ -F | 545.8 | 49.5 |
| COOH-PEG ₂ -PEG ₄ -F | 609.1 | 42.2 |
| COOH-PEG ₃ -PEG ₃ -F | 609.1 | 39.3 |
| COOH-PEG ₃ -PEG ₄ -F | 672.5 | 48.9 |
| COOH-PEG ₄ -PEG ₃ -F | 672.5 | 45.7 |
| COOH-PEG ₄ -PEG ₄ -F | 735.8 | 50.5 |

Individual peptides were cleaved from the resin and cyclised in DMF, with DPPA and NaHCO₃. The mass amount isolated contains some accompanying salt impurities and so yields were not calculated at this stage.

Table 5: HPLC retention times and purities of stable fluorine isotope analogues of the tracer. HPLC gradient: MeOH 0.1% TFA in water 0.1% TFA, 5 to 95%, 20 min, 1.0 mL/min.

| Compound | Retention time | Purity, % |
|--|-----------------------|------------------|
| COOH-PEG ₂ -PEG ₃ -F | 15 min 46 s | >95 |
| COOH-PEG ₂ -PEG ₄ -F | 15 min 49 s | >95 |
| COOH-PEG ₃ -PEG ₃ -F | 15 min 51 s | >98 |
| COOH-PEG ₃ -PEG ₄ -F | 15 min 55 s | >94 |
| COOH-PEG ₄ -PEG ₃ -F | 15 min 58 s | >94 |
| COOH-PEG ₄ -PEG ₄ -F | 16 min 01 s | >93 |

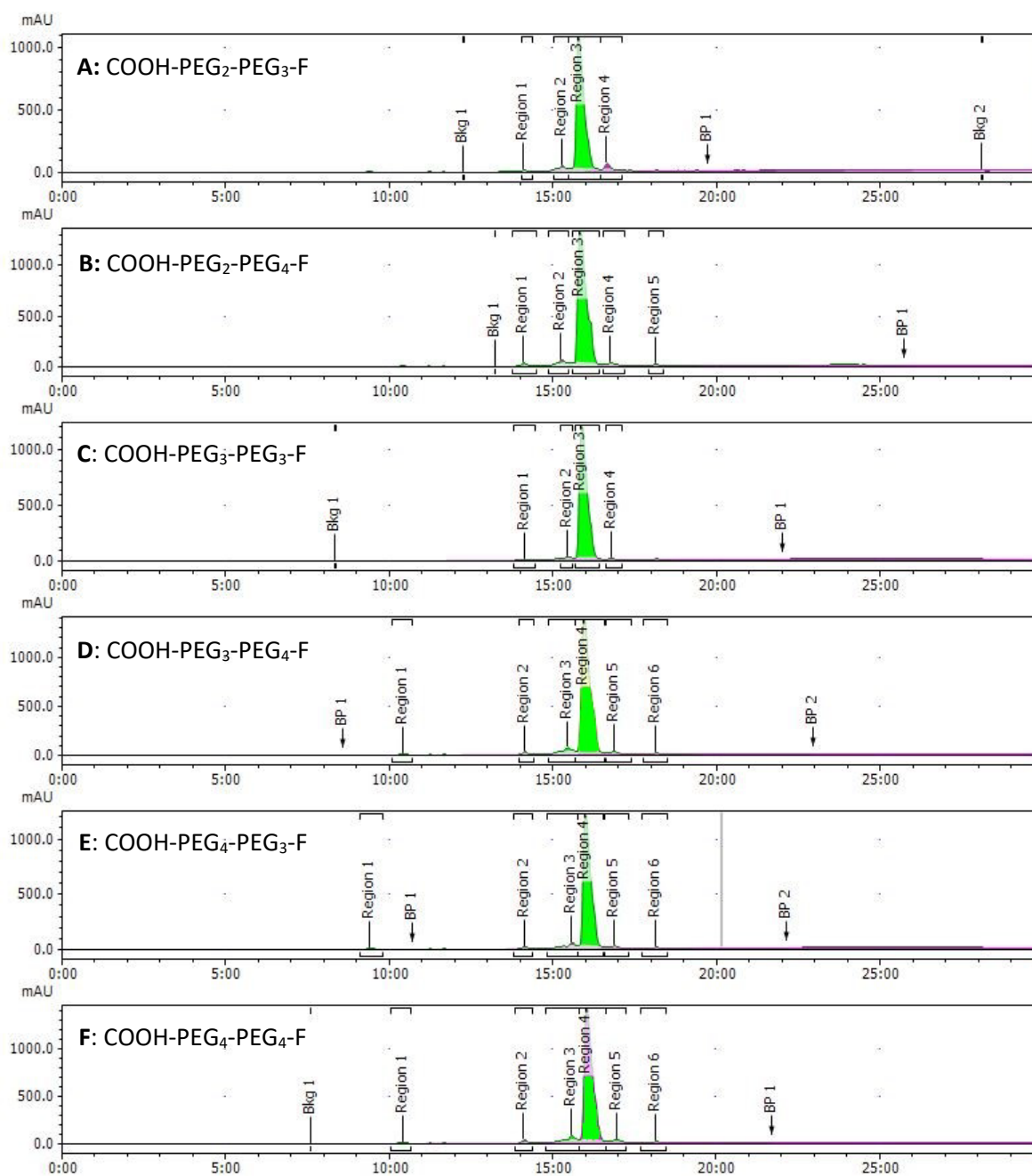


Figure 22: HPLC chromatograms of stable fluorine isotope analogues of the tracer. HPLC gradient: MeOH 0.1% TFA in water 0.1% TFA, 5 to 95%, 20 min, 1.0 mL/min. A: COOH-PEG₂-PEG₃-F, B: COOH-PEG₂-PEG₄-F, C: COOH-PEG₃-PEG₃-F, D: COOH-PEG₃-PEG₄-F, E: COOH-PEG₄-PEG₃-F, F: COOH-PEG₄-PEG₄-F

2.5 Biological studies: *in vitro*

2.5.1 Cell receptor binding assays

The use of cell receptor binding assays, in particular competition binding assays and other related measures of target receptor binding properties are well characterised techniques for establishing the interaction between the molecular compound and the target chemokine receptors. These *in vitro* studies can give information on the nature of the interaction (antagonist vs. agonist) and the relative affinity of the molecular compound studied for the target receptor. Often several different types of assays are used to investigate compounds for their targeting of a single receptor to give broader characterisation and increased data on the nature of the molecular interactions. Commonly used assays for GPCR binding, and chemokine receptor interactions in particular, include fluorescence or luminescence-based assays detecting fluctuations in the level of one or more secondary messengers, such as Ca^{2+} or cyclic adenosine monophosphate (AMP), β -arrestin recruitment assays and phenotypic screening assays [189].

The choice of assay used will be affected by the desired information and previous studies in the area. This can include factors such as cost and availability, or more complex issues such as autofluorescence of the compound under investigation, which could interfere with the readout of the assay [189].

Calcium signalling, utilising a Fluorometric Imaging Plate Reader (FLIPR) system was developed by Prof. Schols (KU Leuven) and his research team to detect and quantify the intracellular calcium flux released upon activation of CXCR4 by CXCL12. The binding of CXCL12 to CXCR4 triggers this calcium flux, which can be detected by prior addition of a calcium sensitive fluorescent dye (Fluo-3) to the cells that is activated on binding to calcium and allows quantitative detection with the FLIPR system [190]. The FLIPR system's ability to monitor intracellular Ca^{2+} mobilisation allows for quantitative evaluation of chemokine receptor antagonists with a high throughput, making it useful for the screening of a variety of drug or tracer responses [189, 190]. Whilst the concentration of CXCL12 is kept constant, increasing amounts of an inhibitor are added. The concentration at which the signal reduction is reduced by 50% relative to the maximum is the 50% inhibitory concentration (IC_{50}) and provides a useful number for comparison of a range of antagonist molecules. A low IC_{50} value is desirable, to give efficient accumulation and retention at the target receptor, potentially improving the quality of the image data. The calcium signalling assay with CXCL12 is not useful for assessment of agonist molecules. In this case, only antagonists were assessed. This is confirmed by the lack of calcium release when the cells are solely exposed to the peptides with no CXCL12 present.

The FLIPR system for calcium signalling provides an excellent readout of affinity but it does require some optimisation of conditions and so our research group did not attempt to set this assay up in Hull but rather relied on the collaboration with the Schol's group at KU Leuven. Other assays such as the antibody competition assay using flow cytometry have been performed routinely in Hull. In this case a fluorescent tagged antibody is used to displace the bound antagonist molecule. The other assay carried out by Schol's group to assess binding affinity was a competition assay with fluorescent tagged CXCL12 (alexafuor-CXCL12) to give a direct readout of competition for binding to CXCR4 which is also of interest alongside the calcium signalling assay results. This second assay also provides an IC_{50} value.

2.5.2 CXCL12 competition binding assay – Jurkat cells

Assays on the range of compounds produced were carried out by Prof. Dominique Schols and his research team at the Rega Institute (KU Leuven) [191].

The assay works due to the competition between a fixed amount of fluorescently labelled CXCL12, CXCL12^{AF647}, and the unlabelled test compound. As CXCL12 is the natural chemokine agonist for CXCR4, compounds that interfere with the binding of CXCL12^{AF647} should interact in the same way with the orthosteric site. The fluorescence can be detected by flow cytometry, allowing for a quantifiable analysis of the percentage of site blocked by the tested compound [191].

Table 6: Compounds and CXCR4 affinity, from competition binding assay measurements, (n = 2)^a
Compounds containing PEG₃ were from the same batch of linker and results may be inaccurate due to undetected impurities or samples diminished before testing.^b n = 1

| Name | Compound | IC ₅₀ , nM, Mean ± SD |
|----------|---|----------------------------------|
| SJA-1023 | CPCR4-PEG ₂ -PEG ₃ -F | 198.95 ± 4.75 |
| SJA-1024 | CPCR4-PEG ₂ -PEG ₄ -F | 215.25 ± 16.45 |
| SJA-1025 | CPCR4-PEG ₃ -PEG ₃ -F | 550.6 ± 19.4 ^a |
| SJA-1026 | CPCR4-PEG ₃ -PEG ₄ -F | 4563 ^{ab} |
| SJA-1027 | CPCR4-PEG ₄ -PEG ₃ -F | 281.9 ± 32.7 ^a |
| SJA-1028 | CPCR4-PEG ₄ -PEG ₄ -F | 199 ± 48.6 |
| | AMD3100 | 15.33 ± 1.69 |
| | AMD11070 | 2.23 ± 0.13 |

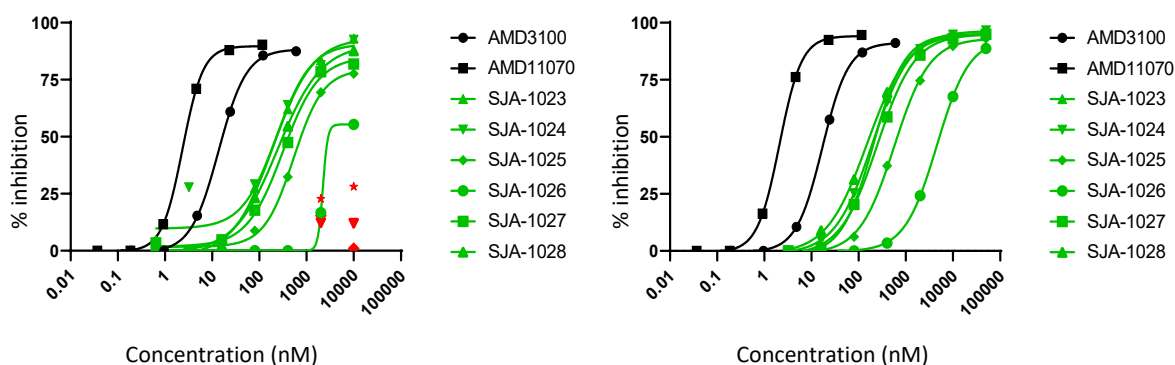


Figure 23: Competition binding assays, carried out by Prof. Schols and his research team at KU Leuven, Belgium. Graphs from repeat assay measurement (each performed in triplicate) to allow determination of a standard deviation.

This competition binding assay appeared to show very little difference in affinity between the screened tracers, with no clear pattern but several anomalous results, (in particular SJA-1026). The affinity (IC_{50} values) showed lower potency than expected but this is still in a range that would show *in vivo* binding to the CXCR4 receptor target and so it was appropriate to proceed to *in vivo* studies with some of these tracer candidates.

The exact reasons for the anomalous results are unclear (particularly when the peptide binding unit is unchanged) but one potential issue identified for future investigation is the presence of variable amounts of salt contamination from HPLC purification (presence of trifluoroacetic acid in the mobile phase). Resynthesis of the SJA1026 sample is required to repeat the analysis as there is no obvious explanation for the low affinity.

2.5.3 Calcium mobilisation assay – U87.CD4.CXCR4 cells [190]

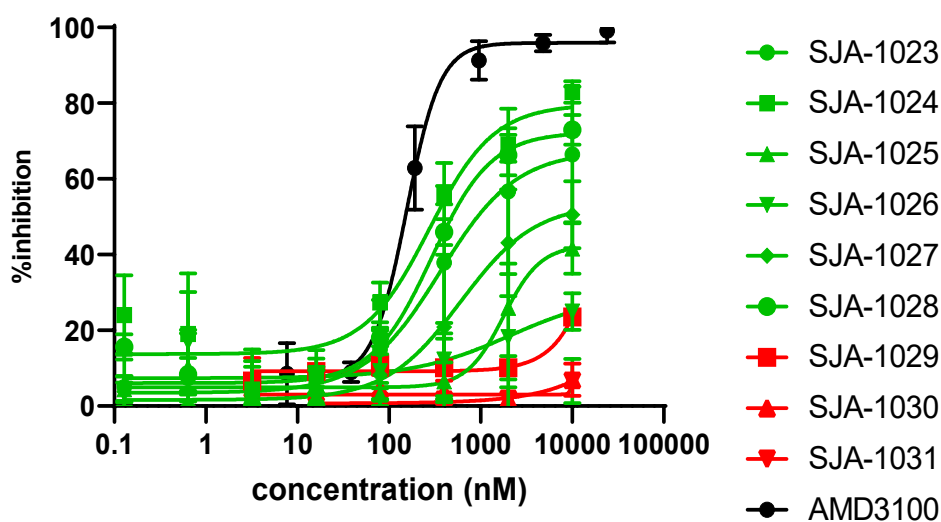


Figure 24: Calcium mobilisation assays, percentage inhibition, carried out by Prof. Schols and his research team in Belgium.

Table 7: Compounds and CXCR4 affinity, from calcium mobilisation assay measurements. ^a As with the previous binding assay, PEG₃ was from the same batch and results indicate there may have been an undetected impurity or samples diminished before testing.

| Name | Compound | CXCR4 affinity, IC ₅₀ (nM) |
|----------|---|---------------------------------------|
| SJA-1023 | CPCR4-PEG ₂ -PEG ₃ -F | 361.6 |
| SJA-1024 | CPCR4-PEG ₂ -PEG ₄ -F | 274.4 |
| SJA-1025 | CPCR4-PEG ₃ -PEG ₃ -F | >10000 ^a |
| SJA-1026 | CPCR4-PEG ₃ -PEG ₄ -F | >10000 ^a |
| SJA-1027 | CPCR4-PEG ₄ -PEG ₃ -F | ~10000 ^a |
| SJA-1028 | CPCR4-PEG ₄ -PEG ₄ -F | 292.4 |
| | AMD3100 | 155.2 |

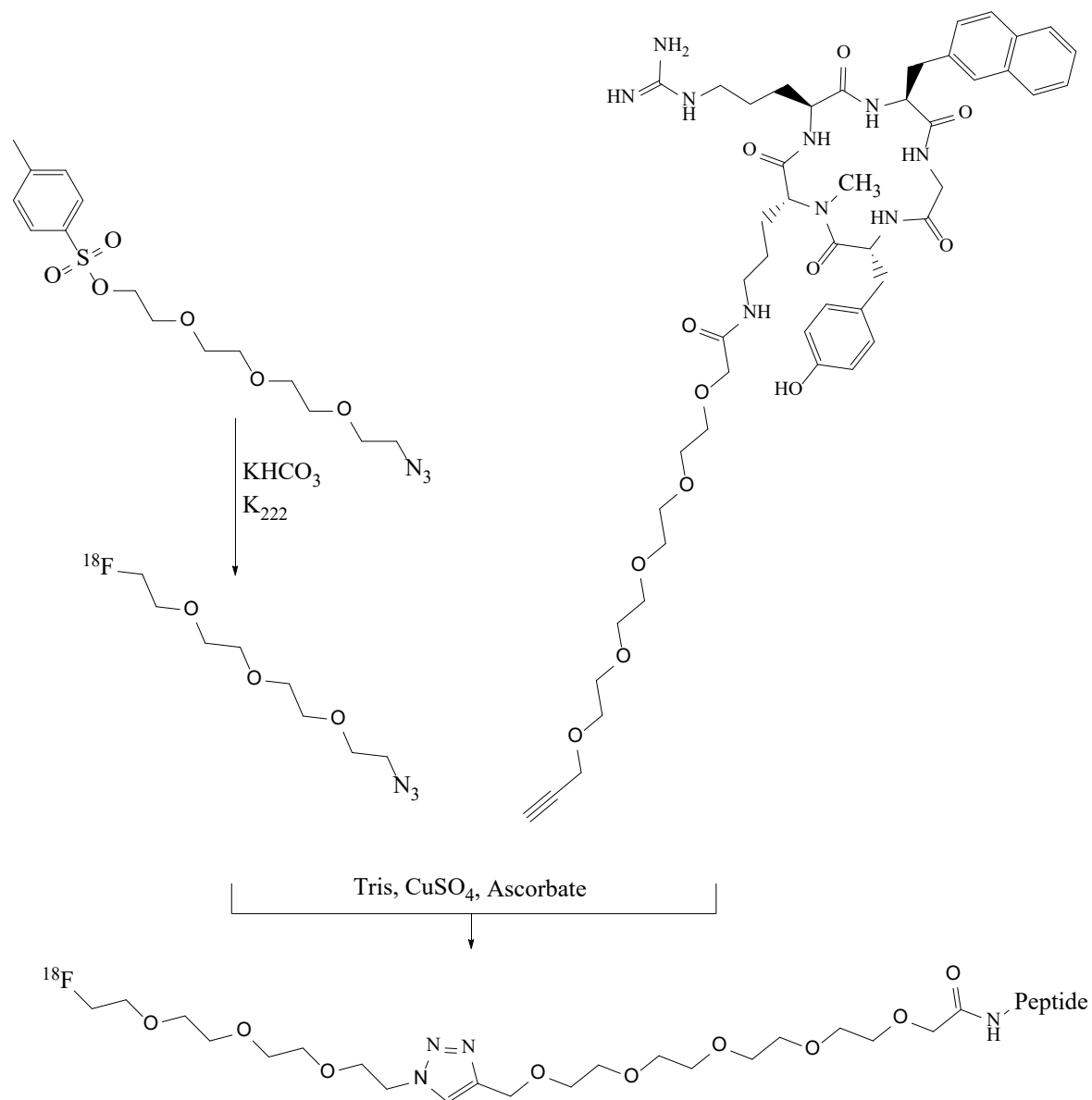
Consistent with the competition binding assay, the calcium mobilisation assay appears to show only small changes in affinity between each of the fluorinated peptide compounds that showed binding (SJA1023, SJA1024 and SJA1028). Three peptide compounds showed unexpectedly low binding that was inconsistent (SJA-1025, SJA-1026 and SJA-1027) likely indicating issues with these batches or the assay samples and so these assays need to be repeated on fresh samples to confirm results. However, a good level of consistency was observed between the two assays for SJA1023, SJA1024 and SJA1028 identifying these three compounds as the lead tracer candidates, (IC₅₀ = 361.6, 274.4 and 292.4 nM respectively, from the intracellular signalling calcium mobilisation assay).

Following the results of these two assays, and the effectiveness of synthetic protocols, it was decided SJA-1028, (CPCR4-PEG₄-PEG₄-F), would be the best option to take forward for fluorine-18 radiolabelling, further characterisation and imaging studies. This was based on the IC₅₀ of 199 ± 48.6

nM by competition binding assay and 292.4 nM by calcium mobilisation assay. These longer PEG chains showed higher stability during synthesis and were produced in higher yields relative to the other compounds produced.

2.6 Peptide radiolabelling with fluorine-18 for PET imaging

2.6.1 "Click" reaction for radiolabelling



Scheme 9: Radiotracer synthesis via "click" reaction.

The assembly of the ^{18}F -labelled tracer from the pre-prepared, azide functionalised prosthetic group, and alkyne functionalised peptide is shown in Scheme 9. A protocol was adopted that requires two semi-preparative radio-HPLC purification steps, initially purifying the prosthetic azide linker after ^{18}F -radiolabelling, with a second purification of the radiotracer following the "click" reaction. This purification should provide the desired radiotracer in high specific activity, removing any unlabelled linker and unlabelled/unreacted peptide precursor.

The tracer selected for radiosynthesis was [^{18}F]CPCR4-PEG₄-PEG₄-F, [^{18}F]SJA-1028. Fluorine-18 was eluted from the cyclotron and trapped on a pre-activated QMA-carb light or regular QMA light cartridge. This was then eluted directly into a reaction vessel containing Kryptofix in acetonitrile, before being dried under inert gas. The mean activity eluted was 1974 ± 382 MBq.

The PEG linker precursor, N₃-PEG₄-Tosyl, was radiolabelled by addition to the reaction vessel and heating to 105-110°C for 10 min, to allow substitution of the tosyl group. The reaction was allowed to cool to 80°C before unreacted [^{18}F]-fluoride was trapped on an Alumina N light cartridge and activity reconstituted in 20% MeOH: water solution for purification by semi-preparative HPLC. After being collected and diluted, the radiolabelled prosthetic group was passed through a homemade cartridge containing HLB C18 sorbent, washed with water and dried with inert gas before being eluted with THF into an HPLC vial.

RCY for the prosthetic, ([^{18}F]N₃-PEG₄-F), was $53 \pm 10\%$ (decay corrected), with the procedure taking 120 minutes (n = 5).

Once purified, this prosthetic was “clicked” to the peptide side of the tracer, CPCR4-PEG₄-CC, using the CuAAC reaction. The peptide, THF and copper salt solution were added to tris-[(1-benzyl-1H-1,2,3-triazol-4-yl)methyl]amine contained in an HPLC champagne vial and the mixture de-oxygenated by bubbling through argon gas. Under a blanket of argon, the radioactive prosthetic was added, followed by sodium ascorbate solution and reaction heated at 50°C in closed vessel for 15 min. The mixture was then diluted with water and purified by semi-preparative HPLC.

Radiolabelling yield from the CuAAC reactions was $62 \pm 10\%$ (decay corrected), taking an average 61 minutes (n = 4).

After collection and dilution, the radiolabelled tracer was again passed through a homemade cartridge containing HLB C18 sorbent, washed with water and dried with inert gas before being eluted with ethanol/acid. The solvent was reduced to near dryness under a gentle stream of inert gas and heating at 80°C then reconstituted in PBS solution. If needed, the pH was adjusted to 7.5 with sodium carbonate solution, the formulated radiotracer was filtered through a 0.22 μm filter for sterility and delivered for *in vivo* imaging.

The final formulated tracer yield was $37 \pm 15\%$ (decay corrected), delivering 103 ± 53 MBq (n = 5).

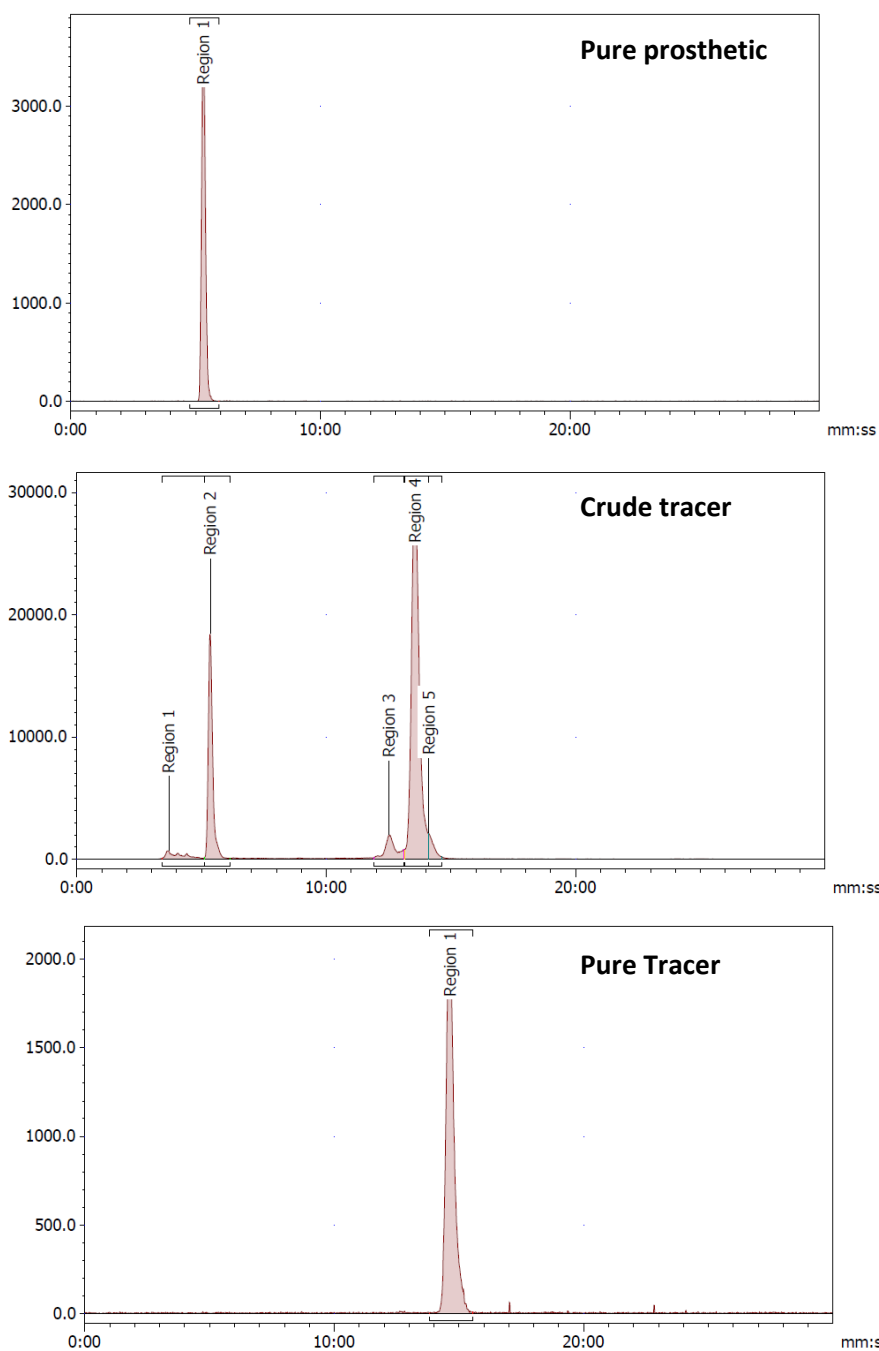


Figure 25: Example radio HPLC chromatograms of a purified [^{18}F]N $_3$ -PEG $_4$ -F prosthetic, crude tracer post-“click” reaction and the purified radiotracer

2.6.2 LogD comparison

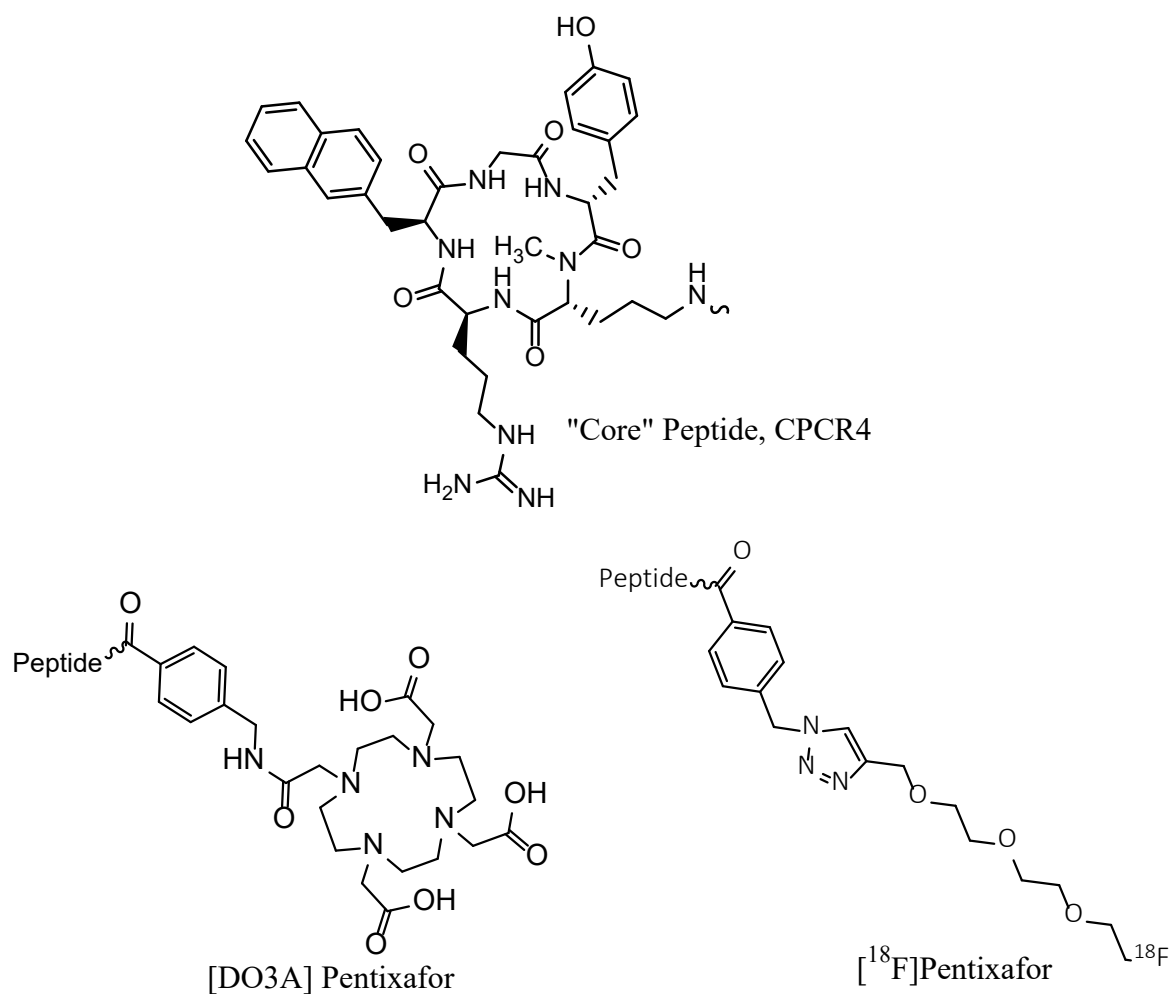


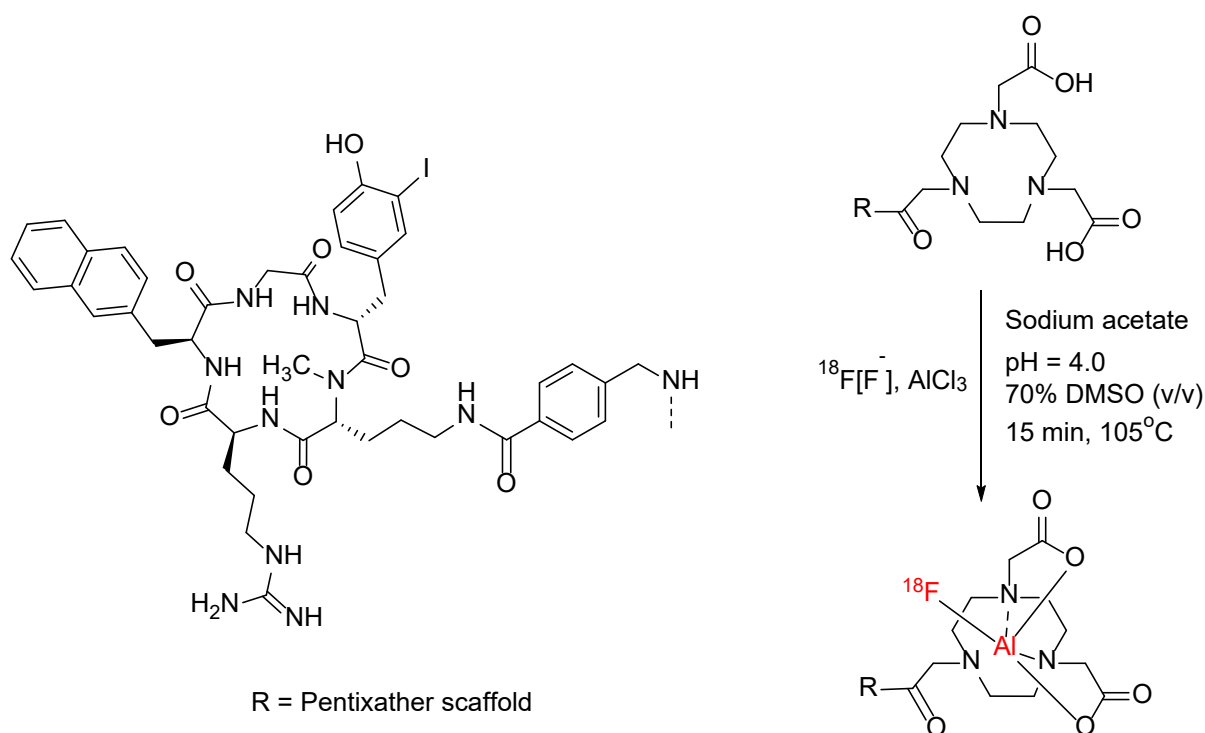
Figure 26: Structures of core peptide and respective chelators / ¹⁸F-labelled moieties

Table 8: Lipophilicity comparison, from LogD_{7.4} or LogP, as required

| Compound | Lipophilicity, Mean ± SD |
|---|---|
| [¹⁸ F]CPCr4-PEG ₄ -PEG ₄ -F | LogD _{7.4} = - 1.13 ± 0.01 (n = 3) |
| [¹⁸ F]Pentixafor | LogD _{7.4} = - 0.14 ± 0.01 [80] |
| [⁶⁸ Ga]Pentixafor (DO3A) | LogP = - 2.90 ± 0.08 [152] |
| [¹⁸ F]AlF-NOTA-pentixather | LogP = -1.4 [163] |

One of the issues for tracer characteristics, and the main aim of this section of development, was the lipophilicity of the ^{18}F -derivatives of this tracer causing it to be excreted *via* the biliary system, causing sub-optimal imaging properties. With the tracer accumulating in the liver and gut, tumours may be difficult to locate and clearance is slowed, with significant amounts of non-specific uptake, as can be seen in Figure 27 [80]. It should be noted that Pentixafor does not bind to murine CXCR4 (very low affinity) and so binding to murine CXCR4 is not observed *in vivo* [113].

The increased hydrophilicity caused by the longer PEG chains is therefore a significant step in the right direction. Poschenrieder *et al.* achieved similar properties using an [^{18}F]AlF-labelled 1,4,7-triazacyclononane-triacetic acid (NOTA) analog of pentixather, although their tracer showed increased accumulation in the intestines and gall bladder [163]. This is an issue with aluminium-fluoride, where an increase in lipophilicity is observed relative to the gallium-68 labelled tracer analogue. Hence, further investigation of PEG linked derivatives and the use of “click” radiolabelling with fluorine-18 prosthetic groups is justified.



Scheme 10: Aqueous radio fluorination of NOTA-pentixather. Reproduced from Poschenrieder *et al.* [162]

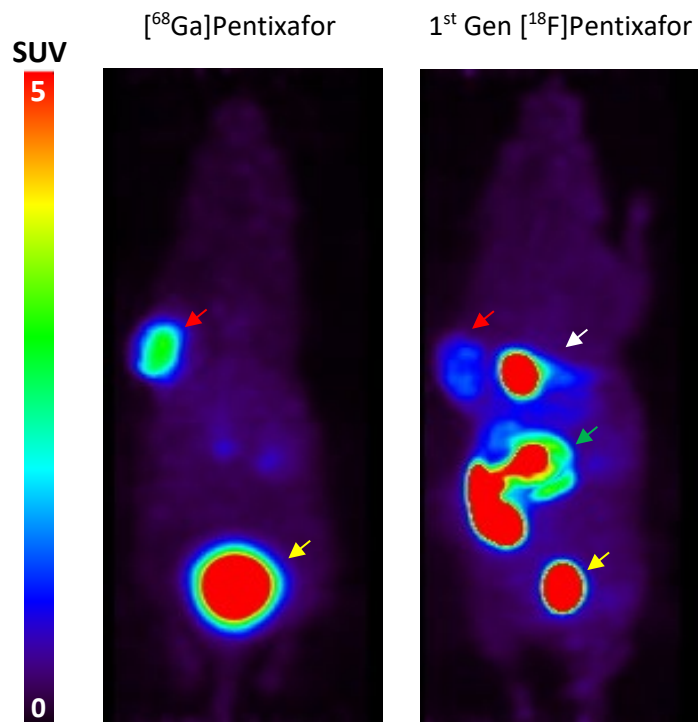


Figure 27: Dynamic PET of [⁶⁸Ga]Pentixafor compared to the previous generation of ¹⁸F-labelled CXCR4 targeted peptides from the Archibald laboratory. Coronal maximum intensity projections, 40-66 min post administration, U87-CXCR4 xenograft (human CXCR4) mouse model (arrow colour code: red – tumour, white – liver, green – gut, yellow – bladder).

2.7 *In vivo* imaging studies

2.7.1 PET-CT scanning experiments

Following the *in vitro* assays, it was decided [¹⁸F]SJA-1028 ([¹⁸F]CPCR4-PEG₄-PEG₄-F) would be the tracer to taken forward to *in vivo* trials. This was because of it having the highest affinity for CXCR4 as well as being the most stable throughout the synthesis process.

A total of 9 unblocked scans were performed on tumour bearing animals and 7 blocked scans on tumour bearing animals. Some animals were scanned multiple times. Tumours are subcutaneous implanted U87-CXCR4 ranging between 250 and >800mm³. However, not all scans were used for analysis due to inadequate injection quality of the tracer resulting in lower quality scan data.

All animals were injected intravenously *via* the tail vein at the start of scan time and scanned dynamically for 90 mins, followed by a CT scan for anatomical reference. Blocked animals received 5 mg/kg SJA05 injected IP, 60 mins prior to tracer injection. Tumour ROIs were drawn freehand to ensure accuracy, as shown in Figure 29. SJA05 is an established low nM affinity tracer that has been well characterised for CXCR4 binding characteristics [133].

Tumour to muscle (T:M) ratios showed a significant tumour uptake (T:M = 2.9 at 50 min), though the excretion route, intended to be modified to go *via* the renal system, appears to be significantly *via* the gut and biliary system, with particularly high uptake in the gallbladder. As noted earlier, Pentixafor is unable to bind to murine CXCR4, so any activity seen should be either the tumour or accumulation from excretion. There appears to be some uptake in the kidneys and bladder, as can be seen on the images and in the biodistribution data, indicating renal excretion.

Given the lipophilicity values found earlier, this is not a particular surprise, being an improvement on the previous “clicked” [¹⁸F]Pentixafor but still significantly less hydrophilic than the established [⁶⁸Ga]Pentixafor. Further modification of the PEG spacer may improve this further, or the introduction of alternate hydrophilic groups.

There is no indication that fluorine is being released from the tracer, such as activity in bones, with metabolite studies showing the tracer is majority stable in urine and liver, though less so in the tumour analysis data, although this may be anomalous.

SUV_{Max} results showed the tracer uptake in the tumour can be blocked, though the differences between the blocked and unblocked are less than ideal, with some activity still visible in the blocked

scans. The blocking agent used (SJA05) has been proven to be successful with targeting CXCR4 in multiple studies and this may indicate some non-specific tumour uptake.

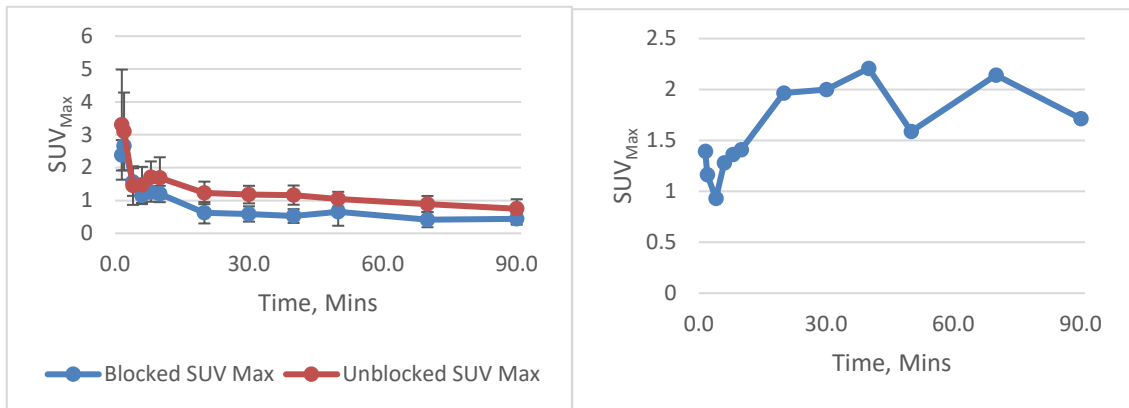


Figure 28: Graphs showing the SUV_{Max} in blocked and unblocked scans, to demonstrate how the tracer can be blocked

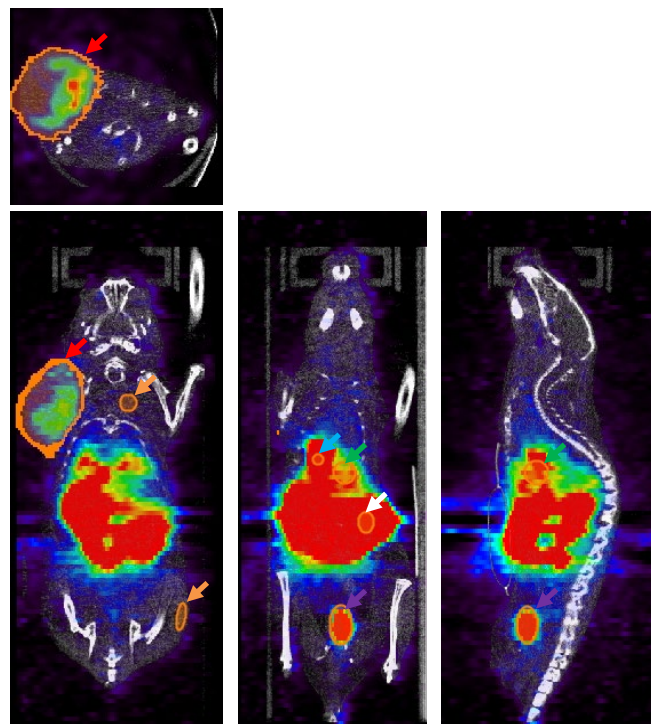


Figure 29: Dynamic PET. Coronal maximum intensity projections, 40-50 min post administration, U87-CXCR4 xenograft (human CXCR4) mouse model. Arrow colour code: red – tumour, white – gut, green – liver, blue – gallbladder, purple – bladder, orange – muscle.

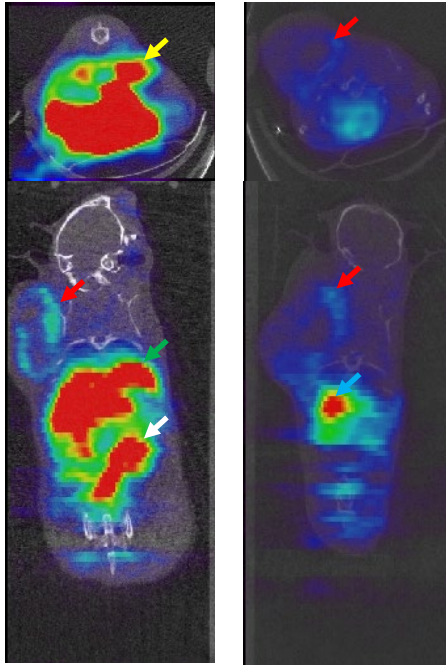


Figure 30: Dynamic PET. Coronal maximum intensity projections, 40-50 min post administration, U87-CXCR4 xenograft (human CXCR4) mouse model. Arrow colour code: red – tumour, white – gut, green – liver, yellow – kidney, blue – gallbladder. Left: Unblocked scan. Right: Scan after blocking dose of SJA05 (5 mg/kg)

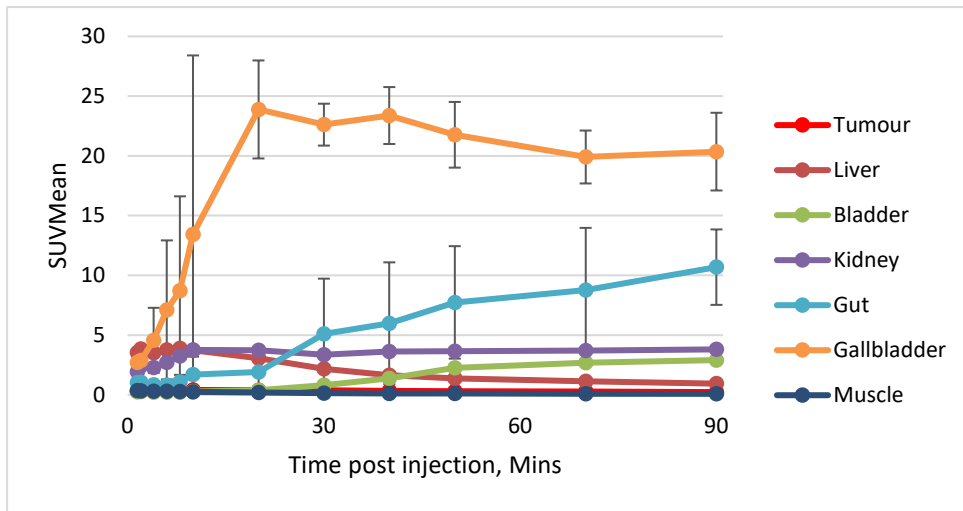


Figure 31: Graph of SUV_{Mean} ± SD of each organ during dynamic PET scan

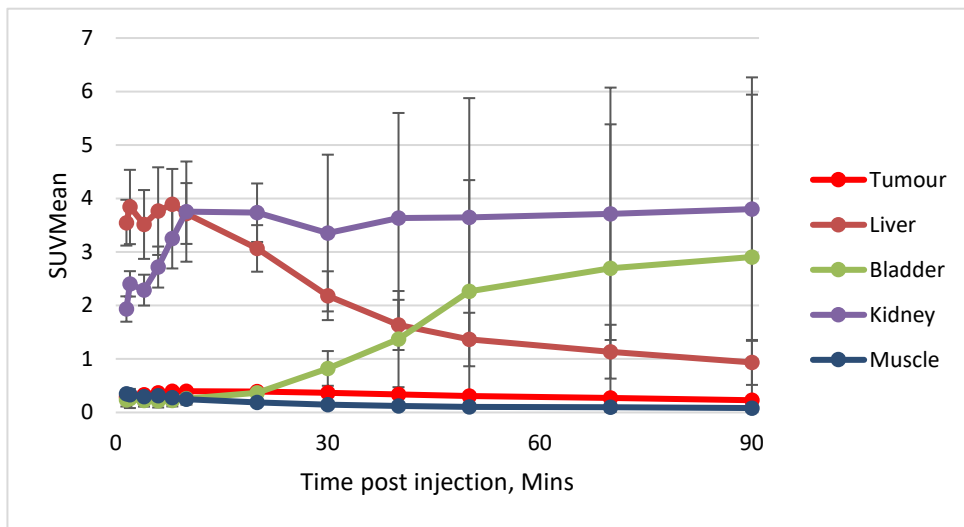


Figure 32: Graph of SUV_{Mean} ± SD of some organs during dynamic PET scan, to separate out the lines more clearly

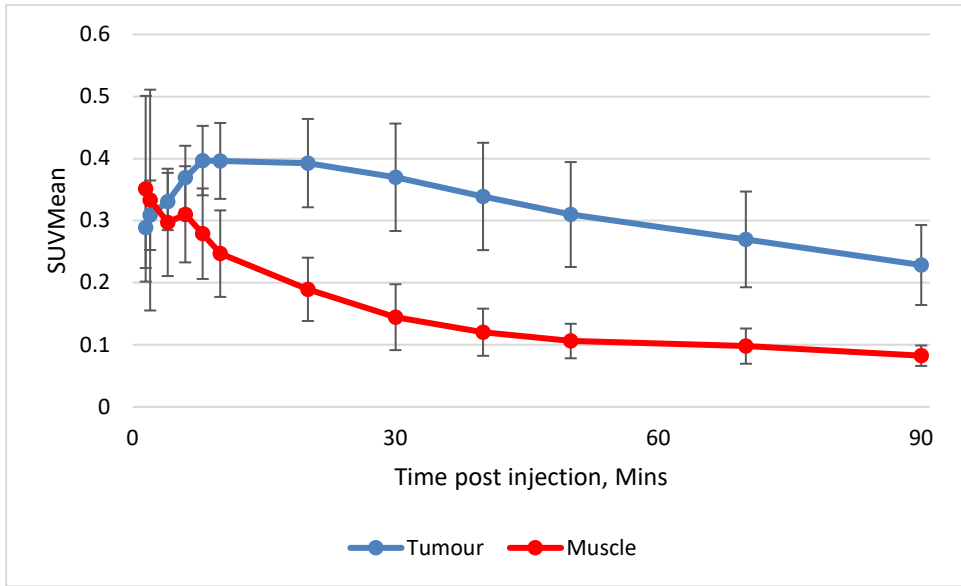


Figure 33: Graph of $SUV_{Mean} \pm SD$ for Tumour and Muscle during dynamic PET scan

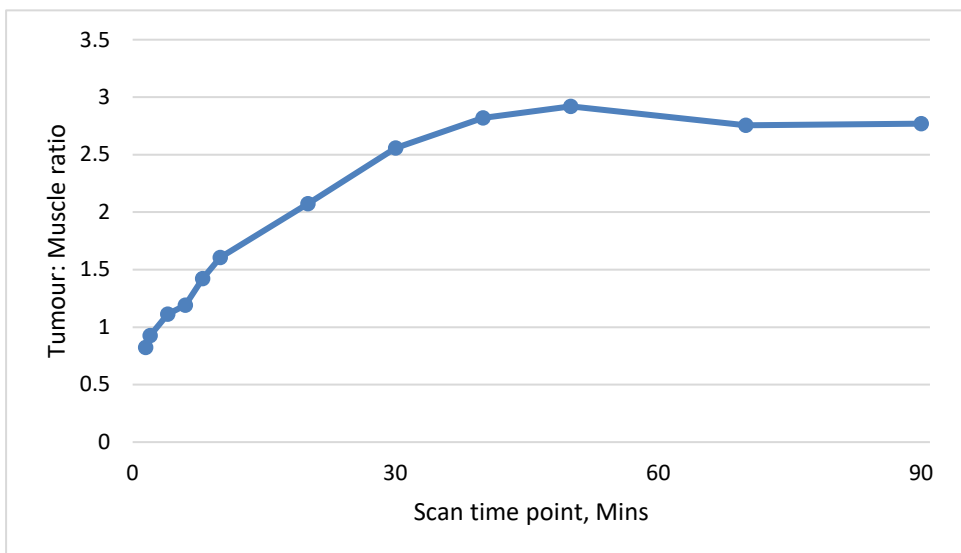


Figure 34: Graph of Tumour to Muscle ratio during dynamic PET scan

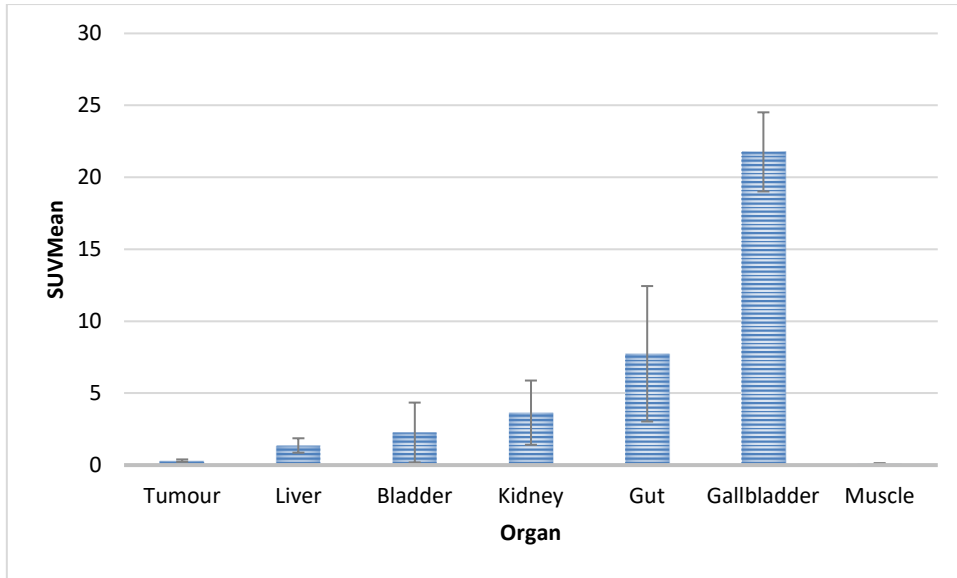


Figure 35: Graph showing the $SUV_{Mean} \pm SD$ of organs at 50 mins post injection, the highest tumour to muscle ratio

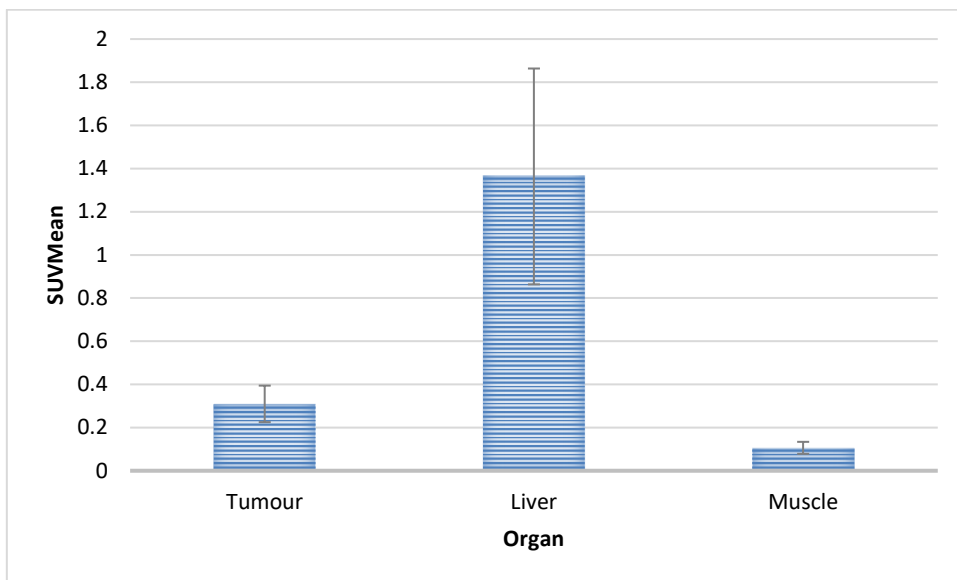


Figure 36: Graph showing the $SUV_{Mean} \pm SD$ of each organ at 50 mins post injection, the highest tumour to muscle ratio, to separate the bars more clearly

2.7.2 Metabolite analysis

At the end of the scan (2 hours post injection), some animals were sacrificed and the fate of the tracer in blood, tumour, liver and urine investigated by radio-HPLC (Column of ACE5 C18 150×4.6 mm; gradient of 5% to 100% in 12 min, MeOH + 0.1% TFA: water + 0.1% TFA MeOH, followed by isocratic 100% MeOH for 5 min, tracer eluted as a sharp peak at 15-16 min). Blood cells were removed by centrifugation at 14500 rpm for 10 min at 4°C, and remaining plasma protein precipitated by addition of the same volume of cold acetonitrile, followed by centrifugation at 14500 rpm for 5 min.

The liver and tumour were frozen in liquid nitrogen, ground to powder in a thermostatic mortar, extracted with a similar volume (w:v) of 50% acetonitrile: water solution and supernatant separated by centrifugation at 14500 rpm for 5 min. Urine proteins were precipitated by addition of a similar volume (v:v) of 70% acetonitrile: water solution and removed by centrifugation in the same way.

Activity was concentrated in urine and liver and was almost undetectable in blood plasma. 20% to 70% activity extracted from tumours (n = 4, n being the number of samples injected for HPLC analysis) was of original tracer, the remainder being from more hydrophilic (but not free [¹⁸F]fluoride) metabolites. Around two thirds (n = 2) of activity in liver and slightly more than two thirds in urine (n = 3), was still the form of original tracer. Only one sample of plasma was analysed due to low activities and difficulties of collecting blood revealing at least four more hydrophilic metabolites accounting for 80% of all activity.

Table 9: Tracer stability summary for selected organs (extraction and analysis by radio-HPLC, 2 hours post injection).

| Organ | Intact radiotracer, % |
|----------------|------------------------------|
| Tumour (n = 3) | 59 ± 12.8 |
| Liver (n = 2) | 68 ± 2.0 |
| Urine (n = 3) | 75 ± 3.3 |
| Plasma (n = 1) | 22 |

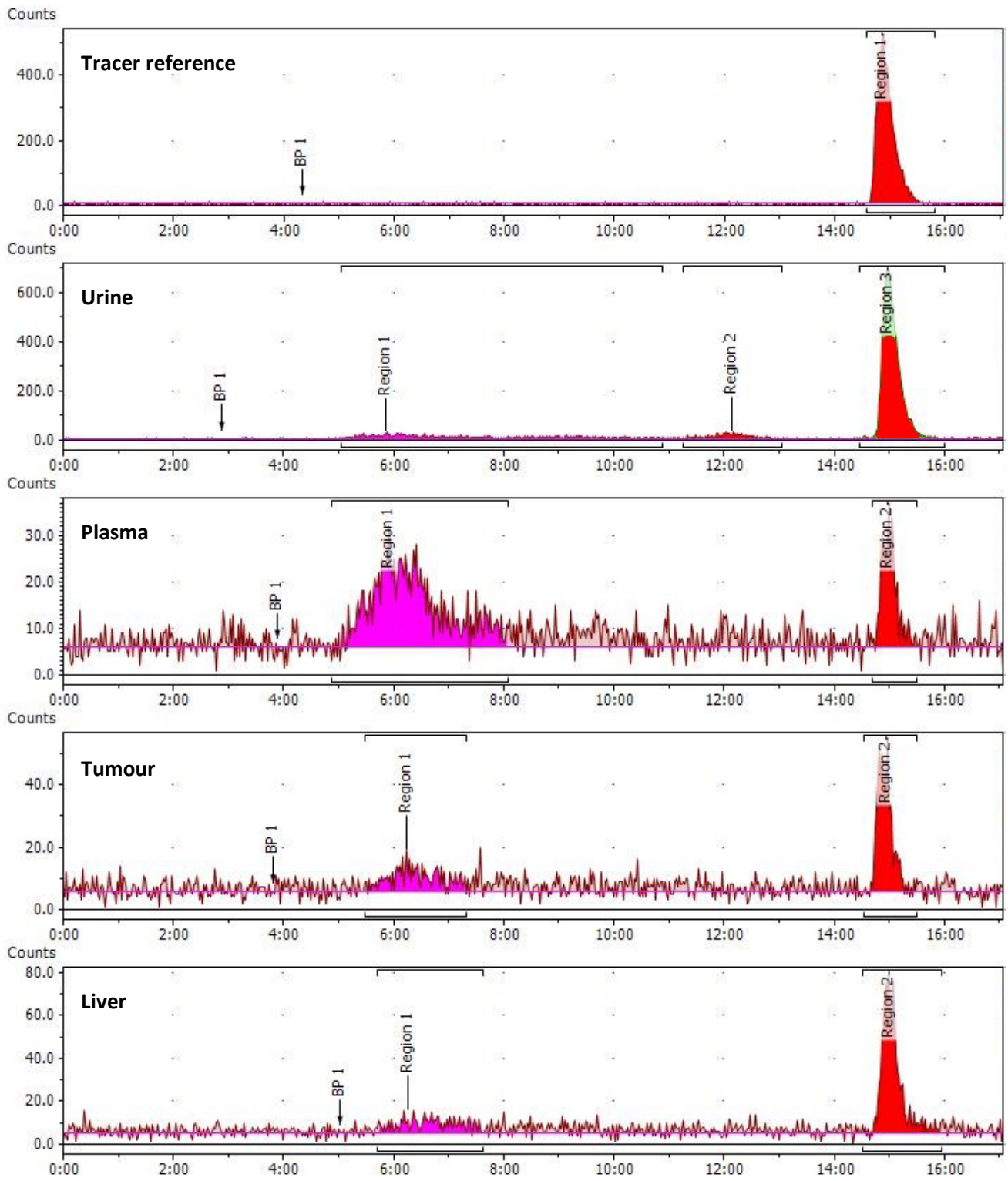


Figure 37: Radio-HPLC chromatograms of the $[^{18}\text{F}]\text{CPCR4-PEG}_4\text{-PEG}_4\text{-F}$ tracer, urine metabolites, plasma metabolites, tumour metabolites and liver metabolites

Chapter Three: Conclusions and Further Work

3.1 Summary

A range of non-radioactive, fluorinated compounds were prepared based on fluorinated PEG chain linkers of various lengths suitable for “click” reaction attachment to a CXCR4-targeting cyclic peptide. These were screened in two CXCR4 binding assays for affinity, with a lead candidate selected for radiolabelling and further characterisation, SJA-1028 (CPCR4-PEG₄-PEG₄-F).

The selected compound was radiolabelled by reacting fluorine-18 with a tosylated PEG linker. This was purified and attached to the CXCR4-targeting peptide *via* a “click” reaction to a second PEG linker (already connected to the peptide *via* standard methods during synthesis of the peptide).

The radiotracer produced was purified before being tested in a SCID/Beige mouse xenograft model with CXCR4 expressing tumour implants. PET imaging showed specific uptake of the radiotracer in tumours, but also significant uptake in the gallbladder and biliary system than was undesirable. The metabolic stability of the tracer shows some degradation but sufficient integrity is maintained for targeted imaging that is compatible with the half-life of fluorine-18.

3.2 Conclusions

In previous research, multiple attempts have been made to synthesise a fluorine-18 radiolabelled CXCR4 targeting tracer. However, there has been a common issue of high lipophilicity, that leads to excretion through the biliary system or gut, instead of the renal system as is seen with Pentixafor. The resulting slower clearance is non-ideal for clinical (or preclinical imaging) both from a patient management perspective and imaging timepoint relative to half-life. The [⁶⁸Ga]Ga³⁺ complex of Pentixafor is highly hydrophilic (mainly due to the chelator properties) giving appropriate pharmacokinetic properties which means background signal has cleared at an appropriate timepoint for clinical imaging. As an additional but unintended side effect, labelling of the tracer also increases binding potency (lower IC₅₀ value). These properties have not been reproduced when designing a fluorine-18 labelled derivative of the same peptide.

The novel tracer in this work was designed with a PEG spacer in an attempt to address the excretion pathway issue, with some success, lowering the lipophilicity when compared to the previous fluorine-18 derivative. However, this change appears to be insufficient to fully deliver the desired the excretion pathway and biodistribution. This resulting preclinical *in vivo* images with the new tracer still show significant levels of activity in the liver, gall bladder and gut that does not rapidly clear.

Whilst tumour uptake does also appear to be significant, with a tumour to muscle ratio of 2.92 at 50 minutes, the sub-optimal blocking study results indicate that there are further improvements to be made to produce an effective peptidic fluorine-18 tracer for CXCR4 imaging.

As was discussed in section 1.4.2.2 the labelling of Pentixafor with gallium-68 increases receptor affinity (lowering the IC_{50}). Although the reason for this is not completely clear, it has been shown that even relatively minor structural modifications can have impact on tracer affinity. Therefore, it is not entirely surprising that the use of a different isotope in fluorine-18 and the prosthetic group investigated lowers the affinity for receptor. The receptor specificity would not be expected to be affected in the same way.

3.3 Potential further work

It is clear from the analysis of the preclinical PET/CT imaging data that further tumour blocking studies are required to gain a clearer picture of how specific the uptake of this tracer is, along with the further pharmacokinetic studies. Some of the data from blocking studies may be less reliable due to the quality of the injection of the tracer (i.e. quality of cannulation and partial tail vein rupture). These studies need to be repeated with further animals to ensure accuracy and reproducibility.

The results from the binding assays, conducted by Prof. Schols and his research team at KU Leuven in Belgium, show some variation in affinity with an issue with one compound having unexpectedly low potency. A further sample of the anomalous compound should be reanalysed to confirm the results. There may be an issue with variable salt contamination in all of the tested peptides and so future confirmation of the salt levels/ organic content would be required in synthesis repeats to ensure that an appropriate comparison can be made between the compounds. The salt contamination arises from the inclusion of trifluoroacetic acid in the mobile for the semi-preparative HPLC. Whether there is any significant effect on the collected imaging data is not clear, but it will impact the molar activity of the tracer and this should be revisited in future studies.

One way to address the issue could be through modified synthesis/ purification methods. The use of alternative methods, as discussed in section 2.2, could be carried out and the products more specifically analysed for salt content along with *in vitro* assays to ensure consistency.

One clear issue is that, although the PEG spacer does seem to have a positive effect on reducing the lipophilicity of the tracer, further modification may be required to optimise this property. Whether through the use of a different type of spacer or a longer PEG chain spacer, further investigation is

required to enhance biodistribution whilst not disrupting the affinity of the tracer for the biological target CXCR4.

Chapter Four: Experimental

4.1 General methods

4.1.1 Solvents and reagents

All chemicals were purchased from Sigma-Aldrich, Fisher, Acros or Chematech and were used as received without further purification. When required to be dry, solvents were dried over activated molecular sieves for a minimum 24 hours.

4.1.2 Mass Spectrometry

Electrospray ionization mass spectrometry was carried out using an Advion expression CMS or a Varian 500 MS spectrometer.

ESI-HRMS (High Resolution Mass Spectrometry) was carried out using a Bruker Maxis Impact.

4.1.3 NMR spectroscopy

All NMR data was collected on a JEOL JNM-LA400 spectrometer at 400.2 MHz for ^1H , using chloroform- d for solvent (CDCl_3), as standard. Chemical shifts are reported in parts per million, ppm. Splitting patterns are assigned as s: singlet, d: doublet, dt: double triplet, t: triplet, q: quartet, m: multiple, td: triple doublet and br: broad signal.

4.1.4 High Performance Liquid Chromatography (HPLC)

HPLC analysis and purification were performed on an Agilent 1100 Series system, equipped with a UV diode array detecting at 210 nm, 230 nm, 250 nm, 254 nm, and 280 nm, controlled by Laura software. The solvent mixtures were made up of methanol + 0.1% trifluoroacetic acid (TFA) / water + 0.1% TFA, with the reported percentages referring to the organic fraction of the solvent mixture.

4.2 Cell Culture and *in vitro* assays

4.2.1 Cell Culture

Brain glioblastoma (U87 and U87-CXCR4) cell lines cultured in DMEM medium (Dulbecco's Modified Eagle Medium), 10% by volume heat inactivated foetal bovine serum (FBS). The U87-CXCR4 cell line media also contained puromycin at a concentration of 1 $\mu\text{L}/\text{mL}$.

The cell cultures were maintained at 37°C in a humidified, CO_2 (5%) controlled atmosphere with subculturing every 2-3 days as appropriate. Cells were used from passage number 35 – 60 and were found to show continual stable expression of CXCR4 and viability, as appropriate.

4.2.2 Cell Counting

The cell concentration was determined by using a haematocytometer. Cells in suspension were diluted 1:1 with 0.2% by volume trypan blue stain. The diluted sample was placed onto a haematocytometer chamber, and the cell density was determined using light microscopy by counting the number of live cells in a set area. The equation below was used to determine the concentration of cells.

$$\text{Cell concentration (cells/mL)} = \text{Averaged cell count} \times 2 \text{ (dilution factor)} \times 10^4 \text{ (volume of chamber)}$$

4.2.3 CXCR4 affinity measurement

4.2.3.1 Competition binding assay

Competition binding assays were performed by Prof. Dominique Schols' group in the Rega Institute, KU Leuven, Belgium.

The assay buffer was prepared by adding 40 mL HEPES (1 M, 20 mM final concentration) to 200 mL Hank's Balanced Salt Solution (HBSS, 10x, without phenol red and without sodium bicarbonate, 1x final concentration). Ultrapure water was added to obtain a final volume of 2 L before 4 g bovine serum albumin (BSA) was added and dissolved *via* magnetic stirring, 0.2% weight/volume. pH was then adjusted to 7.4 using NaOH, and the solution filtered through 0.2 μm pores using a vacuum manifold.

The compounds under investigation were diluted in assay buffer to obtain the desired concentrations for screening, bearing in mind the solution will be diluted further in the assay by a factor of 2x. 100 μL of compound solutions, 2x concentrated, were dispensed into a clear 96-well round bottom plate according to a pre-defined experimental lay out.

0.25 x 10⁶ cells in 50 μL of cell suspension were added from a reagent reservoir into the 96-well plate using a multichannel pipette and the plate incubated for 15 min at RT in the dark. 50 μL of fluorescently labelled CXCL12 (100 ng/mL of CXCL12AF647 in assay buffer, 4x concentrated for 25 ng/mL final concentration) was added, then further incubated for 30 min at RT in the dark. The plate was centrifuged at 400 g for 5 min at RT, supernatant removed from the pelleted cells by flipping over the plate and the plate dried with tissue.

The cells were washed by adding 200 μL of fresh assay buffer to the wells the plate centrifuged for 5 min at 400 g at RT, the supernatant removed by flipping over the plate and again dried on tissue. The cells were then fixed by being resuspended in 200 μL of 1% paraformaldehyde in PBS.

Fluorescence was then quantified by flow cytometry [191].

4.2.3.2 Calcium signalling

Calcium signalling experiments were performed by Prof. Dominique Schols' group in the Rega Institute, KU Leuven, Belgium.

Cells are pre-loaded with the calcium-sensitive fluorescent dye Fluo-3 and incubated with the compound of interest, at the desired concentration, before an additional incubation period with CXCL12. The activation of Fluo-3 which is detected with a Fluorometric Imaging Plate Reader (FLIPR) system [190]. Using a decreasing range of concentration of the compound being tested allows for the IC₅₀ value to be determined.

4.3 *In vivo* experiments

4.3.1 General

All animal procedures were approved by the University of Hull Animal Welfare Ethical Review Body and carried out in accordance with the United Kingdom's Guidance on the Operation of Animals (Scientific Procedures) Act 1986 and the UKCCCR Guidelines 2010.

4.3.2 Tumour implants

Female SCID/Beige mice (21-28 days, 20-25 g; Charles Rivers Laboratories) were anaesthetised with 5% isoflurane and maintained under anaesthesia at 3% isoflurane (oxygen at 1 L/min). Mice were implanted subcutaneously with U87-CXCR4 cells (1 x 10⁶ cells/100 µL in 50% serum-free medium/50% Geltrex[®]) on the upper right shoulder, as described by Fridman *et al.* Tumour growth was monitored bi-weekly by measurements using a calliper. At the time of scanning, the animals used for PET/CT experiments had tumours reaching 250-800 mm³.

4.3.3 PET/CT imaging

PET imaging data were acquired on a Sedecal SuperArgus 2R PET scanner. Mice were induced with 5% isoflurane and maintained under with 3% isoflurane (oxygen at 1 L/min). Whole body PET data acquisition (2 bed positions, 90 min dynamic scan) was synchronised with radiotracer IV injection (3-8 MBq, 200 µL); temperature and respiration were monitored throughout the scan. A CT scan (40 kV, 140 µA, 360 projections, 8 shots) was acquired following each PET scan to show anatomical co-registration. In blocking experiments, the blocking agent was administered 1 hour prior to scan start.

PET data were reconstructed using 3D Ordered Subset Expectation Maximisation (3D-OSEM) algorithm with 16 subsets and 2 iterations and corrections for random, scatter and attenuation.

Images were normalised using the injected dose and animal weight to give Standardised Uptake Values (SUV). Data was analysed using AMIDE and VivoQuant (InVivo, USA) softwares.

4.3.4 Metabolism

Following the scan, 2 hours post injection, some animals were sacrificed and the fate of the tracer in blood, tumour, liver and urine investigated by radio-HPLC (MeOH 0.1% TFA/water 0.1% TFA MeOH gradient, 5 - 100% in 12 min followed by isocratic 100% MeOH for 4 min, tracer eluted as a sharp peak at 15-16 min).

Blood was centrifuged at 14500 rpm, at 4°C for 10 min to separate blood cells from plasma. Plasma proteins were precipitated by addition of the same volume of cold acetonitrile, separated by centrifugation (5 min, 14500 rpm).

Urine proteins were precipitated by addition of the same volume of 70% acetonitrile in water and separated by centrifugation (5 min, 14500 rpm); the resulting supernatant was harvested.

Liver and tumour were frozen in liquid nitrogen, ground into a fine powder in a thermostatic mortar. A pre-weighed aliquot of pulverised liver was resuspended in a similar volume (w/v) of 50% acetonitrile: water solution. The resulting suspension was centrifuged at 14500 rpm, at 4°C for 5 min and the supernatant harvested.

4.4 Peptide synthesis - general methods

4.4.1 General reaction treatments

Linear peptides were synthesised using Fmoc-based solid phase peptide synthesis techniques [188]. Synthesis was carried out in reactors fashioned from 2 mL or 5 mL syringes, fitted with a PTFE frit, depending on the quantity of starting resin being used. Unless otherwise stated, reactions were carried out in dry, amine-free DMF, with gentle shaking on an orbital shaker. All reagents were introduced and removed by use of the syringe reactor plunger. Following each reaction, the reagents were discarded and resin washed three times in recycled dimethylformamide (DMF) and once with clean DMF.

Prior to reactions, Fmoc-Gly-2-Cl-Trt Resin, 100-200 Mesh, 0.54 mmol/g, was weighted directly into the syringe and swollen for 2 hours in dichloromethane (DCM), followed by washing 3 times with DMF and allowed to shake for a further 20 minutes. Following synthesis, or if synthesis is interrupted overnight, the resin was shrunk by washing 3 times in DCM and shaking for 10 minutes, repeating with methanol and diethyl ether. It was then dried under reduced pressure and stored at 4 °C.

4.4.2 Coupling reactions

Coupling agents, HBTU (*N,N,N',N'*-tetramethyl-*O*-(1*H*-benzotriazol-1-yl)uronium hexafluorophosphate) or HATU (1-[Bis(dimethylamino)methylene]-1*H*-1,2,3-triazolo[4,5-*b*]pyridinium 3-oxid hexafluorophosphate) and protected amino acids were allowed to warm to room temperature before being weighted in individual Eppendorf tubes. The coupling agent was fully dissolved in DMF and the solution transferred into the tube containing amino acid, by pipette with disposable tip to avoid contamination. If needed, vortex mixing and sonication were used to aid the dissolution of the amino acid, with a benchtop centrifuge being used to collect the solution at the bottom of the tube. DIPEA (*N,N*-Diisopropylethylamine) was added immediately before the solution was taken up into the reactor, solution should turn a pale yellow. For primary amino acids, a 4-fold excess of reagents and 30- 45 minutes reaction time is sufficient, with HBTU as a coupling reagent. Secondary amines will require HATU as a coupling agent, with up to 2 x 1 hour reaction times, using fresh reagents for the repeat coupling.

4.4.3 Fmoc-deprotection

Fmoc protection groups were removed by a cleavage solution of piperidine in DMF, 50% by volume. Resin was treated for 2 minutes before solution was discarded and the resin treated with fresh solution for a further 5 minutes. Resin was then washed with DMF.

4.4.4 N-methylation

N-methylation was carried out in a 3-step process, in N-methyl-2-pyrrolidone (NMP).

4.4.4.1 o-NBS Protection

A solution of o-NBS-Cl (4 eq.) and collidine (10 eq.) in NMP was added to the resin-bound free amine peptides and shaken for 15 min at room temperature. The resin was washed 4 times with recycled NMP and once with clean NMP.

4.4.4.2 N-methylation

A solution of DBU (3 eq.) in NMP was taken up into the reactor and shaken for 3 min. A solution of dimethylsulfate (10 eq.) in NMP was then also taken up into the reactor and shaken for an additional 2 min. The solution was discarded, the resin washed once with NMP and the same procedure repeated twice more. The resin was washed 4 times with recycled NMP and once with clean NMP.

4.4.4.3 o-NBS Deprotection

For o-NBS deprotection, the resin was treated with a solution of mercaptoethanol (10 eq.) and DBU (5 eq.) in NMP, shaken for 5 minutes. The deprotection procedure was repeated twice more and the resin was washed five times with NMP.

4.4.5 Alloc cleavage

The required volume of DCM is degassed by sonication or bubbling with Argon. A catalytic amount of tetrakis-(triphenylphosphine)palladium ($\text{Pd}(\text{PPh}_3)_4$, 0.3 eq.) is dissolved in degassed DCM. Phenylsilane (PhSiH_3) is added to the solution before the solution is taken up into the reactor and shaken for 1 hour in the dark. This treatment is repeated with fresh reagents for a further hour, with no wash in between.

The resin is then washed in a solution of 0.02M diethylthiocarbamate in DMF (90 mg in 20 ml) for 3x 15 minutes, followed by a wash in 5% DIPEA.

4.4.6 Dde cleavage

Two different Dde cleavage methods were used, depending on if the Dde was cleaved from the linear or cyclic peptide, in solid or liquid phase. Method B was more efficient and was the method used to produce materials for the *in vivo* scanning experiments.

Method A - Cleavage from linear peptide in solid phase

An excess quantity of deprotection mixture was prepared prior to use consisting of 1.25 g (1.8 mmol) hydroxylamine hydrochloride and 0.9 g (1.35 mmol) imidazole suspended in 5 ml of NMP. The mixture was sonicated until complete dissolution. Unused mixture can be stored at -20°C for at least 2 weeks with no loss of stability.

Before being taken up into the reactor, 5 volumes of the mixture were dissolved with 1 volume of DCM, for a total of 1.5 mL. The resin was then shaken for a minimum of 3 hours. There seemed to be no additional by-product formation if left overnight.

Method B - Cleavage from cyclic peptide in liquid phase

2% hydrazine in DCM was added to a vessel containing the dry peptide in powder form, dissolving it, and shaken for 5 minutes at room temperature. The solvent was then removed by rotary evaporation.

4.4.7 Cleavage from trityl chloride resin

Completed linear peptide was cleaved from the resin in 50% hexafluoroisopropanol in DCM for 1 hour, followed by 20% for 1 hour. Solution was concentrated under reduced pressure or under stream of nitrogen. The crude protected peptide purified by semi-preparatory HPLC.

4.4.8 Cyclisation

The linear peptide was diluted in sufficient DMF, (ca. 5 mL/ 0.1 g starting resin), to promote cyclisation rather than the formation of chains. This is treated overnight with diphenylphosphoryl azide (DPPA) (3 eq.) and sodium bicarbonate (5 eq.), with moderate stirring, at room temperature. The DMF was then removed by rotary evaporation and the residue taken up in a small volume of DCM, washed with water and brine, dried over MgSO₄ and concentrated prior to side chain deprotection.

4.4.9 Removal of side chain protection groups

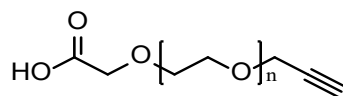
Side chain protections were removed using a cleavage cocktail containing 95% TFA, 2.5% triethylsilane and 2.5% water, shaken for 2 hours. The solution was then concentrated under reduced pressure or under a stream of nitrogen, the crude peptide was precipitated by addition of ice-cold diethyl ether, spun down, ether was decanted, the pellet was washed with further diethyl ether, dried under a stream of nitrogen and stored at -20°C.

4.4.10 Resin Drying

The resin was washed 4 times and suspended in DCM, methanol and diethyl ether, and shaken for 5 minutes each before being dried under vacuum and stored at 4°C.

4.5 PEG linker synthesis

4.5.1 Propargyl-PEG_n-acid linker



4.5.1.1 Synthesis of OH-PEG_n-propargyl

Synthesis was carried out under argon to maintain a dry, inert atmosphere.

The appropriate length polyethylene glycol (PEG) (10 eq.) was weighed into a 3-necked round bottomed flask, diluted in dry tetrahydrofuran (THF) and the flask was flushed with argon. NaH (1.1 eq.) was suspended in dry THF and added dropwise, ensuring the release of hydrogen does not cause an excessive build-up of pressure.

The mixture was then cooled to 10°C. Propargyl bromide (1 eq.), dissolved in THF, was added dropwise over 30 minutes, to promote mono substitution. Once all the propargyl bromide had been added, the reaction mixture was allowed to return to room temperature and left to stir for 2 hours, until no propargyl bromide was visible by TLC (Thin layer chromatography). The addition of heat or being left to stir overnight did not appear to affect the final yield.

The mixture was then quenched with HCl and the THF removed by rotary evaporation. Crude product was extracted with DCM and washed with brine. The organic layer was dried over Na₂SO₄, filtered and concentrated to obtain crude product as an oil. Pure product was obtained by silica gel column chromatography.

4.5.1.2 Synthesis of COOH-PEG_n-propargyl

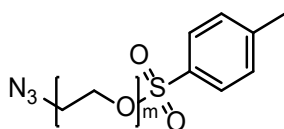
The desired length of propargyl-PEG_n-OH was dissolved in DCM and cooled to 10°C with an ice bath. Tetra-n-butylammonium bromide (0.25 eq.) was then added.

Aqueous NaOH (12 eq.) was formed by dissolving solid NaOH in water at a 1:1 mass: volume ratio and allowed to cool, before being added to the solution and left to stir for 30 minutes. The ice was then removed and bromoacetic acid (1.5 eq.) added to the solution and allowed to stir overnight at room temperature.

The mixture was diluted with water and washed three times with DCM and ethyl acetate. It was then acidified to pH = 2 with nitric acid and the product extracted with ethyl acetate. The extracted layer was washed with brine, dried over MgSO₄ and evaporated *via* rotary evaporation. If NMR analysis

showed high levels of acetic acid, the product was then further dried on a Schlenk line to help remove it, though this did result in lower final yields for the shorter PEG chains.

4.5.2 N₃-PEG_m-Tosyl linker



4.5.2.1 Mono-Tosylation

Synthesis was carried out under argon.

The appropriate length PEG (10 eq.) was diluted in dry DCM and cooled to 0°C. Triethylamine (1.5 eq.) was added dropwise and allowed to stir for 30 minutes. Tosyl chloride (1 eq.) was added slowly, to promote mono-substitution. It can be suspended in dry DCM and added dropwise *via* syringe, helping to maintain the argon atmosphere. The mixture was then allowed to warm and stir overnight at room temperature. The mixture was further diluted with DCM, washed with water, re-extracted with DCM if necessary and washed with 5% citric acid. It was then dried over MgSO₄, filtered and evaporated by rotary evaporation.

4.5.2.2 Substitution of N₃

Tosyl-PEG_m-OH was dissolved in dry DMF and sodium azide (2 eq.) added. The mixture was stirred overnight at 90°C, or until complete (analysed by TLC, Hexane: Ethyl acetate. 20-40% ethyl acetate, depending on length of PEG chain).

The DMF was then removed by rotary evaporation at 55°C, with co-evaporation with water to remove traces. The remaining mixture is dissolved in diethyl ether, sonicated to remove lumps and filtered through celite. Diethyl ether was then removed by evaporation to yield the desired product as an oil.

4.5.2.3 Tosylation 2

N₃-PEG_m-OH was diluted in dry DCM and cooled to 0°C. Triethylamine (3 eq.) was added, followed by tosyl chloride (2 eq., suspended in DCM, added by syringe). The mixture was stirred at RT overnight, or until complete (analysed by TLC).

The mixture was further diluted with DCM, washed with water, reextracted with DCM if necessary and washed with 5% citric acid. It is then dried over MgSO₄, filtered and evaporated by rotary evaporation. Pure product was obtained by silica gel column or plug chromatography, dependent on the results of TLC analysis.

4.6 Radiochemistry

4.6.1 PEG radiolabelling

4.6.1.1 Preparation of fluorine-18

Fluorine-18 was produced from oxygen-18 water by proton bombardment ($^{18}\text{O}(p,n)^{18}\text{F}$) in an ABT compact cyclotron and trapped on a QMA-carb light (Waters) or regular QMA light (Waters), pre-activated by flushing it with 8.4% sodium bicarbonate in water (5 mL) and water (20 mL). The cartridge was eluted with KHCO_3 (0.5 mL, 2.6 mg/mL water) directly into a reaction vessel containing 5 mg of Kryptofix K_{222} in ACN (0.5 mL). Solvents were evaporated at 90-100°C under a gentle stream of inert gas and $\text{K}^{18}\text{F}/\text{K}_{222}$ complex further dried by the addition of 2 x 1 mL ACN.

4.6.1.2 Labelling of PEG precursor

Precursor ($\text{N}_3\text{-PEG}_4\text{-Tosyl}$), dissolved in ACN (0.5 mL), is added into the $\text{K}^{18}\text{F}/\text{K}_{222}$ and fluorine-18 contained in a reaction vessel. The reaction is then heated to 105-110 °C for 10 minutes, before being allowed to cool to below 80°C. Unreacted [^{18}F]fluoride was trapped on an Alumina N light (Waters) cartridge. The solvent was reduced to near dryness by gentle stream of inert gas at 80°C; activity was reconstituted in 800 μL of 20% MeOH /water solution and injected onto semi-preparative HPLC for purification with a MeOH 0.1% TFA gradient in water 0.1% TFA 20 to 40% in 20 min, 4.7 mL/min, $R_t = 12$ min.

The fraction containing radiolabelled prosthetic was collected, diluted 4-fold with water and passed through a homemade cartridge containing HLB C18 (Waters) sorbent (80-100 mg). Trapped product was washed with water (3 mL), dried with inert gas and eluted with THF (0.5 mL) into HPLC champagne vial. If needed, the solvent volume was reduced under gentle stream of inert gas at 50°C.

4.6.2 Copper (I)-catalysed azide-alkyne 1,3-dipolar cycloaddition (CuAAC)

Cu(I) catalysed “click” cycloaddition reaction used to radiolabel alkyne functionalised CPCR4-peptide with a previously prepared ^{18}F -containing azide functionalised prosthetic was optimised as follows [192]:

Stock solutions:

$^{18}\text{F}\text{-PEG}_4\text{-N}_3$: 250-500 MBq in THF (100 μL)

CPCR4 peptide: 10 mM solution in water

CuSO₄·5H₂O: 37 mM solution in water (obtained from a 5-fold dilution of 184 mM solution made from 23 mg dissolved in 500 mL water).

Sodium ascorbate: 250 mM solution in water (obtained by a 5-fold 1.26 M solution made from 50 mg dissolved in 200 mL water, made fresh).

Peptide (10 µL, 1 eq.), THF (20 µL) and copper solution (50 µL, 18 eq.) were added to tris-[(1-benzyl-1H-1,2,3-triazol-4-yl)methyl]amine (1 mg, 1 eq.) contained in an HPLC champagne vial. Mixture was de-oxygenated by bubbling through Argon gas and, under the blanket of argon, were added prosthetic (70-100 µL), followed by sodium ascorbate solution (50 µL, 7 eq. to Cu). Reaction was heated at 50°C in closed vessel for 15 min, diluted with water (0.5 mL) and purified by semi-preparative HPLC with a MeOH 0.1% TFA gradient in water 0.1% TFA 45 to 65% in 20 min, 4.7 mL/min Rt = 12-13 min.

The fraction containing radiolabelled peptide was treated in the same way as previously described for prosthetic precursor. Product was eluted with acid ethanol (0.5 mL, HCl_{conc.} 1 µL/1 mL of ethanol). The solvent was reduced to near dryness under a gentle stream of inert gas and heating at 80°C and reconstituted in PBS solution (0.5 mL). If needed, the pH was adjusted to 7.5 with sodium carbonate solution (0.5 M), formulation was filtered over 0.22 µm filter for sterility and delivered for *in vivo* imaging.

4.6.3 LogD_{7.4} determination

Radiotracer lipophilicity, LogD_{7.4}, was determined by the “shaken-flask” method. Briefly, an aliquot of ethanol solution containing the tracer (1-2 MBq) was dried and resuspended in PBS (700 µL). Three aliquots of 200 µL of the resulting solution were taken, diluted up to 500 µL in PBS and 500 µL of 1-octanol were added into each tube. The samples were vigorously vortex mixed for 10 min, before the centrifugation at 14.5k rpm for 3 min to separate the phases and small aliquots of each were measured in triplicate in an Automated Gamma Counter (Wizard 3” Wallac, UK).

4.6.4 Radio HPLC

Radio HPLC analysis and purification were performed using an Agilent 1100 Series system, equipped with a diode array UV (detection at 254 nm) and LabLogic NaI crystal gamma detectors controlled by Laura software. The solvent mixture used was methanol + 0.1% TFA : water + 0.1% TFA. Percentages given when describing gradients are given as the percentage of organic fraction. Semi-preparative HPLC purifications were performed with an Ace 5 C18, 5 µm, 10 x 250 mm column at a flow rate of 4.7

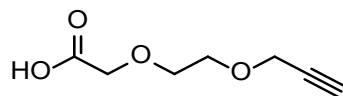
mL/min. Metabolite analysis was performed on an Ace 5 C18, 5 μ m, 4.6 x 150 mm column at a flow rate of 1 mL/min.

4.6.5 Radio-TLC

Reactions were monitored using radio-TLC. Ethyl acetate was used as the eluent on silica gel plates for the stationary phase. Detection was performed with a Scan-RAM Radio TLC detector, controlled by Laura software.

4.7 Compound Synthesis

4.7.1 Synthesis of COOH-PEG₁-CC



Synthesis was carried out as described in section 4.5.1, supplied by George Herbert.

Amounts: Ethylene glycol (24.1 g, 240.8 mmol), propargyl bromide (80% in toluene) (1.12 g, 1.40 g in solvent, 24.08 mmol), sodium hydride (60% in oil) (0.64 g, 1.06 g in solvent, 26.5 mmol), dry THF (Approx. 150 mL).

Yield = 0.48 g, 19.9 % (Low due to water washes)

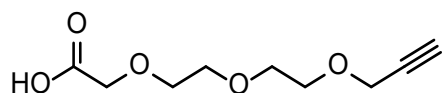
¹H NMR (CDCl₃) δ: (OH-PEG₁-CC), 4.20 (d, 2H, CH₂), 3.76 (t, 2H, CH₂), 3.64 (t, 2H, CH₂), 2.44 (t, 1H, CCH).

Amounts: OH-PEG₁-CC (0.48 g, 4.80 mmol, dissolved in 10 mL DCM), tetra-n-butylammonium bromide (0.44 g, 1.2 mmol), sodium hydroxide (2.3 g, 57.8 mmol), bromoacetic acid (1.0 g, 7.20 mmol).

NMR showed high levels of acetic acid, some of which was removed by treatment on the Schlenk line, but analysis shows this also removed the desired product as well.

¹H NMR (CDCl₃) δ: (COOH-PEG₁-CC), 4.19 (s, 2H, CH₂), 3.76 – 3.80 (m, 2H, CH₂), 3.72 – 3.75 (m, 2H, CH₂), 2.45 (t, 1H, CCH).

4.7.2 Synthesis of COOH-PEG₂-CC



Synthesis was carried out as described in section 4.5.1.

Amounts: Diethylene glycol (10 g, 94.2 mmol), propargyl bromide (80% in toluene) (1.12 g, 1.40 g in solvent, 9.42 mmol), sodium hydride (60% in oil) (0.25 g, 0.412 g in solvent, 10.4 mmol), dry THF (Approx. 60 mL).

Crude product was purified by silica gel column chromatography (6:4 Hexane: Ethyl acetate by volume, increased to 5:5 after 1 L).

This was repeated with the same quantities, with yields of 0.3 g and 0.4 g (28.1 % and 37.5 %), which were then combined for the second stage of synthesis. The quantities for the second stage were then based on this yield.

¹H NMR (CDCl₃) δ: (OH-PEG₂-CC), 4.20 (d, 2H, CH₂), 3.76 – 3.67 (m, 6H, CH₂), 3.60 (t, 2H, CH₂) 2.44 (t, 1H, CCH).

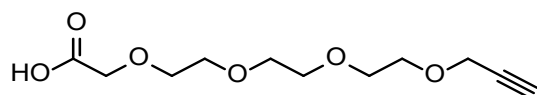
Amounts: OH-PEG₂-CC (0.7 g, 4.86 mmol, dissolved in 10 mL DCM), tetra-n-butylammonium bromide (0.44 g, 1.2 mmol), sodium hydroxide (2.33 g, 58.32 mmol), bromoacetic acid (1.01 g, 7.29 mmol).

Synthesis was repeated a second time with double quantities, to increase stock, with similar yields at all stages.

NMR showed high levels of acetic acid, which were slowly removed by drying on the Schlenk line.

MS (m/z): 225 [M+Na]⁺

4.7.3 Synthesis of COOH-PEG₃-CC



Synthesis was carried out as described in section 4.5.1, supplied by George Herbert.

Amounts: Triethylene glycol (10 g, 66.6 mmol), propargyl bromide (80% in toluene) (0.79 g, 0.99 g in solvent, 6.66 mmol), sodium hydride (60% in oil) (0.175 g, 0.293 g in solvent, 7.33 mmol), dry THF (Approx. 60 mL).

Yield = 0.762 g, 40.5 %

¹H NMR (CDCl₃) δ: (OH-PEG₃-CC), 4.20 (d, 2H, CH₂), 3.74 – 3.64 (m, 10H, CH₂), 3.62 – 3.57 (t, 2H, CH₂), 2.43 (t, 1H, CCH).

Amounts: OH-PEG₃-CC (0.76 g, 4.04 mmol, dissolved in 10 mL DCM), tetra-n-butylammonium bromide (0.37 g, 1.01 mmol), sodium hydroxide (1.94 g, 48.48 mmol), bromoacetic acid (0.84 g, 6.06 mmol).

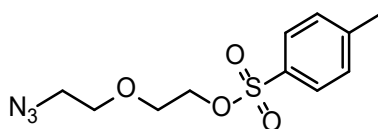
NMR showed high levels of acetic acid, which were slowly removed by treatment on the Schlenk line.

Yield = 0.598 g, 60 %

¹H NMR (CDCl₃) δ: (COOH-PEG₃-CC), 4.20 (d, 2H, CH₂), 4.15 (s, 2H, CH₂), 3.76 – 3.63 (m, 12H, CH₂), 2.43 (t, 1H, CCH).

MS (m/z): 269 [M+Na]⁺

4.7.5 Synthesis of N₃-PEG₂-Tosyl



Synthesis was carried out as described in section 4.5.2.

Amounts:

Stage 1: Diethylene glycol (43.2 g, 407 mmol), triethylamine (6.17 g, 8.5 mL, 61 mmol), tosyl chloride (7.76 g, 40.7 mmol), dry DCM (approx. 50 mL, + 25 mL for tosyl chloride suspension).

Crude product was purified by silica gel column chromatography (5:5 Hexane: Ethyl acetate by volume, increased to 3:7 after 1 L) and treated on the Schlenk line.

Yield = 7.5 g, 70.8%

¹H NMR (CDCl₃) δ: (Tosyl-PEG₂-OH), 7.79 (d, ArH, 2H), 7.36 (d, ArH 2H), 4.21 – 4.15 (m, CH₂, 2H), 3.70 – 3.64 (m, CH₂, 4H), 2.52 (t, CH₂, 2H), 2.44 (s, CH₃, 3H), 1.98 (s, OH, 1H).

Stage 2: Tosyl-PEG₂-OH (7.4 g, 28.4 mmol), sodium azide (3.7 g, 56.8 mmol), dry DMF (approx. 50 mL).

Expected yield = 3.72 g

Yield = 4.4 g, analysed by NMR to still contain DMF at a ratio of 8:5 (Product: DMF).

Therefore, calculated yield = 24.9 mmol, 87.7%

¹H NMR (CDCl₃) δ: (N₃-PEG₂-OH), 3.75 (t, CH₂, 2H), 3.70 (d, CH₂, 2H), 3.61 (t, CH₂, 2H), 3.40 (t, CH₂, 2H), 2.02 (s, OH, 1H).

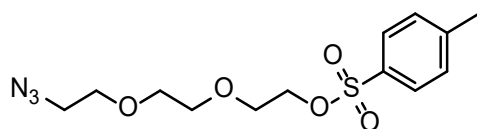
Stage 3: N₃-PEG₂-OH (24.9 mmol), triethylamine (7.55 g, 74.7 mmol), tosyl chloride (9.49 g, 49.8 mmol), dry DCM (approx. 50 mL).

Crude product was purified by silica gel column chromatography (8:2 Hexane: Ethyl acetate by volume, increased to 7:3 after 1 L).

Yield = 5.84 g, 82%

¹H NMR (CDCl₃) δ: (N₃-PEG₂-Tosyl), 7.79 (d, ArH, 2H), 7.33 (d, ArH, 2H), 4.15 (t, CH₂, 2H), 3.68 (t, CH₂, 2H), 3.59 (t, CH₂, 2H), 3.30 (t, CH₂, 2H), 2.43 (s, CH₃, 3H).

4.7.6 Synthesis of N₃-PEG₃-Tosyl



Synthesis was carried out as described in section 4.5.2.

Amounts:

Stage 1: Triethylene glycol (61.1 g, 407 mmol), triethylamine (6.17 g, 8.5 mL, 61 mmol), tosyl chloride (7.76 g, 40.7 mmol), dry DCM (approx. 50 mL, + 25 mL for tosyl chloride suspension).

Crude product was purified by silica gel column chromatography (2:8 Hexane: Ethyl acetate by volume, increased to 100% ethyl acetate after 1 L) and treated on the Schlenk line.

Yield = 10.59 g, 74%

¹H NMR (CDCl₃) δ: (Tosyl-PEG₃-OH), 7.81 – 7.77 (d, ArH, 2H), 7.36 – 7.31 (d, ArH, 2H), 4.16 (t, CH₂, 2H), 3.73 – 3.67 (m, CH₂, 4H), 3.61 (s, CH₂, 4H), 3.59 – 3.55 (m, CH₂, 2H), 2.44 (s, CH₃, 3H), 1.84 (b, OH, 1H).

Stage 2: Tosyl-PEG₃-OH (10.59 g, 34.8 mmol), sodium azide (4.53 g, 69.6 mmol), dry DMF (approx. 50 mL).

Expected yield = 6.1 g

Yield = 6.11 g, analysed by NMR to still contain DMF at a ratio of 3:1 (Product: DMF).

Therefore, calculated yield = 30.6 mmol, 87.9%

¹H NMR (CDCl₃) δ: (N₃-PEG₃-OH), 3.73 (t, CH₂, 2H), 3.67 (b, CH₂, 6H), 3.61 (t, CH₂, 2H), 3.39 (t, CH₂, 2H), 2.19 (b, OH, 1H).

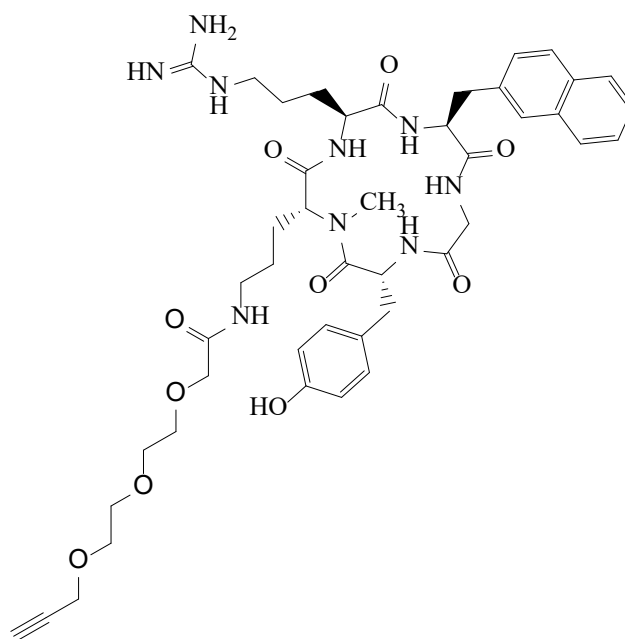
Stage 3: N₃-PEG₃-OH (30.6 mmol), triethylamine (9.29 g, 91.8 mmol), tosyl chloride (11.67 g, 61.2 mmol), dry DCM (approx. 50 mL).

Crude product was purified by silica gel column chromatography (7:3 Hexane: Ethyl acetate by volume).

Yield = 8.39 g, 83%

^1H NMR (CDCl_3) δ : ($\text{N}_3\text{-PEG3-Tosyl}$), 7.79 (d, ArH, 2H), 7.33 (d, ArH, 2H), 4.15 (t, CH_2 , 2H), 3.69 (t, CH_2 , 2H), 3.62 (t, CH_2 , 2H), 3.59 (s, CH_2 , 4H), 3.36 (t, CH_2 , 2H), 2.44 (s, CH_3 , 3H).

4.7.8 Attempted synthesis of CPCr4-PEG₂-CC



Fmoc removal and amino acid coupling were carried out as described in section 4.4. Alloc cleavage was attempted as described in section 4.4.5.

Amounts:

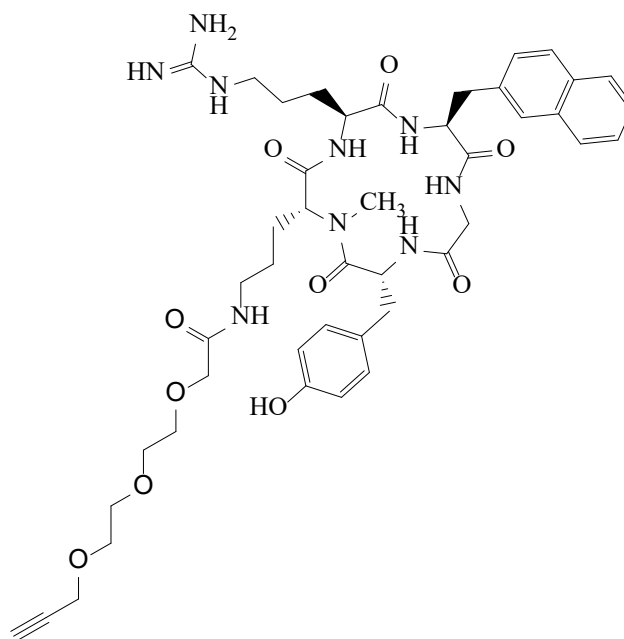
Amino acids - H-Gly-2-Cl-Trt resin (400 mg, 0.54 mmol/g = 0.216 mmol), Fmoc-2Nal-OH (378 mg, 0.864 mmol), Fmoc-Arg(Pbf)-OH (560 mg, 0.864 mmol), Fmoc-D-Orn(Alloc)-OH (378 mg, 0.864 mmol), Fmoc-Tyr(tBu)-OH (428 mg, 0.864 mmol).

Methylation – o-NBS (191 mg, 0.864 mmol), collidine (285 μ L, 2.16 mmol) in 1.5 ml NMP, DBU (96.7 μ L, 0.648 mmol, in 1.5 mL NMP), dimethyl sulphate (204 μ L, 2.16 mmol, in 1 mL NMP), mercaptoethanol (151 μ L, 2.16mmol, in 2 mL NMP), DBU (161 mL, 1.08 mmol)

Alloc cleavage – Pd(PPh₃)₄ (74.8 mg, 0.065 mmol), PhSiH₃ (0.3 ml in 2 ml DCM).

Synthesis was unsuccessful due to a rupture of the syringe reactor during Alloc cleavage due to an increase in pressure, most likely caused by insufficient degassing of the DCM solvent.

4.7.9 Synthesis of CPCr4-PEG₂-CC, using Alloc protected ornithine



Fmoc removal and amino acid coupling were carried out as described in section 4.4. Alloc cleavage was attempted as described in section 4.4.5.

Amounts:

Amino acids - H-Gly-2-Cl-Trt resin (100 mg, 0.54 mmol/g = 0.054 mmol), Fmoc-2Nal-OH (94.5 mg, 0.216 mmol), Fmoc-Arg(Pbf)-OH (140 mg, 0.216 mmol), Fmoc-D-Orn(Alloc)-OH (94.7 mg, 0.216 mmol), Fmoc-Tyr(tBu)-OH (107 mg, 0.216 mmol).

Methylation – o-NBS (47.8 mg, 0.216 mmol), collidine (71.3 μ L, 0.535 mmol) in 0.375 ml NMP, DBU (24.2 μ L, 0.162 mmol, in 0.375 ml NMP), dimethyl sulphate (51.1 μ L, 0.535 mmol, in 0.25 mL NMP), mercaptoethanol (38.9 μ L, 0.535 mmol, in 0.5 mL NMP), DBU (40.3 μ L, 0.27 mmol).

Alloc cleavage – Pd(PPh₃)₄ (18.7 mg, 0.016 mmol), PhSiH₃ (0.075 mL in 0.5 ml DCM).

COOH-PEG₂-CC (4 eq.) – 46.5 mg, 0.216 mmol

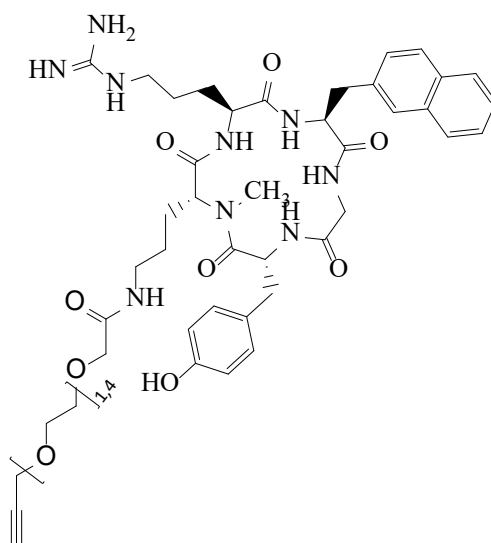
Crude peptide was purified prior to cyclisation using semipreparative HPLC (65-80% Methanol + 0.1% TFA : Water + 0.1 % TFA, peak at 11 mins).

Cyclisation – DPPA (34.9 μ L, 0.127 mmol), NaHCO₃ (22.7 mg, 0.270 mmol), in 5 mL DMF.

Side chain deprotection was carried out as described in section 4.4.9.

MS (m/z): 886 [M+H]⁺

4.7.10 Attempted synthesis of CPCr4-PEG₁-CC and CPCr4-PEG₄-CC



Fmoc removal and amino acid coupling were carried out as described in section 4.4. Alloc cleavage was attempted as described in section 4.4.5, with a 5 mL syringe being used as a reaction vessel at first.

Amounts:

Amino acids - H-Gly-2-Cl-Trt resin (300 mg, 0.54 mmol/g = 0.162 mmol), Fmoc-2Nal-OH (283 mg, 0.648 mmol), Fmoc-Arg(Pbf)-OH (420 mg, 0.648 mmol), Fmoc-D-Orn(Alloc)-OH (284 mg, 0.648 mmol), Fmoc-Tyr(tBu)-OH (321 mg, 0.648 mmol).

Methylation – o-NBS (144 mg, 0.648 mmol), collidine (214 μ L, 1.605 mmol) in 1.3 mL NMP, DBU (72.6 μ L, 0.468 mmol, in 1.3 mL NMP), dimethyl sulphate (153 μ L, 1.605 mmol, in 0.75 mL NMP), mercaptoethanol (113 μ L, 1.605 mmol, in 1.5 mL NMP), DBU (121 μ L, 0.779 mmol).

Alloc cleavage – Pd(PPh₃)₄ (56.2 mg, 0.049 mmol), PhSiH₃ (0.225 mL in 1.5 mL DCM).

Resin was dried and split equally between two 2 mL syringe reaction vessels and re-swollen the next day. Resin does not have to be dried to be do this but it easier to do without loss when dry.

A. COOH-PEG₁-CC (1.5 eq.) – 19.1 mg, 0.121 mmol.

B. COOH-PEG₄-CC (1.5 eq.) – 35.3 mg, 0.121 mmol.

Cyclisation - NaHCO_3 (34.0 mg, 0.624 mmol), DPPA (52.4 μL , 0.190 mmol), in 10 mL DMF (For each peptide).

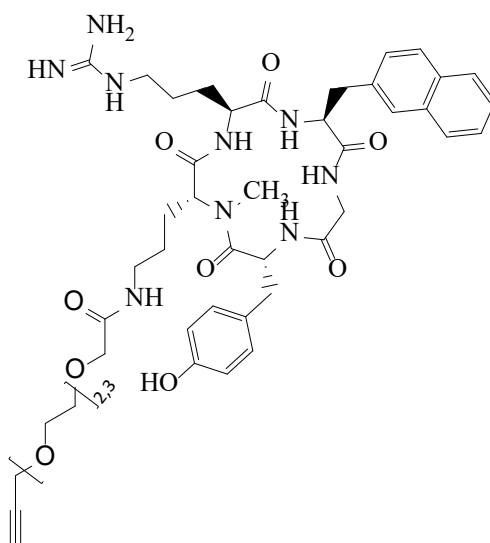
Crude peptides were analysed by HPLC and MS, with unexpected levels of impurities and evidence of Fmoc removal prior to the coupling of the PEG linker. For this reason, the same quantities were repeated, with additional samples taken at each stage to isolate the problem.

MS identified prior to PEG chain coupling:

1251 $[\text{M}+\text{H}]^+$ = Linear, protected CPCR4, the desired structure at this point.

1028 $[\text{M}+\text{H}]^+$ = Linear, protected CPCR4 without Fmoc.

4.7.11 Attempted synthesis of CPCR4-PEG₂-CC and CPCR4-PEG₃-CC



Fmoc removal and amino acid coupling were carried out as described in section 4.4. Alloc cleavage was attempted as described in section 4.4.5, with a 5 mL syringe being used as a reaction vessel at first.

Amounts:

Amino acids - H-Gly-2-Cl-Trt resin (300 mg, 0.54 mmol/g = 0.162 mmol), Fmoc-2Nal-OH (283 mg, 0.648 mmol), Fmoc-Arg(Pbf)-OH (420 mg, 0.648 mmol), Fmoc-D-Orn(Alloc)-OH (284 mg, 0.648 mmol), Fmoc-Tyr(tBu)-OH (321 mg, 0.648 mmol).

Methylation – o-NBS (144 mg, 0.648 mmol), collidine (214 μ L, 1.605 mmol) in 1.3 mL NMP, DBU (72.6 μ L, 0.468 mmol, in 1.3 mL NMP), dimethyl sulphate (153 μ L, 1.605 mmol, in 0.75 mL NMP), mercaptoethanol (113 μ L, 1.605 mmol, in 1.5 mL NMP), DBU (121 μ L, 0.779 mmol).

Alloc cleavage – Pd(PPh₃)₄ (56.2 mg, 0.049 mmol), PhSiH₃ (0.225 mL in 1.5 mL DCM).

Resin was split equally between two 2 mL syringe reaction vessels.

A. COOH-PEG₂-CC (2 eq.) – 32.5 mg, 0.161 mmol.

B. COOH-PEG₃-CC (2 eq.) – 39.6 mg, 0.161 mmol.

Cyclisation - NaHCO₃ (34.0 mg, 0.624 mmol), DPPA (52.4 μ L, 0.190 mmol), in 10 mL DMF (For each peptide).

As with the previous attempt, with PEG₁ and PEG₄, crude peptides were analysed by HPLC and MS, with samples taken at several points during the synthesis process.

MS identified prior to PEG coupling:

1251 [M+H]⁺ (Linear, protected CPCR4, target compound for this step)

1028 [M+H]⁺ (Linear, protected CPCR4, -Fmoc)

MS identified prior to cyclisation:

1434 [M+H]⁺ = Linear, protected CPCR4-PEG₂-CC, target compound for this step.

1396 [M+H]⁺ = Linear, protected CPCR4-PEG₂-CC, with extra PEG₂-CC in place of Fmoc group.

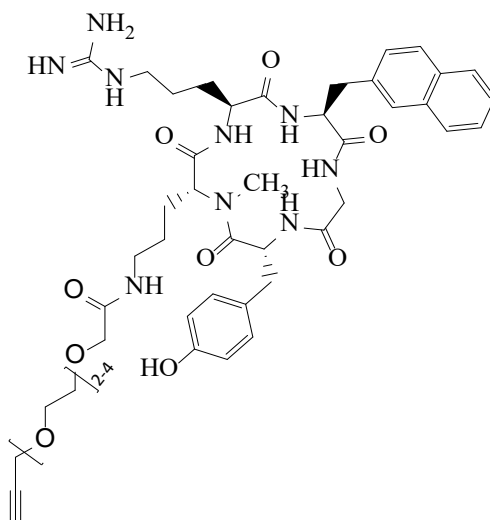
1060 [M+H]⁺ = Linear, protected CPCR4-PEG₂-CC without Fmoc.

1478 [M+H]⁺ = Linear, protected CPCR4-PEG₃-CC, target compound for this step.

1484 [M+H]⁺ = Linear, protected CPCR4-PEG₃-CC, with extra PEG₃-CC in place of Fmoc group.

1104 [M+H]⁺ = Linear, protected CPCR4-PEG₄-CC without Fmoc.

4.7.13 Synthesis of CPCr4-PEG₍₂₋₄₎-CC, using Dde protected ornithine, with Method B of Dde cleavage



This was carried out three time concurrently with the same amounts for each PEG version.

Fmoc removal and amino acid coupling were carried out as described in section 4.4.

Amounts:

Amino acids – H-Gly-2-Cl-Trt resin (300 mg, 0.54 mmol/g = 0.162 mmol), Fmoc-2Nal-OH (283 mg, 0.647 mmol), Fmoc-Arg(Pbf)-OH (420 mg, 0.647 mmol), Fmoc-D-Orn(Dde)-OH (336 mg, 0.647 mmol), Fmoc-Tyr(tBu)-OH (321 mg, 0.647 mmol).

Methylation – o-NBS (144 mg, 0.647 mmol), collidine (214 μ L, 1.76 mmol) in 1.5 mL NMP, DBU (72.6 μ L, 0.477 mmol, in 1.5 mL NMP), dimethyl sulphate (153 μ L, 1.21 mmol, in 1 mL NMP), mercaptoethanol (113 μ L, 1.44 mmol, in 1.5 mL NMP), DBU (121 μ L, 0.795 mmol).

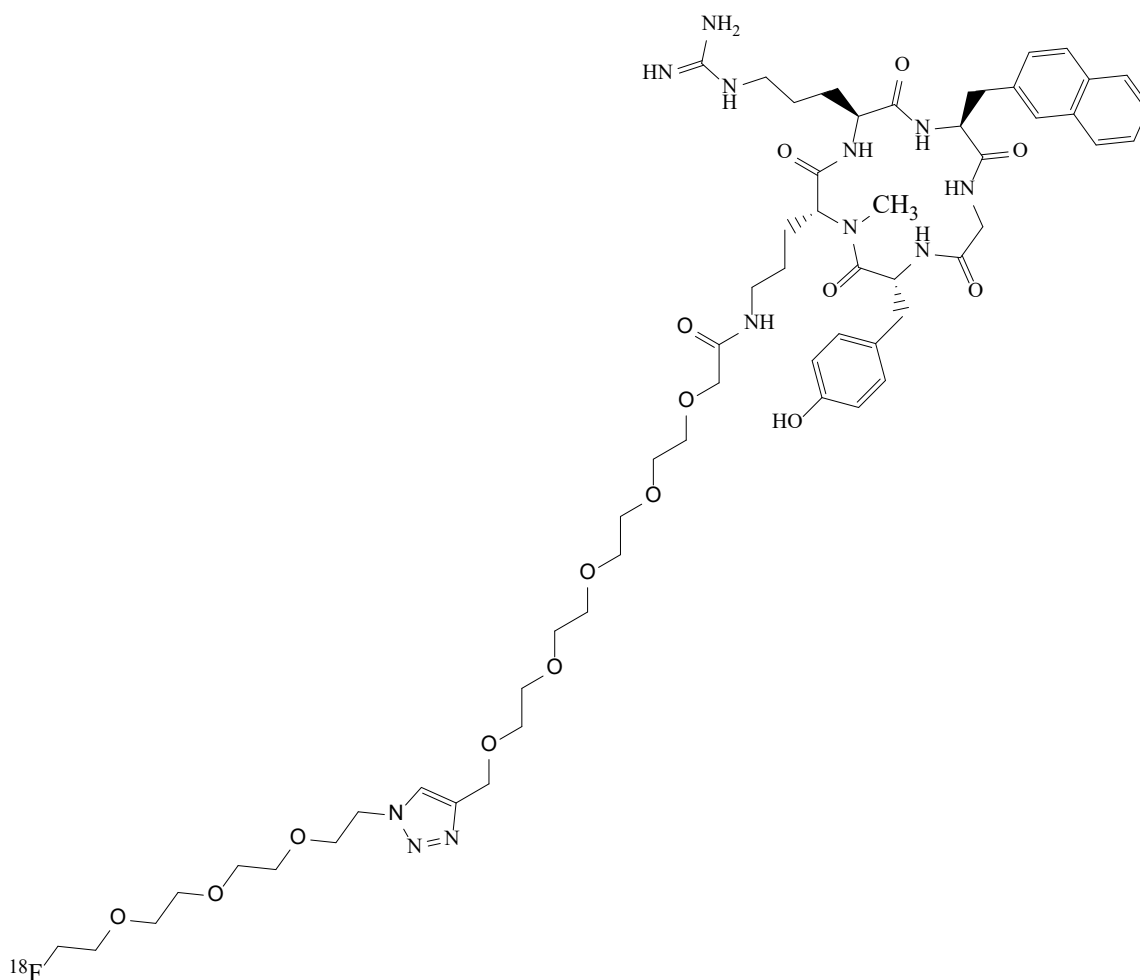
Cyclisation – DPPA (105 μ L, 0.381 mmol), NaHCO₃ (68 mg, 0.809 mmol), in 20 mL DMF.

Dde cleavage – Method B as described in Section 4.4.6.

COOH-PEG₂-CC (131 mg, 0.648 mmol), COOH-PEG₃-CC (166 mg, 0.648 mmol) or COOH-PEG₄-CC (201 mg, 0.648 mmol), as required.

Deprotection of side chains was carried out as described in section 4.4.9.

4.7.14 Synthesis of CPCR4-PEG₄-PEG₄-¹⁸F



The radiotracer was prepared for *in vivo* imaging from peptides and prosthetics synthesised earlier. The process is described in detail in section 4.6.

A total of 5 batches of tracer were used for *in vivo* investigation, with an average of 2138 MBq fluorine-18 eluted from the cyclotron.

Radiolabelling yield for the prosthetic, ([¹⁸F]N₃-PEG₄-F), was 53 ± 10 % (decay corrected), with the procedure taking 120 minutes (n = 5).

Radiolabelling yield from the CuAAC reactions was 62 ± 10 % (decay corrected), taking an average 61 minutes (n = 4). One procedure took longer due to unrelated laboratory activities.

Final formulation yield was 37 ± 15 % (decay corrected), delivering 103 ± 53 MBq (n = 5).

References

1. Bushberg, J.T., J.A. Leidholdt, and J.M. Boone, *Introduction to medical imaging*, in *The essential physics of medical imaging*, C.W. Mitchell, Editor. 2012, Lippincott Williams and Wilkins: Philadelphia, PA. p. 3-17.
2. Suetens, P., *Fundamentals of Medical Imaging*. 2009, Cambridge University Press.
3. Werner, S.Q., E., *J Clin Endocrinol Metab*, 1948. **8**: p. 597-597.
4. Buck, A.K., et al., *Spect/Ct*. *J Nucl Med*, 2008. **49**(8): p. 1305-19.
5. England, N., *Annual Statistical Release 2019/20*. 2020.
6. Knight, J.C. and F.R. Wuest, *Nuclear (PET/SPECT) and optical imaging probes targeting the CXCR4 chemokine receptor*. *MedChemComm*, 2012. **3**(9).
7. Kreisl, W.C., et al., *PET imaging of neuroinflammation in neurological disorders*. *Lancet Neurol*, 2020. **19**(11): p. 940-950.
8. Knaapen, P., et al., *Cardiac PET-CT: Advanced hybrid imaging for the detection of coronary artery disease*. *Neth Heart J*, 2010. **18**(2): p. 90-98.
9. Morbelli, S., et al., *Role of 18F-FDG-PET imaging in the diagnosis of autoimmune encephalitis*. *Lancet Neurol*, 2016. **15**(10): p. 1009-1010.
10. Diéguez, P., et al., *Utility of PET/CT for the diagnostic and disease management: A study of 88 patients from an autoimmune diseases hospital unit in a 2-year period*, in *Ann Rheum Dis*. 2018. p. 1703.3-1704.
11. Yamashita, H., K. Kubota, and A. Mimori, *Clinical value of whole-body PET/CT in patients with active rheumatic diseases*. *Arthritis Res Ther*, 2014. **16**: p. 1-12.
12. J., L.N. and W. W., *The Chemistry of Molecular Imaging*. 2015, John Wiley & Sons: New Jersey. p. 1-25.
13. Webb, A., *Introduction to Biomedical Imaging*. 2003, New Jersey: John Wiley & Sons, Inc. 250.
14. Waterstram-Rich, K.M. and D. Gilmore, *Nuclear Medicine and PET/CT: Technology and Techniques*. 8th ed. 2017, St. Louis, Missouri: Elsevier. 682.
15. Conti, M. and B. Bendriem, *The new opportunities for high time resolution clinical TOF PET*. *Clin Transl Imaging*, 2019. **7**(2): p. 139-147.
16. Lecoq, P. and S. Gundacker, *SiPM applications in positron emission tomography: toward ultimate PET time-of-flight resolution*. *Eur Phys J Plus*, 2021. **136**(3).
17. Jones, T. and D. Townsend, *History and future technical innovation in positron emission tomography*. *J Med Imag*, 2017. **4**(1): p. 011013.
18. Townsend, D.W., *Combined positron emission tomography-computed tomography: the historical perspective*. *Semin Ultrasound CT*, 2008. **29**(4): p. 232-5.
19. Hasegawa, B.H., et al., *Object-specific attenuation correction of SPECT with correlated dual-energy X-ray CT*. *IEEE T Nucl Sci*, 1993. **40**(4).
20. Hutton, B.F., *The origins of SPECT and SPECT/CT*. *Eur J Nucl Med Mol I*, 2014. **41 Suppl 1**: p. S3-16.
21. Weissleder, R., et al., *Molecular Imaging: Principles and Practice*. 2010: People's Medical Publishing House - USA. 1357.

22. Kuruva, M., V.M. Moncayo, and R.B. Peterson, *PET and SPECT Imaging of Epilepsy: Technical Considerations, Pathologies, and Pitfalls*. Semin Ultrasound CT, 2020. **41**(6): p. 551-561.
23. *Introduction to Radiation Protection*. Graduate Texts in Physics. 2010.
24. Finessi, M., G. Bisi, and D. Deandrei, *Hyperglycemia and 18F-FDG PET/CT, issues and problem solving: a literature review*. Acta Diabetol, 2020. **57**(3): p. 253-262.
25. Ali, S.A. and M.A.E. Hamed, *The diagnostic efficacy of whole body 18F-FDG PET CT in detection of unexpected second primary malignancy in cancer patients*. Egypt J Radiol Nucl Med, 2017. **48**(3): p. 671-676.
26. Warburg, O., F. Wind, and E. Negelein, *The Metabolism of Tumors in the Body*. J Gen Physiol, 1926. **8**(6): p. 519-530.
27. Smith, T., *Mammalian hexokinases and their abnormal expression in cancer* Brit J Biomed Sci, 2000. **57**(2): p. 170-178.
28. Cox, B.L., T.R. Mackie, and K.W. Eliceiri, *The sweet spot: FDG and other 2-carbon glucose analogs for multi-modal metabolic imaging of tumor metabolism*. Am J Nucl Med Mol Imaging, 2015. **5**(1): p. 1-13.
29. Ladefoged, C.N., et al., *Low-dose PET image noise reduction using deep learning: application to cardiac viability FDG imaging in patients with ischemic heart disease*. Phys Med Biol, 2021. **66**(5): p. 054003.
30. Steiner, A., et al., *Diagnostic efficiency of whole-body (18)F-FDG PET/MRI, MRI alone, and SUV and ADC values in staging of primary uterine cervical cancer*. Cancer Imaging, 2021. **21**(1): p. 16.
31. Lind, P., et al., *Advantages and limitations of FDG PET in the follow-up of breast cancer*. Eur J Nucl Med Mol I, 2004. **31 Suppl 1**: p. S125-34.
32. Yu, X., et al., *Advantages and disadvantages of F-18 fluorodeoxyglucose positron emission tomography/computed tomography in carcinoma of unknown primary*. Oncol Lett, 2016. **12**(5): p. 3785-3792.
33. Keski-Santti, H., et al., *FDG-PET/CT in the Assessment of Treatment Response after Oncologic Treatment of Head and Neck Squamous Cell Carcinoma*. Clin Med Insights Ear Nose Throat, 2014. **7**: p. 25-9.
34. Kumar, R., et al., *18F-FDG PET for Evaluation of the Treatment Response in Patients with Gastrointestinal Tract Lymphomas*. J Nucl Med, 2004. **45**: p. 1796–1803.
35. Dell'Aquila, A.M., et al., *Fluorine-18 fluorodeoxyglucose positron emission tomography/computed tomography for improving diagnosis of infection in patients on CF-LVAD: longing for more 'insights'*. Eur Heart J-Card Img, 2018. **19**(5): p. 532-543.
36. Smith, D.L., W.A. Breeman, and J. Sims-Mourtada, *The untapped potential of Gallium 68-PET: the next wave of 68Ga-agents*. Appl Radiat Isotopes, 2013. **76**: p. 14-23.
37. Banerjee, S.R. and M.G. Pomper, *Clinical applications of Gallium-68*. Appl Radiat Isotopes, 2013. **76**: p. 2-13.
38. Sun, X., et al., *Peptide-based imaging agents for cancer detection*. Adv Drug Deliv Rev, 2017. **110-111**: p. 38-51.
39. Henze, M., et al., *PET Imaging of Somatostatin Receptors Using [68GA]DOTA-D-Phe1-Tyr3-Octreotide: First Results in Patients with Meningiomas*. J Nucl Med, 2001. **42**(7): p. 1053-6.

40. Basu, S., et al., *Peptide Receptor Radionuclide Therapy of Neuroendocrine Tumors*. Semin Nucl Med, 2020. **50**(5): p. 447-464.
41. Miele, E., et al., *Positron Emission Tomography (PET) radiotracers in oncology--utility of 18F-Fluoro-deoxy-glucose (FDG)-PET in the management of patients with non-small-cell lung cancer (NSCLC)*. J Exp Clin Canc Res, 2008. **27**: p. 52.
42. Adams, S., et al., *Limited value of fluorine-18 fluorodeoxyglucose positron emission tomography for the imaging of neuroendocrine tumours*. Eur J Nucl Med, 1998. **25**(1): p. 79-83.
43. Lee, H.J., E.B. Ehlerding, and W. Cai, *Antibody-Based Tracers for PET/SPECT Imaging of Chronic Inflammatory Diseases*. Chembiochem, 2019. **20**(4): p. 422-436.
44. Li, C. and M. Tian, *Drug Delivery Applications of Noninvasive Imaging*. 1 ed. 2013, New Jersey: John Wiley & Sons.
45. Chianelli, M., et al., *Radiopharmaceuticals for the study of inflammatory processes: a review* Nucl Med Commun, 1997. **18**(5): p. 437-55.
46. Harries, M. and I. Smith, *The development and clinical use of trastuzumab (Herceptin)*. Endocr-Relat Cancer, 2002. **9**: p. 75-85.
47. Wong, W.M., *Trastuzumab: Anti-HER2 Antibody for Treatment of Metastatic Breast Cancer*. Cancer Pract, 1999. **7**(1): p. 48-50.
48. Tang, M., et al., *Cardiac assessment in Australian patients receiving (neo)adjuvant trastuzumab for HER2-positive early breast cancer: a population-based study*. Breast Cancer Res Tr, 2021.
49. Frankel, C., *Development and Clinical Overview of Trastuzumab (Herceptin)*. Semin Oncol Nurs, 2000. **16**(4): p. 13-17.
50. McCormack, P.L., *Pertuzumab: A Review of Its Use for First-Line Combination Treatment of HER2-Positive Metastatic Breast Cancer*. Drugs, 2013. **73**(13): p. 1491-1502.
51. DuMond, B., et al., *Fixed-dose combination of pertuzumab and trastuzumab for subcutaneous injection in patients with HER2-positive breast cancer: A multidisciplinary approach*. J Oncol Pharm Pract, 2021: p. 1078155221999712.
52. Azad, B.B., et al., *A fully human CXCR4 antibody demonstrates diagnostic utility and therapeutic efficacy in solid tumor xenografts*. Oncotarget, 2016. **7**(11): p. 12344-12358.
53. Kashyap, M.K., et al., *Ulocuplumab (BMS-936564 / MDX1338): a fully human anti-CXCR4 antibody induces cell death in chronic lymphocytic leukemia mediated through a reactive oxygen species-dependent pathway*. Oncotarget, 2015. **7**(3): p. 2809-2822.
54. Ghobrial, I.M., et al., *A Phase Ib/II Trial of the First-in-Class Anti-CXCR4 Antibody Ulocuplumab in Combination with Lenalidomide or Bortezomib Plus Dexamethasone in Relapsed Multiple Myeloma*. Clin Cancer Res, 2020. **26**(2): p. 344-353.
55. Klunk, W.E., et al., *Imaging Brain Amyloid in Alzheimer's Disease with Pittsburgh Compound-B*. Ann Neurol, 2004. **55**: p. 306-319.
56. Kitajima, K., et al., *Clinical impact of 11C-Pittsburgh compound-B positron emission tomography in addition to magnetic resonance imaging and single-photon emission computed tomography on diagnosis of mild cognitive impairment to Alzheimer's disease*. Medicine, 2021. **100**(3): p. e23969.
57. Maqsood, H., et al., *Prognostication of cardiac amyloidosis by pittsburgh b compound positron emission tomography*. Eur Heart J, 2020. **41**(Supplement_2).

58. Lee, S.P., et al., *Pittsburgh B Compound Positron Emission Tomography in Patients With AL Cardiac Amyloidosis*. *J Am Coll Cardiol*, 2020. **75**(4): p. 380-390.
59. Wolk, D.A., et al., *Use of Flutemetamol F 18-Labeled Positron Emission Tomography and Other Biomarkers to Assess Risk of Clinical Progression in Patients With Amnesic Mild Cognitive Impairment*. *JAMA Neurol*, 2018. **75**(9): p. 1114-1123.
60. Yang, L., D. Rieves, and C. Ganley, *Brain Amyloid Imaging — FDA Approval of Florbetapir F18 Injection*. *New Engl J Med*, 2012. **367**(10): p. 885-887.
61. Cho, S.H., et al., *Concordance in detecting amyloid positivity between (18)F-florbetaben and (18)F-flutemetamol amyloid PET using quantitative and qualitative assessments*. *Sci Rep*, 2020. **10**(1): p. 19576.
62. Jie, C., et al., *Tauvid: The First FDA-Approved PET Tracer for Imaging Tau Pathology in Alzheimer's Disease*. *Pharmaceuticals*, 2021. **14**(2).
63. Been, L.B., et al., *[18F]FLT-PET in oncology: current status and opportunities*. *Eur J Nucl Med Mol I*, 2004. **31**(12): p. 1659-72.
64. Bollineni, V.R., et al., *A systematic review on [(18)F]FLT-PET uptake as a measure of treatment response in cancer patients*. *Eur J Cancer*, 2016. **55**: p. 81-97.
65. Sanghera, B., et al., *FLT PET-CT in evaluation of treatment response*. *Indian J Nucl Med*, 2014. **29**(2): p. 65-73.
66. Welch, M.J., C.J. Hawker, and K.L. Wooley, *The advantages of nanoparticles for PET*. *J Nucl Med*, 2009. **50**(11): p. 1743-6.
67. Ehman, E.C., et al., *PET/MRI: Where might it replace PET/CT?* *J Magn Reson Imaging*, 2017. **46**(5): p. 1247-1262.
68. Pellico, J., et al., *Fast synthesis and bioconjugation of (68) Ga core-doped extremely small iron oxide nanoparticles for PET/MR imaging*. *Contrast Media Mol I*, 2016. **11**(3): p. 203-10.
69. Pellico, J., et al., *In vivo imaging of lung inflammation with neutrophil-specific (68)Ga nano-radiotracer*. *Sci Rep*, 2017. **7**(1): p. 13242.
70. Liu, Z., et al., *99mTc-labeled RGD-BBN peptide for small-animal SPECT/CT of lung carcinoma*. *Mol Pharm*, 2012. **9**(5): p. 1409-17.
71. Sarcinelli, M.A., et al., *Nanoradiopharmaceuticals for breast cancer imaging: development, characterization, and imaging in induced animals*. *OncoTargets Ther*, 2016. **9**: p. 5847-5854.
72. Mohtavinejad, N., et al., *Technetium-99 m-PEGylated dendrimer-G2-(Dabcyle-Lys(6),Phe(7))-pHBSP: A novel Nano-Radiotracer for molecular and early detecting of cardiac ischemic region*. *Bioorg Chem*, 2020. **98**: p. 103731.
73. Balkwick, F., *Nat. Rev. Cancer*. 2004.
74. Wang, J. and H. Knaut, *Chemokine signaling in development and disease*. *Development*, 2014. **141**(22): p. 4199-205.
75. Chatterjee, S., B.B. Azad, and S. Nimmagassa, *Emerging Applications of Molecular Imaging to Oncology*, M.G. Pomper and P.B. Fisher, Editors. 2014, Elsevier Academic Press Inc: San Diego. p. 31-82.
76. Zlotnik, A. and O. Yoshie, *The chemokine superfamily revisited*. *Immunity*, 2012. **36**(5): p. 705-16.
77. Teicher, B.A. and S.P. Fricker, *CXCL12 (SDF-1)/CXCR4 pathway in cancer*. *Clin Cancer Res*, 2010. **16**(11): p. 2927-31.

78. Balkwill, F.R., *The chemokine system and cancer*. J Pathol, 2012. **226**(2): p. 148-57.
79. Chen, K., et al., *Chemokines in homeostasis and diseases*. Cell Mol Immunol, 2018. **15**(4): p. 324-334.
80. Lee, R., *Development and Evaluation of CXCR4 Receptor Targeted Probes for Medical Imaging Applications*. 2017, University of Hull. p. 413.
81. Proudfoot, A.E.I., *Chemokine Receptors: Multifaceted Therapeutic Targets*. Nat Rev Immunol, 2002. **2**: p. 106-115.
82. Wells, T.N., et al., *Chemokine blockers--therapeutics in the making?* Trends Pharmacol Sci, 2006. **27**(1): p. 41-7.
83. Balabanian, K., et al., *The chemokine SDF-1/CXCL12 binds to and signals through the orphan receptor RDC1 in T lymphocytes*. J Biol Chem, 2005. **280**(42): p. 35760-6.
84. Richard, C.L. and J. Blay, PPAR Res, 2008(19).
85. UK, C.R. [cited 2020 20/03/2020]; Available from: <https://www.cancerresearchuk.org/health-professional/cancer-statistics-for-the-uk>.
86. Hanahan, D. and R.A. Weinberg, *The Hallmarks of Cancer*. Cell, 2000. **100**: p. 57–70.
87. Hanahan, D. and R.A. Weinberg, *Hallmarks of cancer: the next generation*. Cell, 2011. **144**(5): p. 646-74.
88. Encinas, G., et al., *Somatic mutations in early onset luminal breast cancer*. Oncotarget, 2018. **9**(32): p. 22460-22479.
89. Tung, N.M. and J.E. Garber, *BRCA1/2 testing: therapeutic implications for breast cancer management*. Brit J Cancer, 2018. **119**(2): p. 141-152.
90. Yang, X. and J. Wang, *Precision therapy for acute myeloid leukemia*. J Hematol Oncol, 2018. **11**(1): p. 3.
91. Zwierzina, H., *Combining immunotherapy with classical anticancer therapy*. Ann Oncol, 2008. **19 Suppl 7**: p. vii252-5.
92. Brown, G. and E. Marcinkowska, *Acute Myeloid Leukaemia: New Targets and Therapies*. Int J Mol Sci, 2017. **18**(12).
93. Teachey, D.T. and S.P. Hunger, *Acute lymphoblastic leukaemia in 2017: Immunotherapy for ALL takes the world by storm*. Nat Rev Clin Oncol, 2018. **15**(2): p. 69-70.
94. Renard, I. and S.J. Archibald, *CXCR4-targeted metal complexes for molecular imaging*, in *Med Chem*. 2020. p. 447-476.
95. Mutowo, P., *Chemokine receptor type 4 CXCR4 diseases, drugs and druggable target molecules*. 2011.
96. Zou, Y.-R., et al., *Function of the chemokine receptor CXCR4 in haematopoiesis and in cerebellar development*. Nature, 1998. **393**: p. 595-599.
97. Wang, Y., Y. Xie, and D. Oupicky, *Potential of CXCR4/CXCL12 Chemokine Axis in Cancer Drug Delivery*. Curr Pharmacol Rep, 2016. **2**(1): p. 1-10.
98. Barbieri, F., et al., *Drug design strategies focusing on the CXCR4/CXCR7/CXCL12 pathway in leukemia and lymphoma*. Expert Opinion on Drug Discovery, 2016. **11**(11): p. 1093-1109.
99. Tulotta, C., et al., *CXCR4 signaling regulates metastatic onset by controlling neutrophil motility and response to malignant cells*. Sci Rep, 2019. **9**(1): p. 2399.

100. Jacobs, S.M., et al., *CXCR4 expression in glioblastoma tissue and the potential for PET imaging and treatment with [(68)Ga]Ga-Pentixafor /[(177)Lu]Lu-Pentixather*. *Eur J Nucl Med Mol I*, 2021.
101. Bridger, G.J., et al., *Synthesis and Structure-Activity Relationships of Phenylenebis(methylene) Linked Bis-Tetraazamacrocycles That Inhibit HIV Replication. Effects of Macrocyclic Ring Size and Substituents on the Aromatic Linker*. *J Med Chem*, 1995. **38**(2): p. 366-378.
102. Donzella, G., et al., *AMD3100, a small molecule inhibitor of HIV-1 entry via the CXCR4 co-receptor*. *Nat Med*, 1998. **4**(1): p. 72-77.
103. Liles, W.C., et al., *Mobilization of hematopoietic progenitor cells in healthy volunteers by AMD3100, a CXCR4 antagonist*. *Blood*, 2003. **102**(8): p. 2728-30.
104. De Clercq, E., *The AMD3100 story: the path to the discovery of a stem cell mobilizer (Mozobil)*. *Biochem Pharmacol*, 2009. **77**(11): p. 1655-64.
105. Burroughs, L., et al., *Durable engraftment of AMD3100-mobilized autologous and allogeneic peripheral-blood mononuclear cells in a canine transplantation model*. *Blood*, 2005. **106**(12): p. 4002-8.
106. Martin, C., G.J. Bridger, and S.M. Rankin, *Structural analogues of AMD3100 mobilise haematopoietic progenitor cells from bone marrow in vivo according to their ability to inhibit CXCL12 binding to CXCR4 in vitro*. *Brit J Haematol*, 2006. **134**(3): p. 326-9.
107. Devine, S.M., et al., *Rapid mobilization of functional donor hematopoietic cells without G-CSF using AMD3100, an antagonist of the CXCR4/SDF-1 interaction*. *Blood*, 2008. **112**(4): p. 990-8.
108. De Clercq, E., *Recent advances on the use of the CXCR4 antagonist plerixafor (AMD3100, Mozobil) and potential of other CXCR4 antagonists as stem cell mobilizers*. *Pharmacol Therapeut*, 2010. **128**(3): p. 509-18.
109. Gerlach, L.O., et al., *Metal ion enhanced binding of AMD3100 to Asp(262) in the CXCR4 receptor*. *Biochemistry*, 2003. **42**(3): p. 710-717.
110. Jacobson, O., et al., *⁶⁴Cu-AMD3100--a novel imaging agent for targeting chemokine receptor CXCR4*. *Bioorgan Med Chem*, 2009. **17**(4): p. 1486-93.
111. Nimmagadda, S., et al., *Molecular imaging of CXCR4 receptor expression in human cancer xenografts with [⁶⁴Cu]AMD3100 positron emission tomography*. *Cancer Res*, 2010. **70**(10): p. 3935-44.
112. Weiss, I.D., et al., *Positron emission tomography imaging of tumors expressing the human chemokine receptor CXCR4 in mice with the use of ⁶⁴Cu-AMD3100*. *Mol Imaging Biol*, 2012. **14**(1): p. 106-14.
113. Burke, B.P., et al., *(⁶⁴Cu) PET Imaging of the CXCR4 Chemokine Receptor Using a Cross-Bridged Cyclam Bis-Tetraazamacrocyclic Antagonist*. *J Nucl Med*, 2020. **61**(1): p. 123-128.
114. De Silva, R.A., et al., *Imaging CXCR4 expression in human cancer xenografts: evaluation of monocyclam ⁶⁴Cu-AMD3465*. *J Nucl Med*, 2011. **52**(6): p. 986-93.
115. Hartimath, S.V., et al., *N-[(¹¹C)Methyl-AMD3465 PET as a Tool for In Vivo Measurement of Chemokine Receptor 4 (CXCR4) Occupancy by Therapeutic Drugs*. *Mol Imaging Biol*, 2017. **19**(4): p. 570-577.
116. Amor-Coarasa, A., et al., *[(¹⁸F)Fluoroethyltriazolyl Monocyclam Derivatives as Imaging Probes for the Chemokine Receptor CXCR4*. *Molecules*, 2019. **24**(8).
117. Brickute, D., et al., *Development and Evaluation of an (¹⁸F)-Radiolabeled Monocyclam Derivative for Imaging CXCR4 Expression*. *Mol Pharm*, 2019. **16**(5): p. 2106-2117.

118. Wu, Y., et al., *Synthesis and evaluation of [^{99m}Tc]TcAMD3465 as a SPECT tracer for CXCR4 receptor imaging*. J Radioanal Nucl Ch, 2021. **327**(2): p. 627-633.
119. Hunter, T.M., et al., *Configurations of metallocyclams and relevance to anti-HIV activity*. J Inorg Biochem, 2004. **98**(5): p. 713-9.
120. Hunter, T.M., et al., *Configurations of nickel-cyclam antiviral complexes and protein recognition*. Chem Eur J, 2007. **13**(1): p. 40-50.
121. Liang, X., et al., *Selective recognition of configurational substates of zinc cyclam by carboxylates: implications for the design and mechanism of action of anti-HIV agents*. Chem Eur J, 2003. **9**(19): p. 4709-17.
122. Liang, X., et al., *Structure and Dynamics of Metallomacrocycles: Recognition of Zinc Xylyl-Bicyclam by an HIV Coreceptor*. J Am Chem Soc, 2002. **124**(31): p. 9105-9112.
123. Niu, W., et al., *Inside or outside a ligand cleft? Synthetic, structural, and kinetic inertness studies of zinc, cadmium, and mercury complexes of cross-bridged cyclam and cyclen*. Dalton T, 2004(21): p. 3536-47.
124. Wainwright, K.P., *Bridging Alkylation of Saturated Polyaza Macrocycles: A Means for Imparting Structural Rigidity*. Inorg Chem, 1980. **19**: p. 1396-1398.
125. Weisman, G.R., et al., *Cross-Bridged Cyclam. Protonation and Li⁺ Complexation in a Diamond-Lattice Cleft*. J Am Chem Soc, 1990. **112**: p. 8604-8605.
126. Hubin, T.J., N.W. Alcock, and D.H. Busch, *Copper(I) and copper(II) complexes of an ethylene cross-bridged cyclam*. Acta Crystallogr, 2000. **56 (Pt 1)**: p. 37-9.
127. Niu, W., et al., *Two novel zinc(II) complexes of the 1,8-cross-bridged cyclam ligand and their structures*. Inorg Chem Commun, 1999. **2**: p. 361-363.
128. Hubin, T.J., et al., *Crystallographic Characterization of Stepwise Changes in Ligand Conformations as Their Internal Topology Changes and Two Novel Cross-Bridged Tetraazamacrocyclic Copper(II) Complexes*. Inorg Chem, 1999. **38**: p. 4435-4446.
129. Lewis, E.A., et al., *Efficient N- and C-functionalisation of cyclam macrocycles utilising bisaminal methodology*. Tetrahedron Lett, 2004. **45**(15): p. 3059-3062.
130. Lewis, E.A., R.W. Boyle, and S.J. Archibald, *Ultrastable complexes for in vivo use: a bifunctional chelator incorporating a cross-bridged macrocycle*. Chem Commun, 2004(19): p. 2212-3.
131. Mewis, R.E. and S.J. Archibald, *Biomedical applications of macrocyclic ligand complexes*. Coordin Chem Rev, 2010. **254**(15-16): p. 1686-1712.
132. Thorp-Greenwood, F.L. and M.P. Coogan, *Multimodal radio- (PET/SPECT) and fluorescence imaging agents based on metallo-radioisotopes: current applications and prospects for development of new agents*. Dalton T, 2011. **40**(23): p. 6129-43.
133. Khan, A., et al., *Binding Optimization through Coordination Chemistry: CXCR4 Chemokine Receptor Antagonists from Ultrarigid Metal Complexes*. J Am Chem Soc, 2009. **131**: p. 3416-3417.
134. Renard, I., *CXCR4 and ACKR3 binding agents for imaging applications in cancer*. 2019, The University of Hull. p. 262.
135. Woodard, L.E., et al., *Bridged cyclams as imaging agents for chemokine receptor 4 (CXCR4)*. Nucl Med Biol, 2014. **41**(7): p. 552-61.
136. Nakashima, H., et al., *Inhibition of human immunodeficiency viral replication by tannins and related compounds*. Antiviral Research, 1992. **18**(1): p. 91-103.

137. Trent, J.O., et al., *Lipid bilayer simulations of CXCR4 with inverse agonists and weak partial agonists*. J Biol Chem, 2003. **278**(47): p. 47136-44.
138. Tamamura, H., et al., *A Low-Molecular-Weight Inhibitor against the Chemokine Receptor CXCR4: A Strong Anti-HIV Peptide T140*. Biochem Bioph Res Co, 1998. **253**: p. 877-882.
139. Tamamura, H., et al., *Development of Specific CXCR4 Inhibitors Possessing High Selectivity Indexes as Well as Complete Stability in Serum Based on an Anti-HIV Peptide T140*. Bioorg Med Chem Lett, 2001. **11**(15): p. 1897-1902.
140. Hanaoka, H., et al., *Development of a ¹¹¹In-labeled peptide derivative targeting a chemokine receptor, CXCR4, for imaging tumors*. Nucl Med Biol, 2006. **33**(4): p. 489-94.
141. Weiss, I.D. and O. Jacobson, *Molecular imaging of chemokine receptor CXCR4*. Theranostics, 2013. **3**(1): p. 76-84.
142. Zhang, X.X., et al., *Comparison of (18)F-labeled CXCR4 antagonist peptides for PET imaging of CXCR4 expression*. Mol Imaging Biol, 2013. **15**(6): p. 758-67.
143. Jacobson, O., et al., *Improvement of CXCR4 tracer specificity for PET imaging*. J Control Release, 2012. **157**(2): p. 216-23.
144. Hennrich, U., et al., *Synthesis and in vitro evaluation of ⁶⁸Ga-DOTA-4-FBn-TN14003, a novel tracer for the imaging of CXCR4 expression*. Bioorgan Med Chem, 2012. **20**(4): p. 1502-10.
145. Jacobson, O., et al., *PET imaging of CXCR4 using copper-64 labeled peptide antagonist*. Theranostics, 2011. **1**: p. 251-262.
146. Rot, A., *Contribution of Duffy antigen to chemokine function*. Cytokine Growth F R, 2005. **16**(6): p. 687-94.
147. Fujii, N., et al., *Molecular-size reduction of a potent CXCR4-chemokine antagonist using orthogonal combination of conformation- and sequence-based libraries*. Angew Chem Int Edit, 2003. **42**(28): p. 3251-3.
148. Ueda, S., et al., *Structure-Activity Relationships of Cyclic Peptide-Based Chemokine Receptor CXCR4 Antagonists: Disclosing the Importance of Side-Chain and Backbone Functionalities*. J Med Chem, 2007. **50**: p. 192-198.
149. Demmer, O., et al., *Design, synthesis, and functionalization of dimeric peptides targeting chemokine receptor CXCR4*. J Med Chem, 2011. **54**(21): p. 7648-62.
150. Åberg, O., et al., *¹⁸F-labelling of a cyclic pentapeptide inhibitor of the chemokine receptor CXCR4*. J Fluorine Chem, 2012. **135**: p. 200-206.
151. George, G.P., et al., *Scavenging strategy for specific activity improvement: application to a new CXCR4-specific cyclopentapeptide positron emission tomography tracer*. J Labelled Compd Rad, 2013. **56**(13): p. 679-85.
152. Gourni, E., et al., *PET of CXCR4 expression by a (68)Ga-labeled highly specific targeted contrast agent*. J Nucl Med, 2011. **52**(11): p. 1803-10.
153. Demmer, O., et al., *PET imaging of CXCR4 receptors in cancer by a new optimized ligand*. Chem Med Chem, 2011. **6**(10): p. 1789-91.
154. Wester, H.J., et al., *Disclosing the CXCR4 expression in lymphoproliferative diseases by targeted molecular imaging*. Theranostics, 2015. **5**(6): p. 618-30.
155. Herrmann, K., et al., *Biodistribution and radiation dosimetry for the chemokine receptor CXCR4-targeting probe ⁶⁸Ga-pentixafor*. J Nucl Med, 2015. **56**(3): p. 410-6.

156. Philipp-Abbrederis, K., et al., *In vivo molecular imaging of chemokine receptor CXCR4 expression in patients with advanced multiple myeloma*. EMBO Mol Med, 2015. **7**(4): p. 477-87.
157. Lapa, C., et al., *[68Ga]Pentixafor-PET/CT for imaging of chemokine receptor 4 expression in small cell lung cancer - initial experience*. Oncotarget, 2016. **7** (8): p. 9288-9295.
158. Vag, T., et al., *PET imaging of chemokine receptor CXCR4 in patients with primary and recurrent breast carcinoma*. EJNMMI Res, 2018. **8**(1): p. 90.
159. Bouter, C., et al., *(68)Ga-Pentixafor PET/CT Imaging of Chemokine Receptor CXCR4 in Chronic Infection of the Bone: First Insights*. J Nucl Med, 2018. **59**(2): p. 320-326.
160. Pan, Q., et al., *Pulmonary Cryptococcosis Accidentally Detected by 68Ga-Pentixafor PET/CT in a Patient With Multiple Myeloma*. Clin Nucl Med, 2020. **45**(5): p. 423-425.
161. Schottelius, M., et al., *[(177)Lu]pentixather: Comprehensive Preclinical Characterization of a First CXCR4-directed Endoradiotherapeutic Agent*. Theranostics, 2017. **7**(9): p. 2350-2362.
162. Poschenrieder, A., et al., *Preclinical evaluation of [(68)Ga]NOTA-pentixafor for PET imaging of CXCR4 expression in vivo - a comparison to [(68)Ga]pentixafor*. EJNMMI Res, 2016. **6**(1): p. 70.
163. Poschenrieder, A., et al., *First (18)F-Labeled Pentixafor-Based Imaging Agent for PET Imaging of CXCR4 Expression In Vivo*. Tomography, 2016. **2**(2): p. 85-93.
164. Herrmann, K., et al., *First-in-Human Experience of CXCR4-Directed Endoradiotherapy with 177Lu- and 90Y-Labeled Pentixather in Advanced-Stage Multiple Myeloma with Extensive Intra- and Extramedullary Disease*. J Nucl Med, 2016. **57**(2): p. 248-51.
165. Archibald, S.J. and L. Allott, *The aluminium-[(18)F]fluoride revolution: simple radiochemistry with a big impact for radiolabelled biomolecules*. EJNMMI Radiopharm Chem, 2021. **6**(1): p. 30.
166. Kolb, H.C., M.G. Finn, and K.B. Sharpless, *Click Chemistry: Diverse Chemical Function from a Few Good Reactions*. Angew Chem Int Edit, 2001. **40**: p. 2004-2021.
167. Knight, J.C. and B. Cornelissen, *Bioorthogonal chemistry: implications for pretargeted nuclear (PET/SPECT) imaging and therapy*. Am J Nucl Med Mol Imaging, 2014. **4**(2): p. 96-113.
168. Selvaraj, R., et al., *Improved metabolic stability for 18F PET probes rapidly constructed via tetrazine trans-cyclooctene ligation*. Bioconjugate Chem, 2015. **26**(3): p. 435-42.
169. Brachet, E. and P. Belmont, *Inverse Electron Demand Diels-Alder (IEDDA) Reactions: Synthesis of Heterocycles and Natural Products Along with Bioorthogonal and Material Sciences Applications*. Curr Org Chem, 2016. **20**(21): p. 2136-2160.
170. Kaur, R., et al., *1,2,3-Triazole beta-lactam conjugates as antimicrobial agents*. Heliyon, 2020. **6**(6): p. e04241.
171. Li, J., et al., *Radiolabeling of RGD peptide and preliminary biological evaluation in mice bearing U87MG tumors*. Bioorgan Med Chem, 2012. **20**(12): p. 3850-5.
172. Dubash, S.R., et al., *Clinical Translation of a Click-Labeled 18F-Octreotate Radioligand for Imaging Neuroendocrine Tumors*. J Nucl Med, 2016. **57**(8): p. 1207-13.
173. Allott, L., S. Dubash, and E.O. Aboagye, *[(18)F]FET-betaAG-TOCA: The Design, Evaluation and Clinical Translation of a Fluorinated Octreotide*. Cancers (Basel), 2020. **12**(4).
174. Castro, V., H. Rodriguez, and F. Albericio, *CuAAC: An Efficient Click Chemistry Reaction on Solid Phase*. ACS Comb Sci, 2016. **18**(1): p. 1-14.

175. Fang, Y., et al., *Insight into the Mechanism of the CuAAC Reaction by Capturing the Crucial Au₄Cu₄-pi-Alkyne Intermediate*. J Am Chem Soc, 2021. **143**(4): p. 1768-1772.
176. Filpula, D. and H. Zhao, *Releasable PEGylation of proteins with customized linkers*. Adv Drug Deliver Rev, 2008. **60**(1): p. 29-49.
177. Harris, J.M. and R.B. Chess, *Effect of pegylation on pharmaceuticals*. Nat Rev Drug Discov, 2003. **2**: p. 214-221.
178. Wu, Z., et al., *18F-labeled mini-PEG spacers RGD dimer (18F-FPRGD2): synthesis and microPET imaging of alphavbeta3 integrin expression*. Eur J Nucl Med Mol I, 2007. **34**(11): p. 1823-1831.
179. Autio, A., et al., *Mini-PEG spacing of VAP-1-targeting 68Ga-DOTAVAP-P1 peptide improves PET imaging of inflammation*. EJNMMI Res, 2011. **1**(10).
180. Rang, H.P., et al., *Rand and Dale's Pharmacology*. Sixth edition ed. 2007, Philadelphia: Elsevier Limited. 829.
181. Goswami, L.N., et al., *Efficient synthesis of diverse heterobifunctionalized clickable oligo(ethylene glycol) linkers: potential applications in bioconjugation and targeted drug delivery*. Org Biomol Chem, 2013. **11**(7): p. 1116-26.
182. Bogdan, N.D., et al., *Protein-inorganic array construction: design and synthesis of the building blocks*. Chem Eur J, 2010. **16**(7): p. 2170-80.
183. Gentilini, C., M. Boccalon, and L. Pasquato, *Straightforward Synthesis of Fluorinated Amphiphilic Thiols*. Eur J Org Chem, 2008. **2008**(19): p. 3308-3313.
184. Gavriluk, J.I., U. Wuellner, and C.F. Barbas, 3rd, *Beta-lactam-based approach for the chemical programming of aldolase antibody 38C2*. Bioorg Med Chem Lett, 2009. **19**(5): p. 1421-4.
185. Kaiser, E., et al., *Color test for detection of free terminal amino groups in the solid-phase synthesis of peptides*. Anal Biochem, 1970 **34**(2): p. 595-8.
186. Isidro-Llobet, A., M.A. Ivarez, and F. Albericio, *Amino Acid-Protecting Groups*. Chem Rev, 2009. **109**: p. 2455-2504.
187. Thieriet, N., et al., *Use of Alloc-amino Acids in Solid-Phase Peptide Synthesis*. Tetrahedron Lett, 1997. **38**(41): p. 7275-7278.
188. *Fmoc Solid Phase Peptide Synthesis: A Practical Approach*, ed. H.B. D. 2000, New York: Oxford University Press. 346.
189. Claes, S., et al., *A Kinetic Fluorescence-based Ca²⁺ Mobilization Assay to Identify G Protein-coupled Receptor Agonists, Antagonists, and Allosteric Modulators*. J Vis Exp, 2018(132).
190. Princen, K., et al., *Evaluation of SDF-1/CXCR4-induced Ca²⁺ signaling by fluorometric imaging plate reader (FLIPR) and flow cytometry*. Cytom Part A, 2003. **51**(1): p. 35-45.
191. Schoofs, G., et al., *A Flow Cytometry-based Assay to Identify Compounds That Disrupt Binding of Fluorescently-labeled CXC Chemokine Ligand 12 to CXC Chemokine Receptor 4*. J Vis Exp, 2018(133).
192. Gill, H.S. and J. Marik, *Preparation of 18F-labeled peptides using the copper(I)-catalyzed azide-alkyne 1,3-dipolar cycloaddition*. Nat Protoc, 2011. **6**(11): p. 1718-25.